UNIVERSITAT DE BARCELONA

Investigating the roles of MnO_2-acid complexes in catalytic ozonation for enhanced micropollutants abatement in water

Liu Jing

UNIVERSITAT DE BARCELONA

Programa Enginyeria i Ciències Aplicades

Investigating the roles of MnO_2-acid complexes in catalytic ozonation for enhanced micropollutants abatement in water

Jing Liu

Director:

Dra. Carme Sans Mazon

Tutor:

Dra. Carme Sans Mazon

Departament d’Enginyeria Química i Química Analítica

Programa Enginyeria i Ciències Aplicades

Investigació els rols dels complexos MnO_2-àcid en l'ozonització catalítica per a la millora de l'eliminació de microcontaminants en l'aigua

Jing Liu

Directora:

Dra. Carme Sans Mazon

Tutora:

Dra. Carme Sans Mazon

Departament d'Enginyeria Química i Química Analítica

Abstract

A significant amount of organic pollutants has been released into the water environment with the rapid growth of the population. To remove refractory compounds from the aquatic environment, advanced oxidation processes (AOPs), such as electrochemical methods, Fenton system, irradiation and ozonation have attracted more attention. Heterogeneous catalytic ozonation (HCO), as one of the AOPs, could shorten treatment time, enhance pollutant removal efficiency, and improve ozone (O_3) availability, which has gained increasing interest. Considering that catalysts used in the HCO process should be low-cost, environmentally friendly, and readily available, manganese dioxide (MnO_2) composites were used as catalysts in this study to explore their catalytic activity towards pollutant removal in water.

In this thesis, α-MnO_2, β-MnO_2, and δ-MnO_2 were fabricated through a modified hydrothermal-calcination method and evaluated for their potential catalytic ozonation performance in degrading oxalic acid (OA) through semi-continuous experiments. In order to control individual variables of experimental conditions, batch experiments were further conducted to assess the catalytic activities of the catalysts. It was found that the introduction sequence of the catalyst and O_3 stock solution greatly affects the efficiency of the HCO system. For example, when the α-MnO_2 catalyst (50 mg L^{-1}) was added to the OA (10 mg L^{-1}) solution first, followed by O_3 introduction (30 mg L^{-1}), the OA removal rate reached 78.22%. Conversely, the efficiency was only 20.53% when the sequence weas reversed. Pre-contact between oxalic acid (OA) and the catalyst seems to have a significant impact on the efficiency of catalytic ozonation.

To identify the influence of OA in the process, Cat/OA/O_3 system was established using atrazine (ATZ) as a model pollutant. The effect of operational parameters on catalytic performance including the O_3 concentrations (1-30 mg L^{-1}), catalysts dosages (10-50 mg L^{-1}), pH values (pH=3-7), and the molar ratio of catalyst to OA were investigated. Compare to O_3 alone (43.6%), when the molar ratio of catalyst-to-OA increased to 1:0.8, the ATZ (5 mg L^{-1}) degradation efficiencies within 3 min were 95.09%, 93.43%, and 96.71% for the α-MnO_2/OA/O_3, β-MnO_2/OA/O_3, and δ-MnO_2/OA/O_3 systems at pH 3.0, respectively.

Abstract

This study confirmed that the complexation between metal oxides and organic acid plays an important role in water treatment. However, the mechanism of complex in catalytic ozonation process (HCO) was not studied yet. To elucidate the mechanism, as well as the phase effect and ROS contribution for each system, a series of characterizations, pyrophosphate experiments, and probe experiments were designed. The results verified that the formation of the MnO_2-OA complexes relied on the presence of Mn^{3+} on the catalyst surface, which enhanced electron transfer and facilitated the creation of active sites such as oxygen vacancies. This, in turn, accelerated O_3 decomposition, generating more reactive oxygen species (ROS) and further promoting pollutant degradation.

In addition, the crystalline phase of MnO_2 did not influence the formation of MnO_2-OA complexes but affected the reaction sites between the complexes and O_3. For the α-MnO_2-OA complex, more oxygen vacancies were generated on the surface, adsorbing O_3 and pollutants for further reaction. For the β-MnO_2-OA complex, more manganese vacancies and enhanced lattice oxygen (O_L) mobility were key factors contributing to ROS production. As for the δ-MnO_2-OA complex, the surface -OH groups acted as the main active site, reacting with O_3 to generate more ROS, thus improving ATZ degradation. Interestingly, probe experiments suggested that in the MnO_2-OA complex-mediated catalytic ozonation system, the $O_2^{\bullet-}$ played a major role in ATZ removal, followed by $^{\bullet}OH$, while O_3 and $^1O_2$ had a lesser effect.

This thesis provides new insights into the potential applications and perspectives of MnO_2 in catalytic ozonation.

Resum

Amb el ràpid creixement de la població, es generen grans quantitats de contaminants orgànics que s'alliberen al medi aquàtic. Per eliminar aquests compostos refractaris, els processos d'oxidació avançada (AOPs), entre els quals destaca l'ozonització catalítica heterogènia (HCO), han demostrat la seva eficàcia, ja que redueixen el temps de tractament, milloren l'eliminació de contaminants i optimitzen l'ús de l'ozó (O_3). El diòxid de manganès (MnO_2) és un catalitzador atractiu gràcies al seu baix cost i fàcil disponibilitat.

En aquest estudi, s'han sintetitzat α-MnO_2, β-MnO_2 i δ-MnO_2 mitjançant un mètode hidrotermal-calcinat modificat, i s'ha avaluat la seva eficàcia en la degradació d'àcid oxàlic (OA). S'ha comprovat que la seqüència d'addició del catalitzador i de l'O_3 influeix de manera determinant en l'eficiència del procés HCO: per exemple, amb α-MnO_2 es va assolir un 78,22% d'eliminació d'OA quan s'afegia l'ozó a la solució amb el catalitzador, en comparació amb el 20,53% en invertir l'ordre. A més, d'altres àcids (FA, AA, CA i PA) també han mostrat capacitat per promoure l'ozonització catalítica a través de la formació de complexos amb MnO_2.

Per tal d'entendre el mecanisme, s'ha estudiat en detall el sistema β-MnO_2/OA/O_3, aconseguint un 90,4% de degradació de pCBA i un 65,2% d'eliminació d'OA en 10 minuts a pH 4,0. Les caracteritzacions (XPS, H2-TPR, etc.) indiquen que el complex β-MnO_2-OA millora la transferència electrònica i afavoreix la formació de vacants d'oxigen i espècies reactives d'oxigen (ROS). Mitjançant l'ús de pirofosfat de sodi es va confirmar que el Mn^{3+} és fonamental en la formació d'aquest complex, mentre que els experiments amb captadors de radicals van identificar el radical $^{\bullet}OH$ com l'espècie principal en la degradació de pCBA.

Les diferents fases cristal·lines de MnO_2 no afecten la formació del complex MnO_2-OA—dependent del Mn^{3+}—però sí que influeixen en la via de producció de ROS. Al sistema α-MnO_2-OA predominen vacants d'oxigen superficial, al β-MnO_2-OA destaquen vacants de manganès i més mobilitat de l'oxigen de xarxa, i al δ-MnO_2-OA són els grups -OH els principals centres actius. Els radicals $O_2^{\bullet-}$ i $^{\bullet}OH$ s'han identificat com els responsables principals de la degradació dels contaminants.

Acknowledgement

Life can feel like a play, full of twists and brilliant moments. Time slips away quickly, causing us to forget and remember in an endless cycle. As I look back, my four years of doctoral studies are about to end. I cannot help but reflect on these four years in Barcelona, a time truly worth cherishing all my life.

When I first arrived in Barcelona, I felt the warmth of an unfamiliar city and faced the challenges of a new life. From the initial fear during the pandemic to the calm with which I now handle numerous complicated situations, I have journeyed from 2021 to 2025, living and growing these four years. I have witnessed Barcelona in full bloom in spring, heard its drizzly summer rains, enjoyed its gentle autumn breeze, and experienced its lively, bustling winters. Now that graduation is near, I have so much to express and so many people to thank.

I always say my advisor, Carmen Sans, is an angel---always gentle, approachable, and smiling. The words she repeats most often are: “If you need anything, just tell me. If you have any trouble, let me know. If you need help, I’m here.” Over these four years at the University of Barcelona, she has provided not only academic support but also emotional encouragement. I am fortunate to have had such a mentor.

Professor Yuan Xiangjuan is, strictly speaking, more than just a teacher. We met in 2017, and for my research project, she guided my first steps, propelled me forward, and gave me direction so I could see a bigger sky. I am also grateful that she decided to spend a year in Barcelona for academic exchange, so that I could feel the care of someone familiar, even in a foreign land.

As the first Chinese student in our research group, both the environment and the language were unfamiliar, but I adapted quickly thanks to my wonderful colleagues. My senior Oriol was the first friend I made, guiding me around the lab and teaching me Spanish words—sometimes even playful or “bad” ones—helping me integrate smoothly. My friend Noemi was shy when we first met (and so was I), yet she worried if I felt awkward or uncomfortable, took me around the city, and made a foreign land feel less distant. Veronica is always gentle and kind, offering gifts on birthdays and holidays, sharing happiness and blessings, and listening patiently. I have never heard her speak ill of anyone; she is truly someone to treasure. And of course, there is Cristopher, who loves to startle me but is actually a calm, considerate person. He often says, “If you’re upset, let us know—we’re your friends.” Beyond them, many others in the office greet me warmly every morning and offer sincere farewells every evening. It’s more than just an office; it’s another place at the University of Barcelona I hold dear. Their support in both coursework and daily life has been my sunshine these past four years.

As an international student, I have been lucky. While others worried about housing, I stayed in one apartment for more than three years, free from domestic troubles. I am grateful to have met my landlords, Gao Ye and Cui Yue, and their daughter, Moli. Thanks to them, I never felt lonely during festive holidays, I always had someone concerned about me when I left home, I had someone to confide in when I was anxious, and someone to accompany me when I felt carefree. They made Barcelona feel like home, and for three years, I found gratitude that I will carry with me forever.

I am also thankful to the other professors at the university, who offered serious dedication in project discussions and kept the lab well-organized, enabling me to reach the threshold of graduation smoothly.

Finally, I would like to thank myself: for having the patience to deal with everyday trivialities, the persistence to endure scientific setbacks, the courage to face challenges, and the confidence to keep forging ahead. I have lived each day and left footprints along the way—memories of these four PhD years. I do not regret coming to Barcelona.

In closing, I want to thank everyone and everything I encountered here for making my time in Barcelona feel genuine. I wish all of us, including myself, the very best—that all our hopes may, in the end, be realized.

Nomenclature

The used abbreviations, acronyms and symbols are gathered below:

AOPs	Advanced oxidation processes
ACMP	Acetaminophen
ACN	Acetonitrile
CBA	Chlorobenzoic acid
ATZ	Atrazine
HCO	Heterogenous catalytic ozonation
IBU	Ibuprofen
pCBA	p-Chlorobenzoic acid
AA	Acetic acid
CA	Citric acid
FA	Formic acid
PA	Pyruvic acid
BQ	*p*-benzoquinone
TBA	Tert-butanol
NaN_3	Sodium azide
BET	Brunauer-Emmett-Teller
BJH	Barrett-Joyner-Halenda
ESR	Electron spin resonance
HRTEM	High-resolution transmission electron microscopy
SEM	Scanning electron microscope
H_2-TPR	Hydrogen temperature programmed reduction
FT-IR	Fourier transform infrared
Py-IR	Pyridine adsorbed IR spectroscopy
XPS	X-ray photoelectron spectra
O_2-TPD	Oxygen temperature programmed desorption analysis

HPLC	High Performance Liquid Chromatography
$C_2H_2O_4$ (OA)	Oxalic acid 2-hydrate
2,4-D	2,4-dichlorophenoxyacetic acid
DMPO	5,5-dimethyl-1-pyrolin-N-oxide
TEMPO	2,2,6,6-Tetramethyl-1-piperidinyloxy
HCl	Hydrochloric acid
NaOH	Sodium hydroxide
H_3PO_4	Phosphoric acid
$KMnO_4$	Potassium permanganate
MDE	Metronidazole
$MnSO_4$	Manganese sulphate 1-hydrate
MnO_2	Manganese dioxides
MnOx	Manganese oxides
$Na_2S_2O_3$	Sodium thiosulfate
$(NH_4)_2S_2O_8$	Ammonium persulfate
O_2	Oxygen
O_3	Ozone
$^{\bullet}OH$	Hydroxyl radical
$O_2^{\bullet-}$	Superoxide radical
$^1O_2$	Singlet oxygen
ROS	Reactive oxygen species
TA	Terephthalic acid

Outline

CHAPTER 1

Introduction

1.1. Water pollution

Water, as a vital resource essential for human survival, is closely tied to human life. With the advancement of urbanization and industrialization, water pollution has worsened, endangering human health and severely impacting ecosystems [1]. The main sources of water pollution include agricultural runoff and infiltration, medical wastewater, domestic sewage and industrial wastewater. In agricultural production, the use of pesticides and fertilizers has been increasing, leading to the introduction of large amounts of suspended solids, pesticide residues, and fertilizer components into water bodies through rainfall runoff, irrigation, and soil infiltration [2]. Domestic sewage contains not only non-toxic solid impurities such as cellulose, sulfates, and phosphates but also trace metals like copper, manganese, and zinc, as well as detergent components [3]. Among these, high concentrations of nitrogen and phosphorus pose major challenges in water treatment. In contrast, although industrial wastewater is discharged in smaller quantities than domestic sewage, its complex composition presents a more severe threat to water quality. For instance, pharmaceutical wastewater contains residual antibiotics, intermediate metabolites, high concentrations of sulfate ions, and organic solvents, while wastewater from chemical synthesis is rich in harmful pollutants such as phenolic compounds, polycyclic substances, sulfides, and cyanides [4-5]. These toxic substances exhibit high toxicity to microbial communities, severely disrupting aquatic ecosystems.

As water pollution worsens, emerging micropollutants in the environment are increasing, including pesticides, endocrine-disrupting compounds (EDCs), pharmaceutically active compounds (PhACs), and personal care products (PCPs) [6]. These pollutants exist in trace concentrations (ranging from μg L^{-1} to ng L^{-1}) [7]. Due to their persistence, bioaccumulation potential, and ability to disrupt fragile ecosystems, their removal has received increasing attention [8-9]. Conventional water treatment processes, such as bar-screening, grit removal, pre-oxidation, coagulation-flocculation, sedimentation, filtration and disinfection, are primarily used to remove solids of various sizes, organic matter, and microorganisms/pathogens [10-11]. As for micropollutants with low concentrations, conventional wastewater treatment technologies face considerable difficulties in detecting and removing these substances [12]. Therefore, implementing effective strategies to manage and eliminate these pollutants is crucial for safeguarding ecosystems and human well-being.

1.2. Micropollutants treatment

Micropollutants, even in trace amounts (μg L^{-1} to ng L^{-1}), present substantial obstacles to maintaining water quality and protecting environmental health. Conventional water treatment techniques often struggle to remove these trace contaminants effectively and achieve compliance with environmental regulations. Consequently, a range of physico-chemical methods, such as adsorption, membrane filtration, and advanced oxidation processes, have gained prominence for their ability to mitigate or eliminate micropollutants from natural water sources and wastewater treatment systems [13].

1.2.1. Adsorption

Adsorption is a process where micropollutants bind to solid surfaces or adsorbents through various physical and chemical interactions, such as electrostatic forces, hydrogen bonding, π-π bonding, and hydrophobic effects. This approach has obtained traction as a viable alternative to conventional wastewater treatment methods due to its simplicity and excellent efficiency in pollutant removal. Recent progress in adsorption research has largely focused on the development of innovative adsorbents with improved capacity and selectivity [14]. Among the most widely used adsorption methods is the application of activated carbon (AC), a material derived from the pyrolytic decomposition of carbon-rich substances. AC, characterized by its high surface area, porosity, and hydrophobic properties, is particularly effective at capturing a broad spectrum of micropollutants, including organic chemicals and pharmaceuticals [15]. Additionally, various other promising adsorbents include nanomaterials, carbon nanotubes, hudroxide-based compound, natural zeolites, ion exchange resins, metal-organic frameworks, and graphene-derived materials [16]. The effectiveness of adsorption processes can be greatly affected by environmental factors, such as the presence of dissolved organic matter, fluctuations in ionic strength, and competing contaminants, all of which may modify the interactions between micropollutants and adsorbents.

1.2.2. Membrane filtration

Membrane filtration techniques utilize semipermeable membranes with precisely controlled pore sizes to physically separate micropollutants and other contaminants from water [17]. These membranes act as selective barriers, permitting the passage of water molecules while trapping micropollutants based on factors such as size, molecular weight, adsorption, and charge. Different membrane filtration methods, including microfiltration (MF), ultrafiltration (UF), reverse osmosis (RO), and nanofiltration (NF), each have unique pore size ranges and removal capabilities [18]. Additionally, membrane systems are scalable and versatile, making them suitable for a wide range of applications, from small-scale household water treatment to large-scale municipal and industrial processes. As a continuous filtration process, these systems enable real-time water treatment, offering a quick response to emerging micropollutants. However, despite their advantages, membrane filtration faces challenges such as membrane fouling, where the buildup of particulate matter or organic substances on the membrane surface can decrease filtration efficiency over time. This requires routine maintenance, cleaning, and, in some instances, the use of chemical cleaning agents [16].

1.2.3. Advanced oxidation processes (AOPs)

Advanced oxidation processes (AOPs) utilize the production of highly reactive free radicals (such as •OH, chlorine radical ($^{\bullet}Cl$), and ozone radical ($^{\bullet}O_3$)) to oxidize and degrade micropollutants into harmless byproducts [19]. These processes encompass a variety of techniques, including ultraviolet (UV) irradiation, hydrogen peroxide (H_2O_2) treatment, photocatalysis, Fenton, and ozonation [20].

1) Electrochemical oxidation

Electrochemical oxidation utilizes an externally applied electric field to efficiently degrade pollutants under normal pressure and temperature conditions [21], which can be achieved through two pathways. One is the direct anodic oxidation technique, where pollutants adsorbed on the anode surface undergo electron transfer with the high-potential anode, causing the pollutants to lose electrons and be directly oxidized and degraded. The anode materials typically include activated carbon, graphite, and others [22]. Another pathway is the indirect cathodic oxidation technique, where a strong oxidative active oxygen species (ROS), such as hydrogen peroxide (H_2O_2), $^{\bullet}OH$, and others, is generated on the cathode surface under the influence of current. These substances are used to enhance the degradation of organic matter [21]. Due to its simple equipment, mild reaction conditions, controllable processes, environmental friendliness, and high treatment efficiency, electrochemical oxidation is widely studied and applied in wastewater treatment. However, during the electrochemical treatment process, various pollutants and intermediates can easily accumulate on the electrode surface, leading to a decrease in electrode activity and a shortened lifespan.

2) Photochemical oxidation

Photochemical oxidation, as an emerging advanced oxidation technology, is a method that utilizes ultraviolet (UV) or visible light to degrade organic pollutants [23]. It mainly includes photolytic oxidation, and photocatalytic oxidation, and other combined technologies such as photofenton oxidation and photoelectrochemical catalysis. In photocatalytic oxidation, photosensitive semiconductor materials are irradiated with UV or visible light, which excites photogenerated holes and electrons. These electrons then interact with oxygen and water molecules to generate highly oxidative free radicals, thereby enhancing the degradation of organic substances [24]. Photolytic oxidation, on the other hand, involves the decomposition of water molecules under light irradiation to produce $^{\bullet}OH$, which then degrade pollutants through a series of free radical reactions. Currently, widely studied techniques include UV/H_2O_2, UV/ozone, and UV/chlorine. UV-based oxidation methods exhibit remarkable effectiveness in removing a wide range of micropollutants, such as personal care products, endocrine-disrupting compounds, and pharmaceuticals [25].

3) Fenton-like oxidation

The typical Fenton reaction [26] involves ferrous ions (Fe^{2+}) reacting with H_2O_2 under acidic conditions (pH 3-5), producing highly oxidative $^{\bullet}OH$ radicals. These radicals non-selectively react with most organic compounds, effectively removing refractory wastewater pollutants such as phenols, aromatic hydrocarbons, and aromatic amines. However, the traditional Fenton oxidation technology is limited by pH, as Fe^{3+} readily precipitates at higher pH values. To ensure the smooth progression of the Fenton reaction, a series of Fenton-like oxidation methods have been developed for wastewater treatment. Broadly speaking, any method that generates $^{\bullet}OH$ through reactions with H_2O_2 or HO_2^- can be referred to as a Fenton-like method [27]. Studies have shown that introducing homogeneous catalysts such as Co^{2+} and Cu^{2+} into the Fenton system can enhance the oxidation efficiency; meanwhile, transition metals can also act as heterogeneous catalysts in multi-phase Fenton-like systems [28-29]. Furthermore, the application of external field energies such as ultrasound, microwave, light, and electricity can effectively promote the Fenton oxidation process [30]. This has led to the development of a series of emerging Fenton systems, including ultrasonic Fenton, microwave Fenton, photo-Fenton, and electro-Fenton systems.

4) Ozonation

Ozone (O_3), an allotrope of oxygen (O_2) with three oxygen atoms, has a distinctive pungent odour. As a powerful oxidant, O_3 has a high oxidation potential (2.07V) and a strong electrophilic ability in water [31]. During wastewater treatment, it plays a role in decolorization, disinfection, deodorization, and pollutant degradation [32]. O_3 is simple to produce, can be generated on-site using air, and its oxidation byproducts are O_2, which does not cause secondary pollution, making it a clean oxidant. However, when O_3 is used alone as an oxidant in wastewater treatment, issues such as low ozone utilization, low mineralization rate, slow reaction rate, and high cost arise. Therefore, to enhance the utilization of O_3 and improve pollutant removal efficiency, O_3 is often combined with other processes. In recent years, commonly used process systems include O_3/H_2O_2, UV/O_3, and photocatalysis/O_3.

1.2.4. Sonochemical oxidation

Sonochemical oxidation techniques encompass a group of advanced oxidation processes (AOPs) that harness ultrasound waves to produce highly reactive hydroxyl radicals (•OH) in water [33]. This process relies on acoustic cavitation, a phenomenon where the rapid expansion and collapse of microscopic bubbles in a liquid generate extreme localized conditions — pressures reaching up to 1000 atm and temperatures as high as 5000 K. These extreme conditions lead to the formation of reactive species such as hydrogen, •OH, hydroperoxyl radicals, and hydrogen peroxide [34]. The generated radicals interact with organic and inorganic micropollutants, breaking chemical bonds and initiating oxidation reactions, which result in the degradation of pollutants and their transformation into less hazardous byproducts.

1.3 Catalytic ozonation

O_3 technology can removal harmful substances via the strong oxidation of O_3, enhancing water quality while contributing to environmental protection. However, its application is often limited by high energy consumption and low mineralization efficiency. To address these challenges, catalyzing the ozonation process with transition metals and metal oxides has shown promise in improving the degradation efficiency of organic materials. This approach activates O_3 to generate more reactive oxygen species (ROS) such as $^{\bullet}OH$, superoxide radical ($O_2^{\bullet-}$), and singlet oxygen ($^1O_2$). According to the catalyst used, the system can be further divided into homogeneous and heterogeneous catalytic ozonation.

1.3.1 Homogeneous catalytic ozonation (HO)

Homogeneous ozonation typically uses metal ions as catalysts to generate free radicals through ozone O_3 decomposition, thereby degrading pollutants. Commonly used transition metal ions include Mn^{2+}, Ni^{2+}, Co^{2+}, Cu^{2+}, and Zn^{2+}, as well as some noble or rare earth metal ions such as Ag^+, Ce^{3+}, and Au^{3+} [35-36]. The addition of metal ions serves two primary purposes: first, to directly promote the decomposition of O_3, producing high ROS, and accelerating the breakdown of organic pollutants; second, to react with organic compounds in the system to form complexes that release highly reactive species, which are then further attacked by O_3, thereby enhancing the reaction rate [36]. However, homogeneous catalytic systems face challenges such as catalyst loss and difficulty in recovery, which increase the complexity of removing metal ions in subsequent processes and significantly raise treatment costs. Consequently, research efforts have increasingly focused on developing heterogeneous catalytic ozonation techniques, where the catalyst are easy to separate and there is no production of secondary pollution come from metal ions.

1.3.2 Heterogeneous catalytic ozonation (HCO)

The process of adding solid catalysts to a solution to promote the decomposition of O_3, thereby directly producing ROS to degrade organic pollutants, is referred to as heterogeneous catalytic ozonation. The advantages of HCO are summarized as: 1) catalysts in solid form with high efficiency and stability; 2) it enables faster, large-scale production; 3) efficiently mineralize most contaminants; 4) sustained reactions via an active surface that does not require a continuous supply of regents [37]. Consequently, selecting catalysts with catalytic activity, high stability, and cost-effectiveness is the key for the success of HCO technology.

Common catalysts include mineral materials (e.g., natural mineral magnesium hydroxide $Mg(OH)_2$), metal oxides (e.g., Al_2O_3, MnO_2, FeOOH, TiO_2), activated carbon (AC), and supported metal oxides [38-40]. Amongst, manganese oxides (MnO_x) were regarded as the prospective active catalysts for the catalytic ozonation. The oxygen mobility in the oxide lattice and good single electron-transfer redox reaction of Mn^{2+}/Mn^{3+} or Mn^{3+}/Mn^{4+} could be ascribe to the transformation of oxidation states between Mn^{2+} and Mn^{4+}[41]. Manganese dioxide (MnO_2), a common MnO_x, due to its environment friendliness, abundant resources, high efficiency, good thermal stability, and low cost are widely used for HCO in aqueous solution [42]. Based on this, some research progress on the application of MnO_2/MnO_2-based catalysts in HCO will be further introduced in the subsequent sections

1.3.3 ROS identification in catalytic ozonation process

In the catalytic ozonation system, the reactive oxygen species (ROS) generated by the chain reaction decomposition of O_3 play a crucial role. These ROS, such as $^{\bullet}OH$, superoxide radical ($O_2^{\bullet-}$), and singlet oxygen ($^1O_2$) can directly react with target contaminants, thereby promoting both pollutant removal efficiency and catalyst activity. To identify the role of ROS in catalytic ozonation system, conventional scavenging experiments, Electron Spin Resonance (ESR) characterization, and probe method are typically operated (Fig.1.1).

1) Radical scavenger experiment

The frequently employed scavengers for quenching ROS include: *Tert*-butanol (TBA), *p*-benzoquinone (*p*-BQ), and sodium azide (NaN_3). The reaction rate constants (k) of TBA with $^{\bullet}OH$ and O_3 have been reported as $3.8\text{-}7.6\times10^8$ M^{-1} S^{-1} and 3×10^{-3} M^{-1} S^{-1}, respectively. *p*-BQ can react with $O_2^{\bullet-}$, $^{\bullet}OH$, and O_3, with rate constants k ($O_2^{\bullet-}$) $=3.5\text{-}7.8\times10^8$ M^{-1} S^{-1}, k ($^{\bullet}OH$) $=1.2\times10^9$ M^{-1} S^{-1}, and k (O_3) $= 2.5\times10^3$ M^{-1} S^{-1}. Moreover, NaN_3 is commonly applied as scavenger for $^1O_2$, with k ($^1O_2$) values following the order: NaN_3 (2×10^9 M^{-1} S^{-1}) > *p*-BQ (6.6×10^7 M^{-1} S^{-1}) > TBA (1.8×10^3 M^{-1} S^{-1}) [43]. In addition to these scavengers, dimethyl sulfoxide (DMSO) is adopted to scavenge absorbed $^{\bullet}OH$ on the surface of catalyst due to its hydrophobic features [44]. Meanwhile, Yang et al [89] added sodium bicarbonate ($NaHCO_3$) into catalytic ozonation system (MnO_2-NH_2/GO/p-C_3N_4/O_3), the degradation of cephalexin (CLX) was significantly inhibited. It was explained that $NaHCO_3$ could be $^{\bullet}OH$ quencher effecting the degradation process.

2) ESR/EPR characterization

Electron Spin Resonance (ESR) spectroscopy, also referred to as Electron Paramagnetic Resonance (EPR) spectroscopy, is a method designed to investigate substances containing unpaired electrons. This technique offers insights into the electronic configuration, surrounding environment, and behavior of paramagnetic species, such as free radicals, transition metal complexes, and crystal defects, by analyzing the magnetic interactions of unpaired electrons when exposed to an external magnetic field. 5,5-Dimethyl-1-pyrroline (DMPO) and 2,2,6,6-Tetramethyl-4-piperidone (TEMP) are two commonly reagents used in ESR/EPR spectroscopy, especially in further identify the presence of $^{\bullet}OH$, $O_2^{\bullet-}$, and $^1O_2$.

3) Trace amount probe method

Guo et al. [45] conducted conventional ozonation and MnO_2 catalytic ozonation of the selected surface water (spiked with ~ 1.4 µm *m*-DCB) in batch mode. The scavenger and probe approaches for characterizing the role of $^{\bullet}OH$ and $O_2^{\bullet-}$ in pollutant abatement by conventional ozonation and catalytic ozonation with MnO_2 were compared. It reported that high-concentration ROS scavengers (~mM levels of TBA and BQ) in the O_3 system not only quenches their target ROS, but also interrupts the radical chain reaction of O_3 decomposition, blocks the active sites of catalysts, and consumes O_3. These effects can significantly influence the reaction mechanisms of catalytic ozonation. Therefore, the probe approach was used to reveal the realistic role of ROS in catalytic ozonation system by measuring ROS exposure and quantitatively assessing their contribution to pollutant degradation [46]. For instance, by simultaneously monitoring the depletion of $^{\bullet}OH$ probe (4-Chlorobenzoicacid (pCBA)), $O_2^{\bullet-}$ probe (carbon tetrachloride (CCl_4)) and $^1O_2$ probe (metronidazole (MDE)) during catalytic ozonation with MnO_2, the exposures of $^1O_2$, $O_2^{\bullet-}$, and $^{\bullet}OH$ can be calculated by solving Eqs (1.1)-(1.3).

$$ln\left(\frac{[pCBA]_0}{[pCBA]_t}\right) = k_{\cdot OH,pCBA}\int[\cdot OH]\,dt + k_{O_2^{\cdot-},pCBA}\int[O_2^{\cdot-}]dt + k_{1O_2,pCBA}\int[^1O_2]dt + k_{ad,pCBA}t \tag{1.1}$$

$$ln\left(\frac{[CCl_4]_0}{[CCl_4]_t}\right) = k_{\cdot OH,CCl_4}\int[\cdot OH]\,dt + k_{O_2^{\cdot-},CCl_4}\int[O_2^{\cdot-}]dt + k_{1O_2,CCl_4}\int[^1O_2]dt + k_{ad,CCl_4}t \tag{1.2}$$

$$ln\left(\frac{[MDE]_0}{[MDE]_t}\right) = k_{\cdot OH,MDE}\int[\cdot OH]\,dt + k_{O_2^{\cdot -},MDE}\int[O_2^{\cdot -}]dt + k_{^1O_2,MDE}\int[^1O_2]dt + k_{ad,MDE}t \tag{1.3}$$

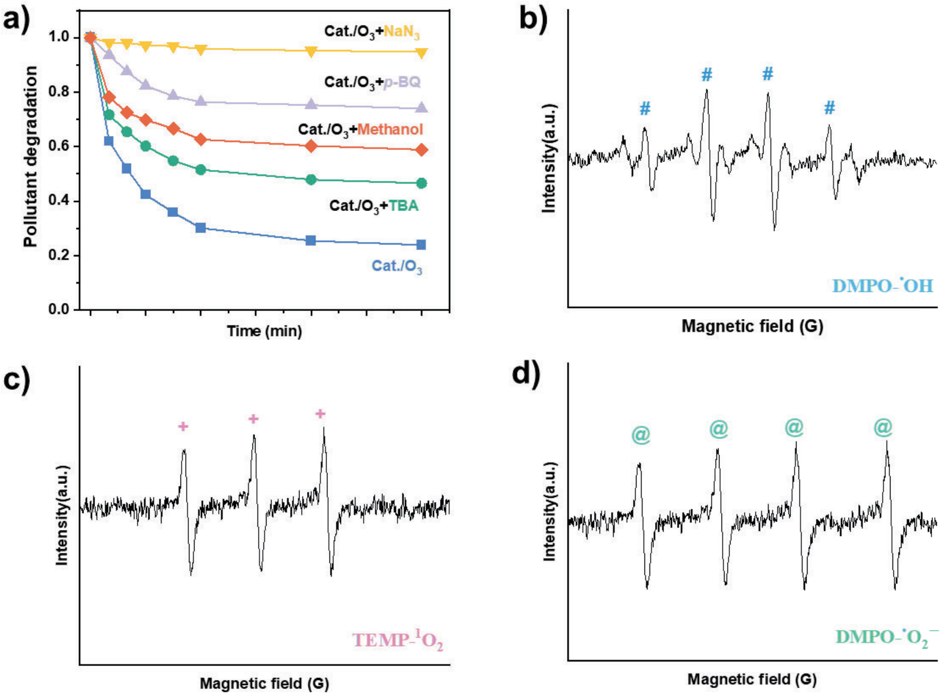

Fig.1.1 (a) Schematic of various scavengers effect in catalytic ozonation system, and ESR spectrum of (b) DMPO-$^{\cdot}$OH, (c) TEMP-$^1O_2$, and (d) DMPO-$O_2^{\cdot -}$.

1.4. Literature review: the application of MnO_2-based materials in HCO

The successful application of MnO_2-based materials in HCO process for pollutant elimination depends on many factors. These include the structure and morphology of MnO_2, the surface properties of the catalysts, and the radicals generated in the system. Some reviews have briefly mentioned the contribution of MnO_2 in different systems for pollutant removal.

1.4.1. The structures and morphologies of MnO_2

Fig.1.2 shows the preparation and application of the various MnO_2/MnO_2-based materials in catalytic ozonation systems for water treatment. The basic unit of MnO_2 crystal structure includes an [MnO_6] octahedron with a Mn atom located at the centre and six oxygen atoms surrounding it [47]. The MnO_6 octahedra connect via edge-sharing to form single chains, producing Mn oxides with diverse structures through edge- and/or corner-sharing [48]. Based on the various connectivity schemes arranged in an m × n rectangular configuration, MnO_2 shows great structural flexibility and appears in a number of crystallographic poly morphs such as α-, β-, γ-, δ-, ε-, and λ- MnO_2 [49, 50] (Fig.1.3). In addition, the synthesize method has a vital impact on the structure and morphology of MnO_2.

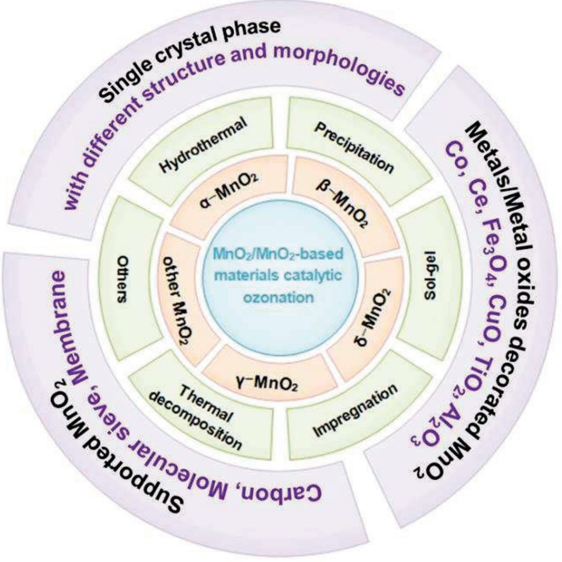

Fig.1.2 A representation of different MnO_2/MnO_2-based materials used for catalytic ozonation system in water.

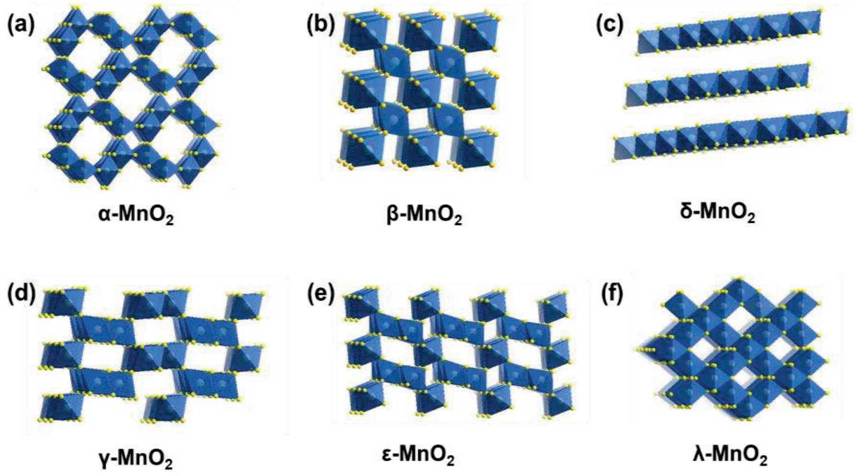

Fig.1.3 Sketch maps of α-MnO_2 (a), β-MnO_2 (b), δ-MnO_2 (c), γ-MnO_2 (d), ε-MnO_2 (e), and λ-MnO_2 (f).

1.4.1.1. α-MnO_2

α-MnO_2 has a rutile structure, consisting of double chains of edge-sharing [MnO_6] octahedra, forming [2 × 2] tunnels with square cross-sections (each side measuring two octahedra of 4.6 Å). This structure can typically host large monovalent, divalent cations, or water molecules for adsorption and further reaction [51]. Wu et al. [52] adopted hydrothermal and H_2 calcination methods to synthesize a series of oxygen vacancy (Vo) modified monometallic α-MnO_2 by varying H_2 atmosphere treatment time. All samples appeared as clusters of nanowires. It was reported that extending the H_2 treatment time facilitated the formation of smaller diameter clusters, which could strengthen the Vo sites exposure of α-MnO_2. Li et al. [53] treated raw $MgMnO_3$ by selective acid etching in all-in-one reaction under normal pressure and temperature to obtain α-MnO_2. Based on the results of N_2 adsorption/desorption isotherm and XRD patterns, it was concluded that highly porous α-MnO_2 nanorods with high specific surface area (271.1 m^2 g^{-1}) were successfully synthesized by sulfonic acid etching for 6 h. However, nitric acid etching could not form any nanorods or nanosheets.

1.4.1.2. β-MnO_2

β-MnO_2, also known as the mineral pyrolusite, features a highly compact crystal structure characterized by channels or tunnels with a width of 1 x 1 (2.3 Å x 2.3 Å) octahedron [54]. These channels facilitate the fast transport and surface adsorption of electrolyte ions due to their appropriate size [55]. Dong et al [56] obtained β-MnO_2 with different morphologies by controlling the hydrothermal temperature. At 100ºC, the morphology of β-MnO_2 was a mixture of nanoneedles and nanoparticles. Higher temperature (150ºC) promoted the growth of β-MnO_2 nanoneedles. When hydrothermal temperature reached 200ºC, uniform and long β-MnO_2 nanowires with larger pore diameter were obtained. The β-MnO_2 nanorods fabricated by Guo et al [57] through the hydrothermal method was non-porous material. However, they displayed low average oxidation state (AOS), which will facilitate O_3 adsorption on the catalyst surface. Due to the reduced resistance, good catalytic properties, biocompatibility, low cost, and excellent electrochemical performance, β-MnO_2

is a versatile and valuable material for applications in catalysis, ion sieves, and electrode materials [54, 56, 58].

1.4.1.3. δ-MnO_2

δ-MnO_2, the primary manganese mineral in hydrogenetic nodules, forms in an oxic environment [59]. It features a typical two-dimensional lamellar structure comprised of [MnO_6] octahedrons sharing common edges. This structure is stabilized perpendicularly by Van der Waals forces from water molecules or ions trapped between the layers [60]. Due to its large interlayer spacing (~7 Å), δ-MnO_2 exhibits a high specific capacity, significant surface electric charge and vacancies, which allows for efficient cation insertion, easy adsorption of metal ions and rare earth elements with positive charges [59, 61]. Ma et al [62] synthesized δ-MnO_2 by reducing $KMnO_4$ in a hydrothermal process, confirming the layer structure of δ-MnO_2 with nanospheres morphology. Due to the special two-dimensional structure of δ-MnO_2, it exhibited a large specific surface area, high Vo content and active site exposure in HCO system. Luo et al [63] further verified that a higher concentration of $KMnO_4$ solution benefits the growth of δ-MnO_2 sheet. When the concentration increased to 0.1 mol L^{-1}, δ-MnO_2 displayed a petal-like sphere morphology consisting of nanoflakes.

1.4.1.4. γ-MnO_2

γ-MnO_2 (nsutite) exhibits an irregular mix structure of 1 x 1 and 1 x 2 tunnels formed by single and double octahedral chains alternately arranged along the c-axis [64, 65]. Its disorder nature with low crystallinity leads to abundant defects and Vo, which are beneficial for promoting the adsorption and activation of O_3 to generate ROS for pollutants removal [51, 65, 66]. Huang et al. [67] employed a precipitation method to prepare hollow nanotube-like γ-MnO_2. This unique hollow structure resulted in a high specific surface area (112.06 m^2 g^{-1}), providing numerous active sites on the surface, which facilitated the adsorption of reactants, thereby enhancing catalytic ozonation activity. Additionally, Itzany J. et al. [51] employed a hydrothermal method to produce spherical γ-MnO_2 consisting of nanorods of various sizes. XPS characterization revealed the presence of abundant Mn^{3+}/Mn^{4+} redox couples in γ-MnO_2, which accelerated electron transfer promoting O_3 decomposition. Owing to its high activity, low toxicity, and low cost, γ-MnO_2 is widely utilized in batteries and catalysts [65, 66].

1.4.1.5. other MnO_2

ε-MnO_2 is structurally very similar to γ-MnO_2 consisting of an intergrowth 1 x 1 pyrolusite and 2 x 1 ramsdellite phases [67]. However, ε-MnO_2 exhibits more structural faults (De Wolff faults) and structural defects (micro-twin) than the γ-phase, resulting in its low crystallinity [68]. Thanks to its unique 3D framework with interconnected tunnels, ε-MnO_2 provides a high surface area, efficient oxygen diffusion, and good stability during cycling, making it widely applicable in fields such as supercapacitors, catalysis, and sensors [69, 70]. Hong et al. [71] fabricated ε-MnO_2 catalyst via selective dissolution of Mn-Li precursors producing more manganese vacancies, and thus better oxygen storage capacity, superior reducibility, and higher Vo, which resulted in excellent activity and stability for O_3 decomposition. However, its catalytic ozonation performance in water treatment has been rarely reported.

λ-MnO_2 features a unique three-dimensional network of tunnels, which might provide abundant surface-active oxygen species via the cycling of Vo [72, 73]. Spinel λ-MnO_2 has been described with strong capacities of electron transfer and rapid ions diffusion [74], making it highly applicable as a material for metal-air batteries [75], anodic materials [76], supercapacitors [77], fuel cells [78], and catalytic water oxidation [73]. To the best of our knowledge, there is little research on λ-MnO_2 as a catalyst in catalytic ozonation reactions for water purification. The crystal form, structure, property, and application field of different MnO_2 were concluded in Table 1.1. The synthesis methods and catalytic performances of various crystal MnO_2 are summarized in Table 1.2

Table 1.1 Comparison of MnO_2 crystal forms, structures, properties, and application.

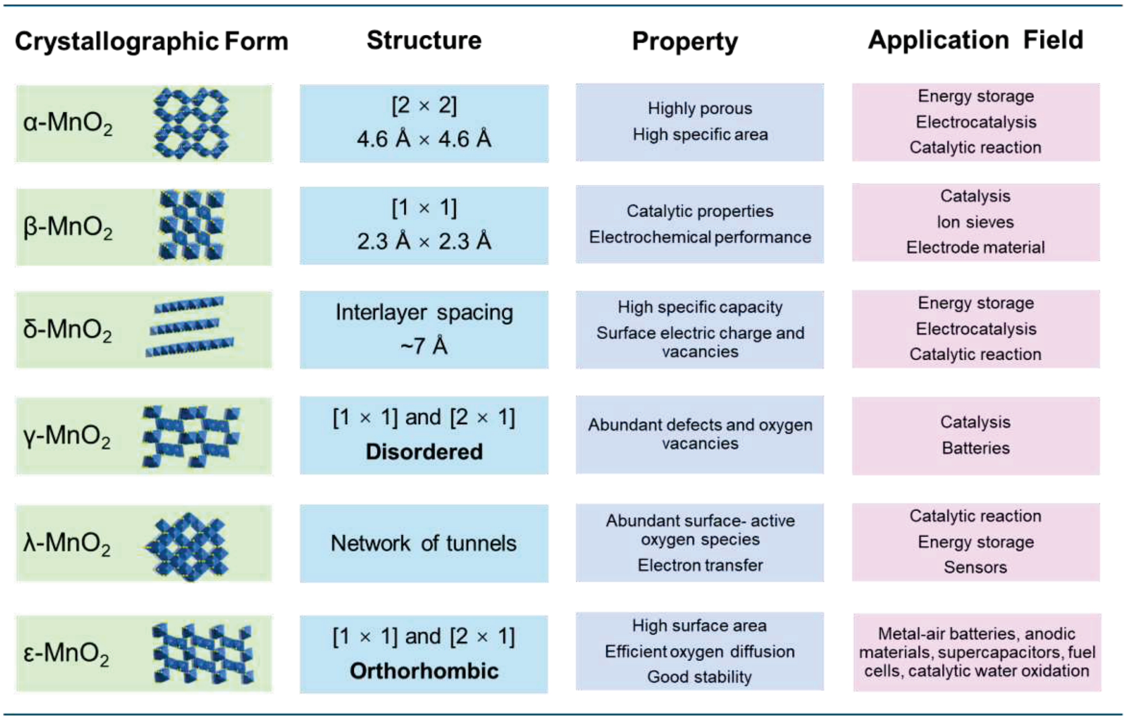

Crystallographic Form	Structure	Property	Application Field
α-MnO_2	[2 × 2] 4.6 Å × 4.6 Å	Highly porous High specific area	Energy storage Electrocatalysis Catalytic reaction
β-MnO_2	[1 × 1] 2.3 Å × 2.3 Å	Catalytic properties Electrochemical performance	Catalysis Ion sieves Electrode material
δ-MnO_2	Interlayer spacing ~7 Å	High specific capacity Surface electric charge and vacancies	Energy storage Electrocatalysis Catalytic reaction
γ-MnO_2	[1 × 1] and [2 × 1] **Disordered**	Abundant defects and oxygen vacancies	Catalysis Batteries
λ-MnO_2	Network of tunnels	Abundant surface- active oxygen species Electron transfer	Catalytic reaction Energy storage Sensors
ε-MnO_2	[1 × 1] and [2 × 1] **Orthorhombic**	High surface area Efficient oxygen diffusion Good stability	Metal-air batteries, anodic materials, supercapacitors, fuel cells, catalytic water oxidation

In conclusion, a variety of techniques are frequently used to create distinct crystalline forms of MnO_2, such as hydrothermal synthesis, precipitation, impregnation, and sol-gel. The size, shape, and pore volume of the final product are greatly influenced by critical preparation parameters like temperature, pH, and time. The multidimensional morphology, porous structure, and large surface specific area of α-, β-, γ-, and δ-MnO_2 make them more commonly utilized in HCO systems than other MnO_2 catalysts.

Table 1.2 Various methods for synthesizing MnO_2/MnO_2-based materials used in catalytic ozonation system.

Method	Material	Target	Activity	Ref.
Hydrothermal	α-MnO_2	Atrazine	96.5%	[52]
	α-MnO_2	Phenol	94.9%	[84]
	α-MnO_2	Phenol	69%	[50]
	β-MnO_2	Phenol	55%	
	γ-MnO_2	Phenol	55%	
	α-MnO_2	Ciprofloxacin	93.1%	[42]
	β-MnO_2	Ciprofloxacin	82.3%	
	γ-MnO_2	Ciprofloxacin	75%	
	β- MnO_2	Phenol	83.7%	[56]
		Mineralization	Increased 27.1%	
	α-MnO_2	Ibuprofen TOC	50%	[123]
	β-MnO_2	Ibuprofen TOC	37%	
	δ-MnO_2	Sulfachloropyridazine	0.105 min^{-1}	[62]
	γ-MnO_2	TOC of Bisphenol A	51%	[51]
Co-precipitation	γ-MnO_2	Phenol	98.14%	[67]
	Fe_3O_4/MnO_2	p-cresol	99.5%	[103]
		p-chlorophenol	93.9%	
Redox precipitation	MnO_2	COD of wastewater-biotreated	47.39%	[120]
Acid etching	α-MnO_2	4-chlorophenol	86.9%	[53]
Surfactant	α-MnO_2	4-nitrophenol	99.3%	[121]
Impregnation	MnO_2/γ-Al_2O_3	Sulfamethazine	99.9%	[95]
	Cu-Mn-Ce@ γ-Al_2O_3	COD of wastewater-biotreated	61%	[94]
Sol–gel	MnO_2/TiO_2	Phenol	64.7%	[122]

1.4.2. Application of MnO_2-based catalysts

The structure of MnO_2 is very versatile because of the varied connections and arrangement of the fundamental structural unit [MnO_6]. Because of its special design, which makes it easier for O_3 to adsorb, diffuse, and decompose, it has exceptional catalytic efficacy and is frequently used to remove contaminants from water.

1.4.2.1. Single MnO_2 catalysts

1) The influence of MnO_2 crystal phase

The crystal phase is an important factor determining the activity of MnO_2, but different reaction systems have yielded varying conclusions. Nawaz et al. [49] successfully synthesized α-, β-, γ-, δ-, ε-, and λ-MnO_2 catalysts and investigated the catalytic ozonation performance for 4-NP degradation. α-MnO_2 was found to be the most active catalyst for 4-NP removal (99.3%) at neutral pH. The lower average oxidation state of α-MnO_2 meant a higher ratio of Mn^{3+}/Mn^{4+}, which enables more oxidation/reduction cycles, thereby improving the electron transfer and enhancing the catalytic decomposition of O_3 to generate ROS.

He et al [79] obtained α-, β-, and γ-MnO_2 catalysts by the hydrothermal method, which exhibited nanofiber, nanotube, and quasi-flower shapes, respectively (Fig.1.4). Compared to β-, and γ-MnO_2 catalysts, α-MnO_2 demonstrated the highest catalytic performance with 99% degradation efficiency for ibuprofen (IBU) and metoprolol. Characterization results showed that α-MnO_2 contained higher oxygen reduction capacity and migration ability, making it easier to generate Vo and surface adsorbed oxygen (O^{2-}, O^-, OH^-). The presence of abundant Vo and surface adsorbed oxygen could facilitate the adsorption of O_3 on the catalyst surface, which then self-decomposed to product more ROS accelerating pollutants degradation. The MnO_2 with different crystal forms exhibits different electron transfer ability, oxygen reduction ability, and Vo content, resulting in various catalytic activities and inconsistent action mechanisms.

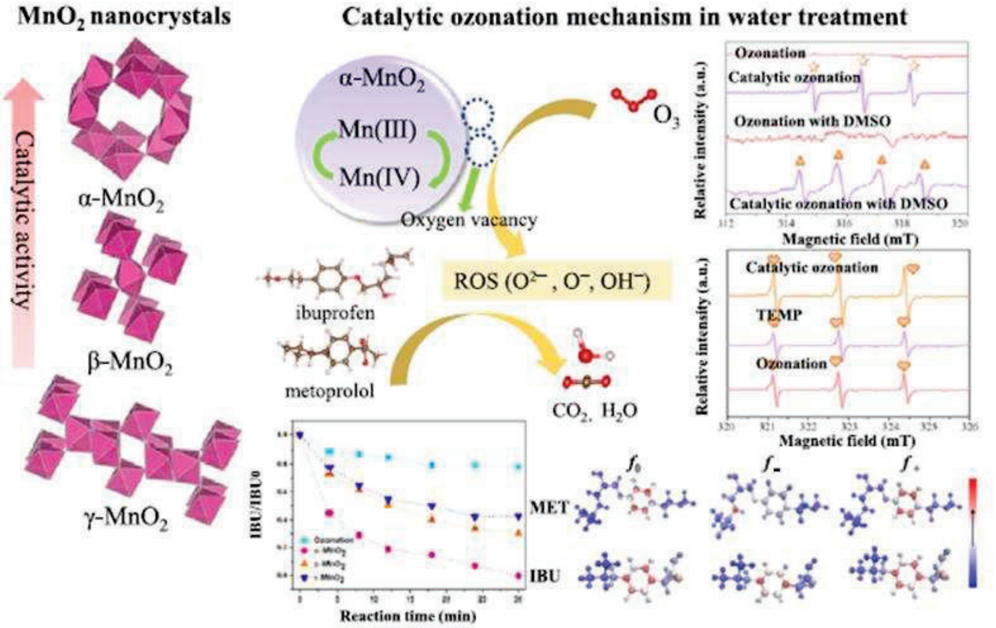

Fig.1.4 The proposed catalytic ozonation mechanism of different MnO$_2$ nanocrystals. Reproduced from [6]. **Copyright 2024 with permission from Elsevier.**

2) The influence of different facets

Some researchers have found that by controlling the growth conditions of MnO$_2$ crystals, some active crystal facets with highly unsaturated coordination atoms can be preferentially exposed to reactants. The exposure of more undercoordinated atoms and/or the easy formation of Vo can induce O$_3$ decomposition into ROS over the crystal facets, thereby, effective catalyzing O$_3$ to degrade a wide range of refractory pollutants. Li et al. [53] prepared highly porous α-MnO$_2$ by selective acid etching from Mn-containing spinel, which achieved more than 90.9% of 4-chlorophenol degradation within 12 min by catalytic ozonation. DFT theory calculations revealed that α-MnO$_2$ with (110) facet promotes the adsorption and activation of ozone directly over the defects or indirectly over H$_2$O adsorbed on the defects. Thus, more ROS were generated and got involved in pollutant degradation.

3) The influence of various MnO$_2$ morphologies

Different morphologies of MnO$_2$ significantly influence the number of exposed active sites, directly impacting their catalytic performance [80]. As displayed in Fig.1.5, commonly, 3D (such as nan nanoflowers, nanospheres, and hollow nanospheres) [81, 63, 82] and 2D structures (nanosheets) [83] possess more abundant pore structures and larger surface areas compared to 1D nonporous catalysts (such as nanowires, nanorods, and nanotubes) [84, 56]. Consequently, researchers are committed to fabricating MnO_2 with different morphologies to increase the exposure of surface-active sites and enhance the mass transfer of pollutants in the porous structure, thereby improving catalytic performance.

Dong et al. [56] prepared β-MnO_2 catalyst in various morphologies, including nanowires, dandelion-like structures, and commercial bulk forms, and compared their catalytic ozonation performance for phenol removal. Amongst, β-MnO_2 nanowires exhibited good separability with higher sedimentation (8.2×10^{-2} cm s^{-1}) and larger specific surface area (73.54 m^2 g^{-1}), which are important advantages as catalyst for catalytic ozonation. In addition, Zarei et al. [85] used nano-MnO_2 as ozonation catalysts instead of simple MnO_2 significantly enhancing the removal efficiencies to 82% for COD and 100% for color in real petrochemical wastewater. It was proved that the particle size range of nano-MnO_2 shifted to a finer range, providing a better morphology to achieve a more available surface of the catalyst.

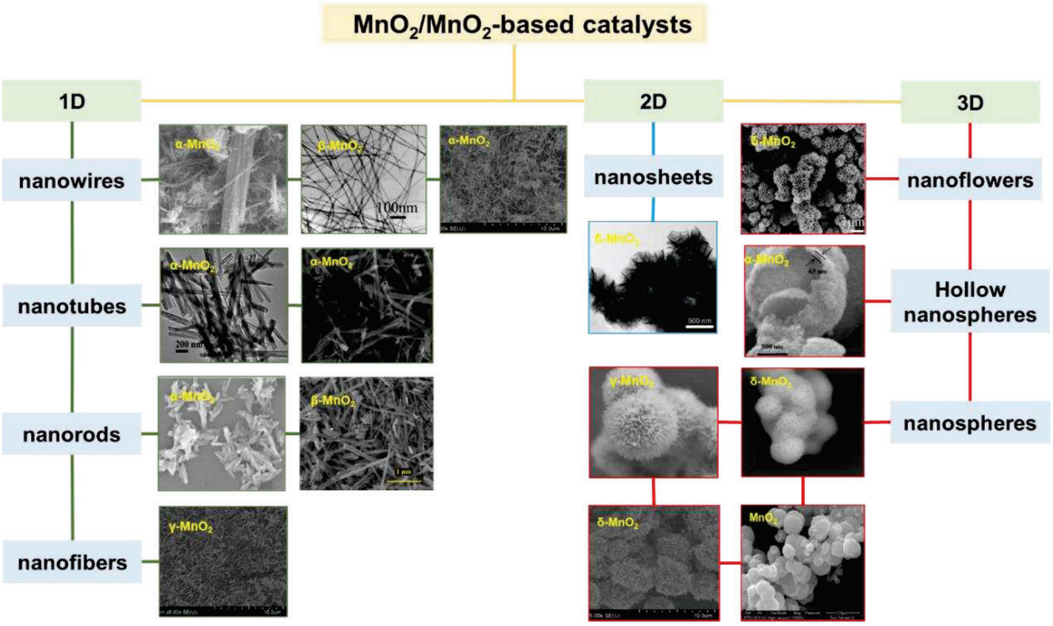

Fig.1.5 The overview of SEM images of MnO_2 with various morphologies.

1.4.2.2. Metal/metal oxides decorated MnO_2 composite catalyst

With the increasing application of MnO_2 in water treatment, the demand for its catalytic properties is also rising. However, the crystal structure, specific surface area, Mn-O bond strength, and other aspects of MnO_2 are not ideal for effective utilization in water purification. Therefore, multicomponent catalysts based on MnO_2 are considered to improve stability, create more available active sites, and reduce metal ion leaching of catalyst, thus enhancing its catalytic ozonation capacity.

1) Metal doping MnO_2 catalyst

Metal ion doping modifies the intrinsic properties of MnO_2 by introducing ions into its lattice [86]. When a metal ion dopant with a different valence state replaces another ion in the lattice, it creates charge defects and Vo. These changes affect the morphology, specific surface area, and oxygen mobility of MnO_2, significantly influencing the O_3 decomposition pathway [87]. For example, Zhang et al. [88] fabricated a cobalt-doped-α-MnO_2 catalyst through a hydrothermal method, which significantly improved the phenol removal to 97.47 % after 40 min. Compared to α-MnO_2, Co-α-MnO_2 has larger specific surface area (79.496 m^2/g) and pore volume (0.0396 cm^3/g), higher adsorbed oxygen content (18.99 %) and Mn^{3+} relative content (41.16 %). Additionally, the Vo content, lattice defect content, and surface -OH content of Co-α-MnO_2 are higher than those of α-MnO_2, resulting in higher catalytic ozonation performance of Co-α-MnO_2. Similarly, Zhang et al. [89] prepared an $MnCe_xO_y$ catalyst by α-MnO_2 doped with Ce^{3+} and employed it in an ozonation system for quinoline degradation. It confirmed that the $MnCe_xO_y$ catalyst had a larger specific surface and higher contents of O_s and Mn^{3+} than α-MnO_2, which promoted O_3 decomposition and ROS generation.

2) MnO_2/metal oxides catalysts

Combing with other metal oxides is also a good strategy to synthesize multicomponent catalysts for enhancing the catalytic performance of MnO_2. TiO_2, one of the most commonly used materials, has attracted increasing attention due to its high chemical inertness, environmental friendliness, good thermal stability, and strong electron transfer ability [90, 91]. Cristina et al. [92, 93] used MnO_2/TiO_2 as catalyst in catalytic ozonation removal of pentachlorophenol (PCP). The characterization results showed the presence of crystalline-, rutile- and anatase-TiO_2 phases. The catalytic ozonation process not only allowed for higher mineralization of PCP, but also resulted in lower toxicity compared to the initial solution.

Alumina (Al_2O_3) has been extensively studied as a catalyst due to its environment friendless, structural stability, high industrial feasibility, and low cost [94, 95]. Gao et al. [96] compared four metal oxides loaded on Al_2O_3 catalyst, finding that $MnO_2/\gamma\text{-}Al_2O_3$ had the best catalytic performance with 88.4% of mineralization of acetic acid wastewater in 300 min. This was attributed to the $MnO_2/\gamma\text{-}Al_2O_3$ catalyst's efficiency in converting O_3 into ROS such as $^{\bullet}OH$ and O_2^{-} in the solution and O_2^{2-} on the catalyst surface. Liu et al. [97] prepared the granular MnO_2/Al_2O_3 catalyst, which achieved 95% of quinoline and 65% of TOC degradation in 90 min, respectively. In addition to the direct loading of MnO_2 onto Al_2O_3, many researchers have focused on synthesizing metal/metal oxide-MnO_2/Al_2O_3 composite catalysts, such as $MnO_2\text{-}CuO/\gamma\text{-}Al_2O_3$ [98], Cu-Mn-Ce@$\gamma\text{-}Al_2O_3$ [64], and $MnO_x\text{–}CeO_x/\gamma\text{-}Al_2O_3$ [99-101]. The addition of Cu and Ce elements can growth active facet of MnO_2, promote the synergistic effect of bimetallic and improve the stability of catalysts.

Furthermore, Zhang et al. [102] reported that $Fe_3O_4\text{–}MnO_2/O_3$ system could achieve excellent BPA degradation, which was much higher than other systems including Fe_3O_4/O_3, $Fe_3O_4\text{-}MnO_2$ and $Fe_3O_4\text{-}MnO_2/O_2$. The $Fe_3O_4\text{-}MnO_2$ catalyst had a large specific surface area, allowing it to adsorb more O_3 on its surface for further reactions. Nawaz et al. [103] fabricated $Fe_3O_4\text{-}MnO_2$ catalyst with abundant porosity, high surface area, and multiple components, providing more reaction sites on the surface. This resulted in excellent activity in catalytic ozonation and mineralization of cresol and chlorophenol. Other metals oxides such as Co_3O_4 and CuO have also been proven to be effective choices for preparing multicomponent-Mn catalyst. These oxides can enhance O_3 mass transfer, improve O_3 exposure, and increase O_3 utilization efficiency, thereby promoting the catalytic ozonation performance [104, 105].

1.4.2.3. Effect of various carriers on MnO_2-based catalyst

An efficient catalyst support is characterized by a high specific surface area and a robust structure, enabling the effective dispersion of active sites, minimizing metal agglomeration, and offering a porous framework that facilitates catalytic reactions while reducing mass transfer resistance. Consequently, selecting a suitable support can significantly improve the catalytic performance and resistance to neutral toxicity of the catalyst.

1) Carbon material

Pure metal oxides may cause problems such as the aggregation of metal oxide nanoparticles and metal leaching in the solution, consequently hindering the efficiency of catalytic ozonation. Therefore, the combination of MnO_2 with non-metallic materials was considered to suppress the Mn ion leaching issue, prevent the agglomeration of Mn oxides, and overcome the high energy barrier from reduction of $M^{(n+m)+}$ to M^{n+} (M, metal species), thus significantly improving the activity of catalyst in catalytic ozonation process.

Activated carbon (AC) emerges as an ideal non-metallic material due to its numerous surface chemical functional groups, abundant reserve, stable chemical properties, potential for solid waste recycling, carbon sequestration, huge adsorption capacity and low cost [90, 106]. Developing a catalyst that can enhance the interaction between metal active sites and AC is of strong practical significance. Gong et al. [107] synthesized different crystalline phase structures of MnO_2 loaded onto AC using a hydrothermal synthesis-calcination method. Compared with MnO_2 alone, α-MnO_2/AC possessed lower polarization resistance, faster charge transfer rate, and higher Mn^{3+} and Vo contents, thus accelerating the production rate of radicals, achieving 96.27% of bromamine acid degradation in catalytic ozonation process.

Graphene/reduced graphene oxide (GO/rGO) with special 2D structure performs preeminent chemical stability, electrical conductivity and surface to volume ratio, drawing abundant research attention as a catalyst support for metal oxide [108]. Wang et al. [109] successfully fabricated a 2D γ-MnO_2/rGO structure catalyst via a facile low temperature hydrothermal method. The commercial MnO_2 and alone rGO degraded 50 mg/L of 4-NP in 60 min in the catalytic ozonation process, while the as-prepared MnO_2/rGO composite only took 30 min. It was confirmed that the high catalytic performance of MnO_2/rGO could be attributed to the large amounts of active sites which could generate more radicals in catalytic ozonation process.

2) Membrane

In recent years, coupling heterogeneous catalytic ozonation technology with membrane filtration has been considered a promising solution for treating micropollutants in water [110]. However, membrane fouling and insufficient removal of small organic molecules remain critical obstacles limiting its further widespread application [111]. To solve these problems, surface modification of membranes with functional materials has recently drawn much attention in combined O_3-membrane systems [112]. Cheng et al. [111] utilized three types of MnO_2 to prepare Mn oxide incorporated membranes: commercially available MnO_2 (C-MnO_2), and lab synthesized MnO_2 using $MnCl_2$ precursor (M-MnO_2) and $Na_2S_2O_3$ precursor (S-MnO_2). The catalytic ozonation performance of S-MnO_2 incorporated membrane towards *p*-chloronitrobenzene degradation (68.0%) was higher than that of the M-MnO_2 incorporated membrane (61.5%) and the C-MnO_2 incorporated membrane (51.7%). S-MnO_2 exhibited the best dispersibility and smallest particle size, facilitating that more MnO_2 particles incorporate to membrane pores increasing membrane intrinsic resistance and lessening membrane flux. In the presence of O_3, the radicals generated by catalytic membranes would enhance ozonation of foulants deposited in the pores. Moreover, the incorporation of small particles would reduce membrane surface roughness, decreasing the accumulation of contaminants on the valleys of membrane surface, thus reducing membrane fouling.

3) Molecular sieves

The decomposition of O_3 on carbon material surfaces leads to additional $^{\bullet}OH$ generation. However, when exposed to high O_3 concentrations, carbon materials lose active sites for aqueous O_3 decomposition, indicating low stability of carbon-based catalyst [113]. In contrast, mesoporous molecular sieves (such as MCM-41, SBA-15, ZSM-5, and MCM-48) exhibit larger specific surface areas, higher thermal stability, and porosity, providing greater exposure of active sites for interfacial reactions [114, 115]. Sun et al. [116] adopted an incipient impregnation method to get MnOx/SBA-15 material for OA removal in catalytic ozonation system. The MnOx-2%/SBA-15 (Mn:SBA-15 weight ratio was 2%,) achieved 84.6% removal of OA in 60 min. Sui et al. [81] prepared MnOx-0.01/MCM-41 (the ratio of Mn/Si was 0.01) catalysts through impregnation, obtaining 88.9% of catalytic ozonation degradation of nitrobenzene. Besides, based on the combination of hydrothermal and solid-state reaction method, Hong et al. [117] loaded α-MnO_2 on ZSM-5 for the catalytic ozonation of toluene. However, to the best of our knowledge, the utilization of MnO_2 loaded on the mesoporous molecular sieve in HCO system for water treatment has been seldom reported.

1.4.3. The mechanisms of catalytic ozonation by MnO_2-based catalysts

Based on aforementioned results, the contaminant degradation process in HCO system by MnO_2-based catalysts can be summarized in three ways. 1) Pollutant molecules are absorbed on the catalysts surface and are degraded subsequently by O_3 or generated active species. 2) O_3 react with surface-active groups of catalysts producing ROS. These ROS, along with O_3, then engage in chemical reactions with the pollutant molecules present in the solution. 3) Both O_3 and pollutant molecules are adsorbed onto the catalyst surface at the same time for further reaction. The catalytic ozonation process involves several theories, and the mechanisms can be explained as follows:

1) Physical properties theory

The specific surface area, pore size, and pore volume of MnO_2/MnO_2-based catalysts are influenced by their physical characteristics, which include their crystalline phase, particle size, shape, and composition. These characteristics have a direct impact on active site exposure, which affects the adsorption ability of catalyst and O_3 activation. Ma et al. [62] used a hydrothermal method to create various δ-, α-, γ-, and β-MnO_2. The XRD characteristic peaks of α- and β-MnO_2 were sharp and straight, indicating big particle size and good crystallinity. γ- and δ-MnO_2 exhibited a larger spectral band, smaller particle size, and reduced crystallinity. These different structures result in varying catalytic ozonation efficiencies. The rate constant of SCP degradation by MnO_2 was in the order δ- (0.105 min^{-1}) > α- (0.077 min^{-1}) >γ- (0.063 min^{-1}) > β-MnO_2 (0.062 min^{-1}). Besides, due to a higher pore volume and BET surface area (159.6 m^2 g^{-1}), the adsorption capacity (less than 8%SCP in 60 min) of δ-MnO_2 was higher than the other phases of MnO_2. The trend of SCP degradation rate was consistent with BET surface areas. Therefore, it is believed that the BET surface area partly determines the catalytic performance of different MnO_2.

2) Oxygen vacancy (Vo) theory

During the oxidation/reduction reaction between the different Mn species, Vo are produced to balance the charge because of the downshift of high valence Mn (Mn^{4+}) [53]. Vo have the ability to accept and donate electrons, creating electron transfer channels throughout the catalysts. This excellent electron transfer property allows Vo to alleviate the passivation of catalysts promoting the redox cycle of Mn species [52]. Additionally, Vo integrated into the crystal structure of MnO_2/MnO_2-based catalysts can also regulate the inherent electronic configuration, ultimately promoting the catalytic sites exposure. Furthermore, due to the high surface energy of Vo, the activity of the oxygen exchange ‘surface’ can be reduced, potentially enhancing the adsorption of O_3 and H_2O onto the catalytic surface, thus promoting the utilization of O_3 [117]. As potential catalytic active sites, Vo can induce the generation of some other ROS, including $O_2^{\bullet-}$, $^1O_2$, and $^{\bullet}OH$, in the presence of O_3 (Eqs. (1.4)-(1.7)) [51, 52]. Constructing and modulating surface and bulk Vo over MnO_2 is an effective modification method to boost catalytic ozonation performance. The reaction mechanism is displayed in Fig.1.6.

$$O_3 + V_o \rightarrow O^{2-} + O_2 \tag{1.4}$$

$$O^{2-} + O_3 \rightarrow O_2^{2-} + O_2 \tag{1.5}$$

$$O_2^{2-} \rightarrow O_2 + V_o \tag{1.6}$$

$$O_2^{2-}/ O^{2-} + H_2O \rightarrow [{}^1O_2/O_2^{\cdot -}/{}^{\cdot}OH] \qquad (1.7)$$

3) Redox couple theory

In the catalytic ozonation process, MnO_2 has multi-valence Mn species such as Mn^{4+}, Mn^{3+}, and Mn^{2+}.Lower valence Mn species tend to reach a higher valence after being subjected to ozonation. Due to the existence of two redox couples Mn^{4+}/Mn^{3+} (0.95 eV) and Mn^{3+}/Mn^{2+} (1.50 eV), the oxidation/reduction reactions occur easily between various Mn valence states [82]. The transition of $Mn^{4+}/Mn^{3+}/Mn^{2+}$ involving electron transfer can promote O_3 decomposition to generate more active oxygen species, which are responsible for the catalytic reactions (Eqs. (1.8)-(1.12)) [83, 118]. Itzany J. et al. [51] compared the ratio of Mn^{3+}/Mn^{4+} between α-MnO_2 and γ-MnO_2 through XPS analysis. They demonstrated that γ-MnO_2 showed a higher ratio (1.4) than α-MnO_2 (0.79). The existence of a higher Mn^{3+}/Mn^{4+} ratio would accelerate O_3 decomposition by adsorbing O_3 molecules on the surface to form intermediate oxygen species, thus enhancing the generation of ROS to increase pollutants degradation. To improve redox cycling capability between muti-valent Mn species, additional metals and/or metal oxides were incorporated into MnO_2. Nawaz et al. [103] fabricated a mesoporous Fe_3O_4/MnO_2 composite for phenolic mixture degradation, which had better activity than Fe_3O_4 and MnO_2 alone. There were two redox couples (Mn^{3+}/Mn^{4+} and Fe^{2+}/Fe^{3+}) existing in the structure of catalyst. Firstly, O_3 would oxidize Mn^{3+} to Mn^{4+}, then the presence of Fe^{2+} in the composite could reduce the Mn^{4+} back to Mn^{3+} ($E_{Fe3+/Fe4+}$=0.77 eV). The redox reactions between multivalent metal ions promote the generation and transfer of electrons, thereby enhancing the decomposition of ozone. The reaction mechanism is displayed in Fig.1.6.

$$4Mn^{4+} + O^{2-} \rightarrow 2Mn^{4+} + 2Mn^{3+} + V_o + \frac{1}{2}O_2 \qquad (1.8)$$

$$2Mn^{3+} + 2H_2O \rightarrow Mn^{4+} + Mn^{2+} + O^{2-} + 4H^+ \qquad (1.9)$$

$$[Mn^{4+}/Mn^{3+}] \overset{e^-}{\Leftrightarrow} [Mn^{3+}/Mn^{2+}] \qquad (1.10)$$

$$O_3 + e^- \rightarrow O_2^{\cdot-} + O_2 \qquad (1.11)$$

$$e^- + O_2 \rightarrow O_2^{\cdot-} \qquad (1.12)$$

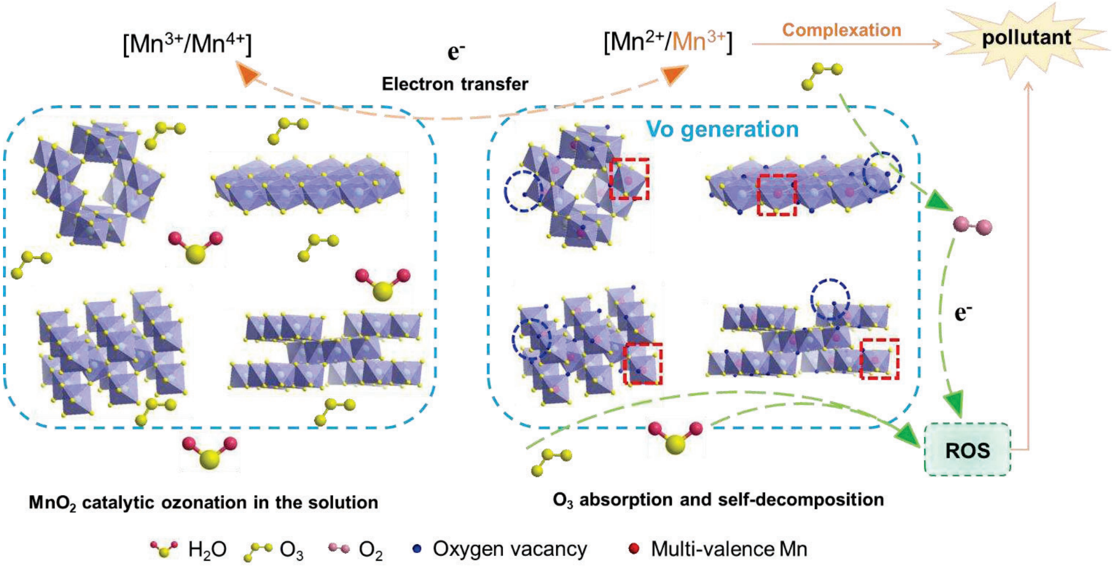

Fig.1.6 Mechanism analysis of catalytic ozonation by MnO_2/MnO_2-based catalysts involving Mn species and Vo generation.

4) Complexation theory

In α-MnO_2/O_3 system, Tian et al [118] pointed out that there is adsorption of terminal oxygen atom of O_3 on the weak Lewis acid sites of α-MnO_2 surface to form long-lived Mn-O_3* complexes based on in situ DRIFTS experiments. Then, the electron flow from the highest occupied molecular orbitals (HOMOs) of pollutants (P) with low φ1/2 to the lowest unoccupied molecular orbitals (LUMOs) of metastable Mn-O_3* complexes led to the formation of oxidized pollutants (POX) and the decomposition of the Mn-O_3* complexes to give free $O_2^{\bullet-}$ and/or adsorbed peroxide (*O_2), accompanied by the regeneration of α-MnO_2 (Eqs. (1.13)-(1.14)).

$$\alpha\text{-}MnO_2 + O_3 \rightarrow \text{Mn-}O_3^{*} \text{ complexes} \qquad (1.13)$$

$$\text{Mn-}O_3^{*} \text{ complexes} + P \rightarrow O_2^{\cdot-}/\,^{*}O_2 + MnO_2 + P_{OX} \qquad (1.14)$$

5) Surface hydroxyl groups theory

In the aqueous environment, water molecules (H_2O) coordinate with Lewis acids (like Vo and metal ions) on the surface of MnO_2/MnO_2-based catalysts, The H_2O molecules then dissociate, forming surface -OH and H^+ on the catalyst surface (Fig.1.7). The surface -OH groups may serve as the main active sites for MnO_2/MnO_2-based catalysts, facilitating the absorption and subsequent decomposition of O_3 to generate radicals [56]. The highly active surface resonance structure of O_3 coordinates with surface -OH to form a five-membered ring structure, which subsequently decomposes to release O_2 and produce surface HO_2^- [119]. The formed HO_2^- further reacts with O_3 generating $O_3^{\bullet-}$ and $HO_2^{\bullet}$ which are then converted to $O_2^{\bullet-}$ by releasing H^+. Meanwhile, $O_2^{\bullet-}$ is oxidized by O_3 to form $O_3^{\bullet-}$ and O_2. Additionally, H^+ combines with $O_3^{\bullet-}$ to form $HO_3^{\bullet}$ which further decomposes to produce $^{\bullet}OH$ and O_2 [96]. Finally, surface cations are formed from $O_2^{\bullet-}$ in the presence of H_2O, which in turn form surface hydrated cations (H_2O^+) that are subsequently converted to surface -OH, hence, completing the surface -OH regeneration (Eqs. (1.15)-(1.20)). To recognize the role of surface -OH of catalysts, Zhang et al. [88] employed HPO_4^{2-} to occupy surface -OH, thereby deactivating the catalytic activity. The degradation rate of phenol obtained by O_3/Co-α-MnO_2 was 64.58%, which was reduced by 32.89%. In conclusion, surface -OH groups play a key role in catalytic ozonation processes.

$$[MnO_2] + H_2O \rightarrow [MnO_2]\text{-}OH + H^+ \quad (1.15)$$

$$[MnO_2]\text{-}OH + O_3 \rightarrow HO_2^- + O_2 \quad (1.16)$$

$$HO_2^- + O_3 \rightarrow HO_2^{\cdot} + O_3^{-\cdot} \quad (1.17)$$

$$HO_2^{\cdot} \rightarrow H^+ + O_2^{-\cdot} \quad (1.18)$$

$$O_2^{-\cdot} + O_3 \rightarrow O_3^{-\cdot} + O_2 \quad (1.19)$$

$$O_3^{\cdot-} + H^+ \rightarrow HO_3^{\cdot} \rightarrow \cdot OH + O_2 \qquad (1.20)$$

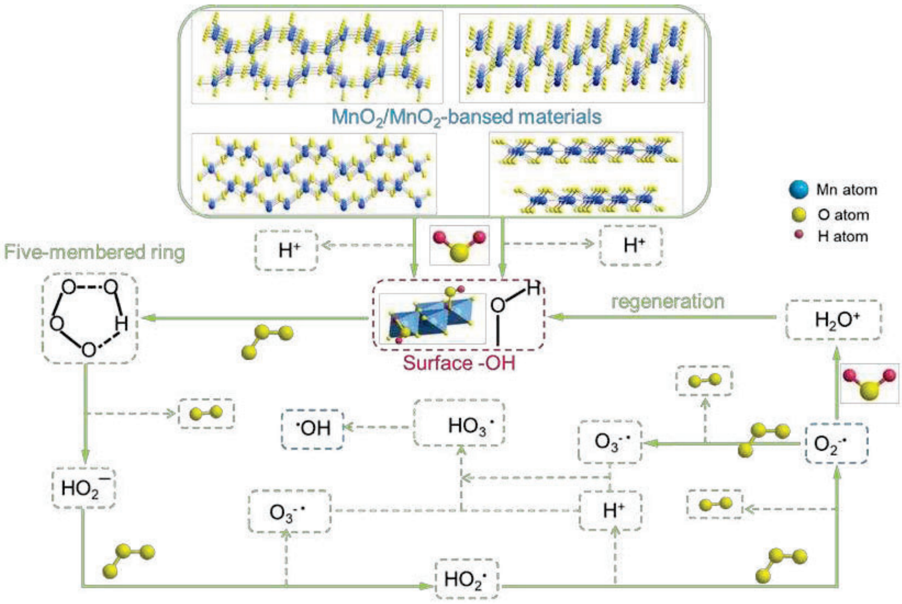

Fig.1.7 Mechanism analysis of catalytic ozonation by MnO_2/MnO_2-based catalysts involving the influences of surface -OH.

1.4.4. Conclusion from the literature review

MnO_2 as one of the most promising catalysts used in HCO system exhibits excellent activity for pollutant degradation. Due to its different crystal phase structures (α-, β-, γ-, δ-, ε-, and λ-), the function of MnO_2 such as specific surface area, redox properties, surface functional group types, and adsorption modes are various, thereby, impacting the catalytic performance and causing complex degradation mechanisms. In addition, some studies report that the generation of Mn-complex in the catalytic ozonation can enhance the pollutant removal efficiency. However, the relevant complex theory is still not known and in-depth evaluated. Therefore, exploring the formation of MnO_2-complexes, investigating the catalytic process, as well as clarifying the catalytic mechanism of MnO_2 complexes in HCO system for pollutant elimination, is of great significance for enhancing the application of MnO_2 catalysts.

CHAPTER 2

Objectives and thesis structure

2.1. Motivation and objectives

Nowadays, micropollutants (MPs) have often been detected in aquatic environment at ng L^{-1} to μg L^{-1} levels, significantly influencing the environment and human health. To remove stubborn compounds in wastewater, heterogeneous catalytic ozonation has drawn an increasing attention owing to its several advantages such as shorter reaction time, high O_3 availability, and efficient pollutant degradation rate.

Manganese dioxide (MnO_2) catalysts have become a research hotspot because of its non-toxicity, high specific capacitance, and cheap cost. Due to its diverse crystal structures, the catalytic ozonation mechanisms of MnO_2 catalysts are different. In addition, some studies revealed that the complexation between metal oxide and organic acids can improve pollutant removal, but the complex study in HCO system is seldom mentioned. Therefore, this thesis focused on investigating the roles of MnO_2-acid complexes in catalytic ozonation for enhanced micropollutants abatement in water. To reach this general objective, the following specific goals are proposed:

- Improving the synthesis method of composites to obtained different crystalline forms of MnO_2 catalysts (α-, β-, and δ-MnO_2) for pollutant removal to evaluate catalytic performance.
- Optimize operation parameters (such as catalyst dosage, initial pollutant concentration, O_3 concentration and pH) to improve the effective utilization of catalysts and O_3, selecting the best catalytic system.
- Study the effect of OA presence on the formation of MnO_2-OA complexes and evaluate the co-degradation efficiency of pollutants in the Cat/OA/O_3 system.
- Through systematic characterization techniques (such as XRD, FT-IR, SEM, XPS, O_2-TPD, and *etc.*), explore the electron transfer ability and redox property of complexes, and analyze the effect of MnO_2 crystal forms on MnO_2-OA complex catalytic activity.

- Determine the type of reactive oxygen species (ROS) and the contribution of various ROS in Cat/OA/O_3 systems through scavenger experiments, electron spin resonance (ESR), and probe experiments.
- Elaborate the interfacial mechanisms of different Cat/OA/O_3 systems.

2.2. Thesis structure

The aim of this thesis was to address the current gaps in understanding the role of MnO_2-acid complexes in catalytic ozonation, along with determining the physicochemical properties of MnO_2-acid complexes and quantifying the contribution of various ROS in HCO process. To achieve this goal, the main contributions of this thesis were organized into four chapters.

Chapter 1: Introduction

Currently, the existence of emerging micropollutants in the environment has become a pressing global issue. HCO as one of the recommended AOPs has been confirmed to be an efficient strategy for more efficient mineralization and the fast degradation of refractory organic compounds. The selection of catalysts with efficient catalytic activity, high stability and environmentally friendly is the key for the successful employment of HCO. Through an exhausted bibliographic review, it is provided an overview of the advancements in HCO using MnO_2/MnO_2-based materials, focusing on their preparation, structural characteristics, and catalytic performance. Finally, it is summarized the possible mechanisms of catalytic ozonation efficiency by MnO_2/MnO_2-based catalysts.

The review is redrafted from the paper:

Jing Liu, Xiangjuan Yuan, Huiyu Dong, Carmen Sans, *Progress in MnO_2/MnO_2-Based Materials Catalytic Ozonation Process for Water and Wastewater Treatment*. Submitted to Journal of Environmental Management (2025).

Chapter 4: Effect of complexation between manganese dioxides and organic acids on enhancing catalytic ozonation efficiency

During the experimental work of this thesis was found that the adding sequence of the catalyst and O_3 stock solution would significantly influence the catalytic ozonation efficiency. When adding catalysts (α-MnO_2, β-MnO_2, and δ-MnO_2) into the reaction first, the α-MnO_2/OA/O_3 β-MnO_2/OA/O_3, and δ-MnO_2/OA/O_3 system could achieve the enhanced co-degradation of ATZ and OA, which might due the presence of MnO_2-OA complexes. Furthermore, aside from OA, the presence of different acids in the catalytic ozonation system can result in varying pollutant degradation efficiencies.

The mentioned results are included in the paper:

Jing Liu, Xiangjuan Yuan, Carmen Sans, Effect of complexation between manganese dioxides and organic acids on enhancing catalytic ozonation efficiency. (Under preparation).

Chapter 5: Insights into the role of β-MnO_2 and oxalic acid complex expediting ozonation: Structural properties and mechanism

In this study, a β-MnO_2-oxalic acid (β-MnO_2-OA) complex was constructed and used in HCO for pCBA degradation (β-MnO_2/OA/O_3). The 90.4% of pCBA and 65.2% of OA degradation were achieved at pH 4.0 within 10 mins by the incorporation of OA (10 mg L^{-1}) and β-MnO_2 (50 mg L^{-1}). Systematic characterization techniques (XPS, H_2-TPR, and *etc.*) confirmed the enhanced electron transfer ability and redox property of β-MnO_2-OA complex. More oxygen vacancies and reactive oxygen species (ROS) were generated through facilitating oxygen species migration, thus promoting the removal efficiency of pollutants.

The mentioned results can be found in the publication:

Jing Liu, Xiangjuan Yuan, Carmen Sans, Effect of complexation between manganese dioxides and organic acids on enhancing catalytic ozonation efficiency. Separation and Purification Technology 341 (2024) 126904. https://doi.org/10.1016/j.seppur.2024.126904.

Chapter 6: Enhanced effects of oxalic acid complexation with various MnO_2 crystals on catalytic ozonation: Structural properties, ROS contribution and Mechanism

This work found that the various crystal phases of MnO_2 material affect the catalytic ozonation activity of catalysts but had no effect on the formation of MnO_2-OA complexes, which relied on the presence of Mn^{3+}. At catalyst-to-OA molar ratio of 1:0.8, the ATZ degradation in α-MnO_2/OA/O_3, β-MnO_2/OA/O_3, and δ-MnO_2/OA/O_3 processes reached 95.09%, 93.43%, and 96.71%, respectively. Due to the differences in the structural properties of various MnO_2-OA complexes, the mechanisms of catalytic ozonation were different.

The mentioned results were presented in the publication:

Jing Liu, Xiangjuan Yuan, Carmen Sans, Exploring Phase Effects and ROS Contributions in Catalytic Ozonation of Polymorphic MnO_2-Oxalic Acid Complexes, Submitted to Separation and Purification Technology (2025).

CHAPTER 3

Materials and Methods

3.1 Chemicals

All chemicals including 4-Chlorobenzoic acid (pCBA), atrazine (ATZ), Acetaminophen (ACMP), ibuprofen (IBU), potassium permanganate ($KMnO_4$), pyruvic acid, ammonium persulfate $(NH_4)_2S_2O_8$), citric acid (CA), tert-butanol (TBA), *p*-benzoquinone (BQ), Sodium pyrophosphate (PP), metronidazole (MDE), 2,4-dichlorophenoxyacetic acid (2,4-D), terephthalic acid (TA) were analytical grade, provided by Merck. Manganese sulphate 1-hydrate ($MnSO_4$), oxalic acid 2-hydrate ($C_2H_2O_4$), acetic acid (AA), formic acid (FA), sodium thiosulfate ($Na_2S_2O_3$), phosphoric acid (H_3PO_4), acetonitrile (ACN), sodium hydroxide (NaOH), hydrochloric acid (HCl), and sodium azide (NaN_3) were pharma grade supplied by Panreac. 2,2,6,6-Tetramethyl-1-piperidinyloxy (TEMPO, purity > 97%) and 5,5-dimethyl-1-pyrolin-N-oxide (DMPO, purity > 97%) were obtained from Aladdin, China. All aqueous solutions were prepared by Milli-Q system (Merck Millipore, Germany).

3.2 Preparation of MnO_2 catalysts

A series of MnO_2 materials with different crystal phases were synthesized through a hydrothermal-calcination method, using various precursor solutions, hydrothermal temperatures, and duration.

For obtaining α-MnO_2, 1.25 g $KMnO_4$ and 0.53 g $MnSO_4$ were dissolved in 80 mL Milli-Q water under stirring for 2h. Then, the dark brown mixture was transferred to two 100 mL Teflon-lined stainless-steel autoclaves and heated at 160ºC for around 15-16 h. After cooling to room temperature, the black slurry was centrifuged, washed by Milli-Q water and dried at 100ºC for 24 h. Finally, the resultant solid was saved into a crucible and put in the muffle furnace for calcination at 360ºC for 2 h with heating rate 180ºC h^{-1}.

For the synthesis of β-MnO_2, 3.38 g of $MnSO_4$ and 4.56 g of $(NH_4)_2S_2O_4$ were dissolved in 80 mL of Milli-Q water with continuous stirring for 2h. The resulting dark brown solution was then distributed into two 100 mL Teflon-lined stainless-steel autoclaves and subjected to hydrothermal treatment at 90ºC for approximately 24 h. Once cooled to room temperature, the black suspension was separated by centrifugation, thoroughly rinsed with Milli-Q water, and dried at 100ºC for 24 hours. The obtained solid was subsequently placed in a crucible and calcined in a muffle furnace at 360ºC for 2 hours with a heating rate of 180ºC per hour.

To prepare δ-MnO_2, 1.50 g of $KMnO_4$ and 0.28 g of $MnSO_4$ were dissolved in 80 mL of Milli-Q water under continuous stirring for 2 hours. The dark brown solution was then transferred into two 100 mL Teflon-lined stainless-steel autoclaves and heated at 160ºC for 15–16 hours. After the system was cooled to room temperature, the resulting black slurry was collected via centrifugation, washed with Milli-Q water, and dried at 100ºC for 24 hours. Finally, the dried solid was placed in a crucible and calcined in a muffle furnace at 360ºC for 2 hours with a heating rate of 180ºC per hour.

3.3 Characterizations

1) XRD analysis: The catalysts were ground into a fine powder using an agate mortar and pestle to ensure uniform particle size. A small amount of the powdered sample was then evenly spread onto the sample holder, ensuring a flat and smooth surface. To minimize any preferred orientation effects, gentle tapping and leveling were performed. The sample holder was subsequently placed into the X-ray diffractometer for analysis.

The Bruker D8 powder X-ray Diffractometer (PANalytical, Netherlands) with Cu Ka radiation (λ=0.154178 nm) was employed to record the X-ray powder diffraction (XRD) patterns, using a radiation at 40 kV and 15 mA. Two theta from 10º to 80º were obtained at a scanning rate of 0.5º/min.

2) FT-IR analysis: A small amount of the sample (typically 1-2 mg) was thoroughly mixed with approximately 100 mg of dried KBr in an agate mortar to ensure uniform dispersion. The mixture was finely ground and then pressed into a transparent pellet using a hydraulic press under high pressure.

The KBr pellet containing the sample was placed in the FT-IR spectrometer for measurement. The Fourier transform infrared (FT-IR) spectra was collected by Thermo Scientific Nicolet iS5 spectrometer (Thermo Fisher, USA) with KBr film method at room temperature between 4000 and 400 cm^{-1}.

3) HRTEM analysis: The high-resolution transmission electron microscopy (HRTEM) images were obtained using a JEOL JEM-2100F microscope (FEI, USA). To prepare samples for TEM analysis, a small amount of the material was dispersed in a suitable solvent, such as ethanol or deionized water, using ultrasonication to create a well-dispersed suspension. A drop of the suspension was carefully applied to a carbon-coated copper grid using a micropipette. After allowing the solvent to evaporate naturally or under gentle heating, the dried grid was loaded into the TEM for observation and analysis.

4) SEM analysis: A small amount of the sample was evenly spread onto a conductive adhesive tape or carbon tape attached to a sample holder. Non-conductive samples were coated with a thin layer of conductive material, such as gold or platinum, using a sputter coater to enhance conductivity and reduce charging effects. The prepared sample was then loaded into the SEM chamber for imaging and analysis.

The Hitachi S-4800 scanning electron microscope (SEM) instrument (Hitachi, Japan) was used to observe the morphology of catalysts.

5) XPS analysis: The sample was carefully ground into a fine powder, if necessary, to ensure uniformity. A small amount of the sample was then pressed onto a double-sided conductive adhesive tape or mounted on a sample holder suitable for XPS analysis. For powders, care was taken to achieve a smooth and evenly distributed surface. The prepared sample was loaded into the XPS instrument under vacuum conditions for measurement. Non-conductive samples were neutralized using a charge compensation system during analysis to avoid charging effects.

The VG Multilab2000 spectrometer (Thermo Fisher, USA) were conducted to obtain X-ray photoelectron spectra (XPS), being conducted on a Kratos AXIS Ultra DLD high performance, electron spectrometer with non-monochromatized Al Kα excitation source (hv=1486.6 eV). Binding energies were calibrated by using the contaminant carbon (C1s= 284.8 eV).

6) H_2-TPR analysis: A known amount of the catalyst (typically 50–100 mg) was loaded into a quartz U-tube reactor. The sample was pretreated by heating in an inert gas, such as argon or nitrogen, to remove any adsorbed impurities. After cooling to room temperature under the same inert atmosphere, a gas mixture of H_2 (typically 5–10% in argon) was introduced at a controlled flow rate (50 mL/min). The temperature of the reactor was then gradually increased (from 100 to 700°C) at a specific heating rate (e.g., 10°C/min) while monitoring the H_2 consumption using a thermal conductivity detector (TCD). Data were recorded to analyze the reduction behavior of the catalyst.

Hydrogen temperature programmed reduction (H_2-TPR) was carried out in a U-shaped quartz reactor using an AutoChem II2920 chemisorption analyzer (Micromeritics Instrument Corp.) equipped with a TCD detector to measure catalyst reducibility.

7) *O_2-TPD analysis:* For oxygen temperature programmed desorption analysis (O_2-TPD), the catalyst sample (typically 50–100 mg) of 40-60 mesh was placed into a quartz U-tube reactor. Before starting the desorption experiment, the sample was pretreated in a flow of inert gas for 0.5 h, such as helium or nitrogen, at an elevated temperature (typically 300–400°C) to remove any adsorbed species. After the pretreatment, the sample was cooled to room temperature under a mixture of 10% O_2/He (60 mL/min) at 25°C for 1 h. The

reactor was then purged with pure oxygen to allow oxygen adsorption onto the catalyst surface. Following oxygen adsorption, the temperature was increased at a controlled rate (e.g., 10°C/min) while monitoring the desorbed oxygen using a mass spectrometer or a thermal conductivity detector (TCD). This method helps to investigate the surface oxygen species and their desorption characteristics.

8) Py-IR analysis: Pyridine adsorbed IR spectroscopy (Py-IR) was conducted using an FT-IR (Tensor 27, Bruker, Germany) equipped with a custom-made IR cell that was connected by a vacuum adsorption apparatus.

For Py-IR analysis, the catalyst sample (typically 10–20 mg) was first outgassed under vacuum at an elevated temperature (usually 200–300°C) for several hours to remove any adsorbed moisture or other volatile species. After cooling to room temperature in a vacuum (10^{-3} Pa), the sample was exposed to a pyridine vapor (or pyridine gas) by introducing a small amount of pyridine into the sample chamber. The sample was allowed to adsorb pyridine for a specific period (usually 30 minutes to 1 hour) until the adsorption approached saturation. Once the pyridine had adsorbed, excess pyridine was removed by purging the sample with an inert gas, such as nitrogen or helium. The sample was then analyzed using infrared spectroscopy to examine the pyridine adsorption bands, which provide information about the acidic properties of the catalyst surface.

9) BET analysis: around 0.1-0.2 g of catalyst was first degassed to remove adsorbed moisture and other impurities. The sample was placed in a sample tube or chamber and heated under a vacuum or inert gas flow (such as nitrogen) at elevated temperatures (usually 100–200°C) for several hours, depending on the sample type. After degassing, the sample was cooled to room temperature in a vacuum or inert atmosphere. Once prepared, the sample was exposed to a known amount of nitrogen gas (or another adsorbate) at liquid nitrogen temperature (around -196°C) to measure the adsorption isotherm. The nitrogen adsorption was used to determine the specific surface area of the sample, and the BET method was employed to analyze the surface area based on the adsorption of gas molecules on the material's surface.

The Micromeritics ASAP 2010 porosimeter was used to determine the Brunauer–Emmett–Teller (BET) surface area. The specific surface area, pore volume, and pore size distributions of the catalysts were calculated according to the Barrett-Joyner-Halenda (BJH) method.

10) ESR analysis: Electron spin resonance (ESR) spectra were recorded at room temperature using a Bruker ESR A300 spectrometer (Bruker, Germany).

For ESR analysis, the sample was typically prepared as a solid, liquid, or powder, depending on the nature of the material. For solid or powder samples, the sample was first ground into a fine powder, if necessary. The prepared sample is then placed in an ESR tube (usually a quartz or glass tube). If the sample was in liquid form, it was directly injected into the ESR tube. Once the sample was prepared, it was loaded into the ESR instrument, where it was subjected to a magnetic field, and the absorption of microwave radiation is measured. This technique was used to study the electronic structure, concentration, and dynamics of paramagnetic species, such as free radicals or metal ions.

3.4 Experimental procedures

3.4.1 Adsorption experiments

For adsorption experiments, a certain concentration of pollutants and MnO_2 were mixed in 100 mL milli-Q water. At specific time intervals, 1.5 mL samples were obtained. After filtered by 0.45 μm filter, the samples were further analyzed using High Performance Liquid Chromatography (HPLC).

3.4.2 Catalytic activity experiments

1) Semi-continuous system

The experimental setup for the emi-continuous ozonation experiments was illustrated in Fig. 3.1. Oxygen bottle was used to convert O_2 (P= 2 bar) to O_3 using a laboratory ozonizer (Model 301.19, Sander, Germany), maintained at 5 °C by a thermostatic bath. The ozone inlet concentration to the reactor was fixed at 80 mg/NL with a flow rate of 0.7 L min^{-1}. Simultaneous monitoring of the inlet and outlet gas-phase ozone concentrations was performed using two ozone analyzers (BMT 963vent and 964 Messtechnik, Germany). The experiments were conducted in a jacketed glass slurry-type reactor with a continuous O_3 stream introduce into reactor of 500 mL volume. The OA degradation was used to evaluate the catalytic ozonation performances of catalysts. The initial OA concentration was set at 20 mg L^{-1} to facilitate monitoring of their evolution and mineralization through the available analytical techniques. The reactor was maintained at around 20°C, controlled by a thermostatic bath, and stirred magnetically at 500 rpm. A desirable amount of catalyst was added into the reactor to initiate the catalytic ozonation reaction. During the experiments, 1.5 mL samples were taken at specific time intervals and immediately quenched with an excess of 0.01 M $Na_2S_2O_3$ to remove residual O_3. After filtered by 0.45 μm filter, the samples were further determined through HPLC.

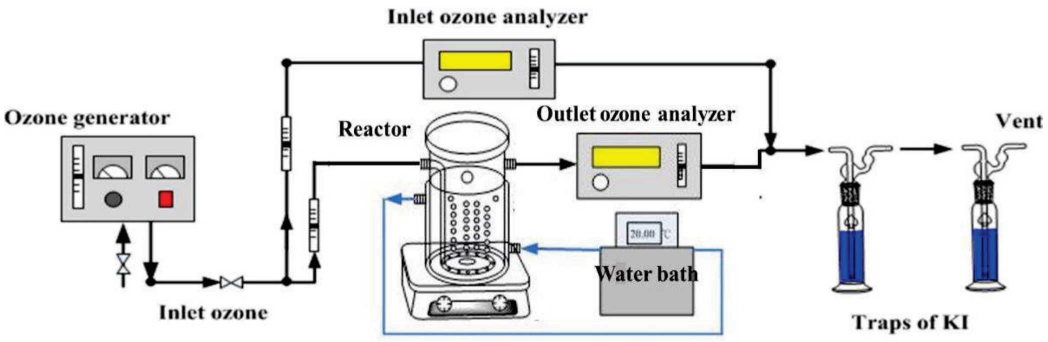

Fig. 3.1 The schematic diagram of semi-continuous catalytic ozonation experiments

2) Batch experiment systems

For the batch mode (Cat/O_3), the gaseous (0.7 L min^{-1}, about 120 mg L^{-1}) generated through a laboratory ozonizer (Model 301.19, Sander, Germany), was bubbled into 250 mL of Milli-Q water kept in an ice bath for 40 minutes to gain the O_3 stock solution with dissolved O_3 concentration around 45 mg L^{-1}. The concentration of dissolved O_3 was measured at 260 nm (ε_{O3} = 3200 M^{-1} cm^{-1}) by a DR6000 UV-Vis spectrophotometer (Hach, USA). Typically, a certain dosage of catalyst was added into the OA solution under stirring (400 rpm). Then, a certain amount of O_3 stock solution was dosed into the reactor to initiate the catalytic ozonation reaction with initial reaction concentration of O_3 in the range of 1 mg L^{-1} to 30 mg L^{-1}.

For Cat/OA/O_3 processes, OA solution and pollutants solution (e.g. ATZ) were mixed in 100 mL Milli-Q water with continuous stirring (400 rpm) at room temperature. Then, a certain dosage of catalyst was added into the mixture solution, and subsequently, the corresponding O_3 stock solution was added to initiate the catalytic ozonation reaction with the initial reaction O_3 concentration of O_3 about 1 mg L^{-1} to 30 mg L^{-1}. During the experiments, 1.5 mL samples were taken at specific time intervals and immediately quenched with an excess of 0.01 M $Na_2S_2O_3$ to remove residual O_3. After filtered by 0.45 μm filter, the samples were further determined through HPLC (Fig.3.2).

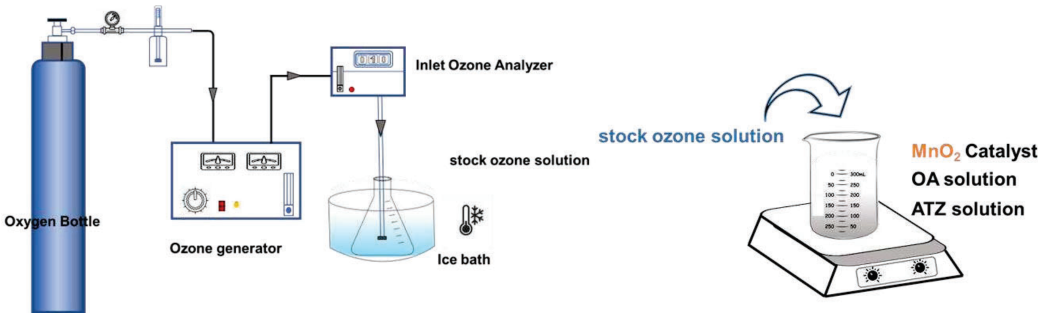

Fig. 3.2 The schematic diagram of catalytic ozonation experiments in batch mode.

3.4.3 Probe experiments

In HCO processes, the O_3, $^{\bullet}OH$, $O_2^{\bullet-}$, and $^1O_2$ are generally considered to play important roles in contaminant degradation. In the study, TA, 2,4-D, and MDE as $^{\bullet}OH$, $O_2^{\bullet-}$, and $^1O_2$ probes, respectively, were added into the same catalytic ozonation system at low concentration (0.1 mg L^{-1}) to identify and quantify ROS. Moreover, the adsorption of the probes and ATZ on the surface of catalysts can be negligible. Therefore, the degradation of ATZ, TA, 2,4-D, and MDE in HCO system can be illustrated as Eqs. (3.1-3.4).

$$ln\left(\frac{[ATZ]_0}{[ATZ]_t}\right) = k_{^{\cdot}OH,ATZ}\int[^{\cdot}OH]\,dt + k_{O_2^{\cdot-},ATZ}\int[O_2^{\cdot-}]dt + k_{^1O_2,ATZ}\int[^1O_2]dt + k_{O_3,ATZ}\int[O_3]\,dt \tag{3.1}$$

$$ln\left(\frac{[TA]_0}{[TA]_t}\right) = k_{^{\cdot}OH,TA}\int[^{\cdot}OH]\,dt + k_{O_2^{\cdot-},TA}\int[O_2^{\cdot-}]dt + k_{^1O_2,TA}\int[^1O_2]dt + k_{O_3,TA}\int[O_3]\,dt \tag{3.2}$$

$$ln\left(\frac{[MDE]_0}{[MDE]_t}\right) = k_{^{\cdot}OH,MDE}\int[^{\cdot}OH]\,dt + k_{O_2^{\cdot-},MDE}\int[O_2^{\cdot-}]dt + k_{^1O_2,MDE}\int[^1O_2]dt + k_{O_3,MDE}\int[O_3]\,dt \tag{3.3}$$

$$ln\left(\frac{[2,4\text{-}D]_0}{[2,4\text{-}D]_t}\right) = k_{^{\cdot}OH,2,4\text{-}D}\int[^{\cdot}OH]\,dt + k_{O_2^{\cdot-},2,4\text{-}D}\int[O_2^{\cdot-}]dt + k_{^1O_2,2,4\text{-}D}\int[^1O_2]dt + k_{O_3,2,4\text{-}D}\int[O_3]\,dt \tag{3.4}$$

$$O_{3,exp} = \int[O_3]dt \tag{3.5}$$

$k_{O_3,compound}$, $k_{^{\cdot}OH,compound}$, $k_{O_2^{\cdot-},compound}$, and $k_{^1O_2,compound}$ are the second-order rate constant for the reaction of probe compounds and ATZ with O_3, $^{\bullet}OH$, $O_2^{\bullet-}$, and $^1O_2$, respectively, which are listed in Table 3.1. O_3 exposure ($\int[O_3]dt$) was determined from the time integrated O_3 concentration during the treatment time Eq. (3.5). The exposures of $^{\bullet}OH$, $O_2^{\bullet-}$, and $^1O_2$ were calculated through Eqs.(3.2-3.4), which were described as $\int[{}^{\cdot}OH]\,dt$, $\int[O_2^{\cdot-}]dt$, and $\int[{}^1O_2]dt$, respectively, based on the observed abatement efficiency of TA, 2,4-D, and MDE in the same HCO system.

Table 3.1 Second-order rate constants for the reaction of test micropollutants with O_3, $^{\bullet}OH$, $O_2^{\bullet-}$, and $^1O_2$.

Compounds	k_{O_3} ($M^{-1}\cdot s^{-1}$)	$k_{\cdot OH}$ ($M^{-1}\cdot s^{-1}$)	$k_{O_2^{\cdot-}}$ ($M^{-1}\cdot s^{-1}$)	$k_{^1O_2}$ ($M^{-1}\cdot s^{-1}$)
TA	0.04	3.3×10^9	1.1×10^4	1.2×10^7
2,4-D	29.1	5.1×10^9	8.3×10^5	No·Reaction
MDE	<1	6×10^9	No·Reaction	1.5×10^8
ATZ	2.3	2.4×10^9	4.1×10^5	$<4\times10^4$

3.5 Analytic methods

1) *Dissolved O_3 concentration:* The dissolved O_3 concentration was measured by indigo method (Bader and Hoign´e, 1981). A quartz cell with an optical path length of 1 cm was sealed immediately after syringe injection of samples and indigo solution and measured through UV-Vis spectrophotometer. Use pure water as the blank control. Mix a pure water sample with the indigo solution and measure its absorbance at a wavelength of 600 nm. After catalytic ozonation reaction was initiated, the reaction sample was taken at regular time intervals. Immediately mix sample with the indigo solution, and measure the absorbance using a UV-Vis spectrophotometer. The dissolved O_3 concentration in the solution was calculated by comparing the difference valne in absorbance before and after the reaction, Additionally, the stock ozone solution decreased at a rate of 0.07% per minute during the reaction time, which can be regarded as no decrease over the timescale of the experiment.

2) *Pollutants concentration analysis:* The concentration of dissolved Metal ion was monitored by Perkin Elmer Optima 8300 ICP (American). The concentration of pollutants was analyzed by an Infinity 1260 HPLC from Agilent Technologies (USA) equipped with a Mediterranea Sea18 column (250 mm × 4.6 mm with a particle size of 5 μm) from Teknokroma (Spain). Acetonitrile and phosphoric acid were used as the mobile phases. The specific measure methods of different compounds were displayed in the Table 3.2.

Table 3.2 The details of HPLC method for various compound.

Compound	Mobile·Phases·(v/v)		Flow·Rate	Wavelength
	H_3PO_4(pH=3)	ACN	mL·min^{-1}	nm
OA	80	20	0.85	210
pCBA	40	60	1	234
ATZ	55	45	1	220
IBU	25	75	1	220
ACMP	60	40	1	250

3) *Probe compounds analysis:* The probe compounds were separated by Vanquish HPLC-MS 137, equipping with Halo C18 (2.1×150 mm, 2.7μm) column, 0.1% formic acid (A) and acetonitrile (B) were used as the mobile phases and the samples were analyzed at a constant flow rate of 0.5 mL min^{-1}. The column temperature is controlled at 40°C. The mobile phase gradient elution procedure and the detailed detective instrument information is demonstrated in Table 3.3.

Table 3.3 The details of HPLC-MS method for probe compounds.

Mobile phase gradient elution procedure		
Time (min)	Mobile phase A%	Mobile phase B%
0.0	95	5
10	65	35
11	35	65
16	0	100
18	0	100
18.5	95	5
22	95	5

The materials, along with the specific methods employed for each experiment, were comprehensively described and elaborated upon in the corresponding results chapter, providing a clear and detailed account of the experimental procedures.

CHAPTER 4

Effect of complexation between manganese dioxides and organic acids on enhancing catalytic ozonation efficiency

The result could be found in the paper:

Jing Liu, Xiangjuan Yuan, Carmen Sans, Effect of complexation between manganese dioxides and organic acids on enhancing catalytic ozonation efficiency. (Under preparation).

4.1 Introduction

Manganese dioxides (MnO_2) as a usual MnOx material show a highly flexible structure. Based on the diverse rectangular configuration of basic unit ([MnO_6] octahedron), MnO_2 exhibits different crystal phases such as α-, β-, δ-, γ-, λ-, and ε-MnO_2 [1, 2]. α-MnO_2 possesses a [2 × 2] tunnel structure consisting of double chains of [MnO_6] octahedra, where each square has a side length of 4.6 Å [3]. β-MnO_2 as the mineral pyrolusite features a [1 × 1] tunnel or channel with a width of 2.3 Å x 2.3 Å [4]. However, δ-MnO_2 presents a typical lamellar structure with a large interlayer spacing (~7 Å) [5]. Ma et al [6] reported that different crystal MnO_2 material followed an activity order of δ-MnO_2>α-MnO_2>γ-MnO_2>β-MnO_2 in the degradation of sulfachloropyridazine. Hydroxyl radical($^{\bullet}OH$) and singlet oxygen ($^1O_2$) play an important role in the reaction. Zhang et al [7] found β-MnO_2 synthesized by NO_3^- precursors was more active than β-MnO_2 synthesized by SO_4^{2-} and Cl^- in removing COD of bio-treated coking wastewater. The higher catalytic ozonation performance was attributed to more adsorbed oxygen and crystal defects on the surface of disordered β-MnO_2-NO_3^-. Nawaz et al. [8] revealed that superoxide radicals ($O_2^{\bullet-}$), rather than $^{\bullet}OH$, were mainly responsible for the catalytic ozonation degradation of 4-Nitrophenol (4-NP) by α-MnO_2. It could be concluded that the application of different crystal MnO_2 catalysts in HCO process for pollutant removal displays various catalytic activity and the mechanisms are complex and diverse.

Therefore, this study aims to 1) improve the synthesis method of composites to obtain α-MnO_2, β-MnO_2, and δ-MnO_2 materials for pollutant removal to evaluate catalytic performance, 2) optimize experimental conditions to enhance O_3 utilization efficiency and catalyst activity. Oxalic acid (OA) is a common final oxidation product of organic pollutants that has very low reactivity with O_3 ($k_{O3,OA} \leq 0.04\ M^{-1}\ S^{-1}$) [9]. Thus, OA was selected as target pollutant for evaluating the activity of MnO_2 in catalytic ozonation system Moreover, some researchers found that OA as an organic acid ligand can directly form complexes with MnOx to promote the degradation efficiency of organic compounds [10-12]. Consequently, the effect of organic acids including OA as ligands on improving the MnO_2 catalytic ozonation efficiency is investigated.

4.2 Experimental methods

4.2.1 Reagents

Reagents used in this study include atrazine (ATZ), pyruvic acid, citric acid, potassium permanganate ($KMnO_4$), and ammonium persulfate ($NH_4)_2S_2O_8$), manganese sulphate 1-hydrate ($MnSO_4$), NaOH, oxalic acid 2-hydrate ($C_2H_2O_4$), acetic acid, formic acid, sodium thiosulfate ($Na_2S_2O_3$), hydrochloric acid (HCl), phosphoric acid (H_3PO_4) and acetonitrile. All aqueous solutions were prepared by Milli-Q system (Merck Millipore, Germany).

4.2.2 Catalysts fabrication

The α-MnO_2, β-MnO_2, and δ-MnO_2 were fabricated by a modified hydrothermal-calcination approach. Typically, for α- MnO_2, 1.25 g $KMnO_4$ and 0.53 g $MnSO_4$ were dissolved in 80 mL Milli-Q water under stirring for 2h. Then, the dark brown mixture was transferred to two 100 mL Teflon-lined stainless-steel autoclaves and heated at 160ºC for around 15-16 h. Finally, the resultant solid was saved into a crucible and put in the muffle furnace for calcination at 360ºC for 2 h with heating rate 180ºC h^{-1}. β-MnO_2 and δ-MnO_2 were obtained in similar procedure, more details were displayed in CHAPTER 3 Materials and Methods.

4.2.3 Catalytic ozonation experiments

In this study, both semi-continuous and batch systems were used to estimate the catalytic ozonation performances of α-MnO_2, β-MnO_2, and δ-MnO_2 catalysts. Initially, the semi-continuous system was employed to assess the potential activity of the catalyst under different synthesis conditions, obtaining a broad range of experimental parameters. Subsequently, batch experiments were conducted to further evaluate the catalytic ozonation performance of catalysts by controlling individual variables, such as the concentration of dissolved O_3 (1 mg L^{-1} to 30 mg L^{-1}). During the experiments, 1.5 mL samples were taken at specific time intervals and immediately quenched with an excess of 0.01 M $Na_2S_2O_3$ to remove residual O_3. After filtered by 0.45 µm filter, the samples were further determined through High Performance Liquid Chromatography (HPLC).

4.2.4 Analysis method

The concentration of pollutants was analyzed by an Infinity 1260 HPLC from Agilent Technologies (USA) equipped with a Mediterranea Sea18 column (250 mm × 4.6 mm with a particle size of 5 μm) from Teknokroma (Spain). Acetonitrile and phosphoric acid were used as the mobile phases. ATZ samples were measured at a wavelength of 220 nm with a constant flow rate of 1 mL min^{-1}. OA samples were tested at a wavelength of 210 nm with a constant flow rate of 0.85 mL min^{-1}.

4.3 Results and discussion

4.3.1 Optimization of catalysts preparation method

The α-MnO_2, β-MnO_2, and δ-MnO_2 were synthesized through the hydrothermal method, and OA removal efficiency was used to evaluate the catalytic ozonation performances of various catalysts. Considering the effect of synthesis procedure on catalytic activity of catalysts, the OA degradation of different catalysts with hydrothermal-calcination was compared and the results are shown in Fig.4.1. The sole ozonation achieved 9.52% of OA removal, while it was improved in the presence of α-MnO_2(66.16%), β-MnO_2(70.33%), and δ-MnO_2(15.08%) in 30 mins Fig.4.1(a). As displayed in Fig.4.1(b), the catalytic ozonation performances of α-MnO_2, β-MnO_2, and δ-MnO_2 after calcination were significantly enhanced. The corresponding OA degradation was 98.73%, 99.58%, and 39.82%, respectively, with reaction rates over 30 min increasing more than threefold to 0.31, 0.18, and 0.03 min^{-1}, respectively. Moreover, less than 5% of OA adsorption in 30 min was detected by as-prepared catalysts (Fig.4.2), which indicated that the adsorption effect of catalysts could be neglected. Therefore, a modified hydrothermal-calcination approach was ultimately used to synthesize the catalysts for subsequent studies.

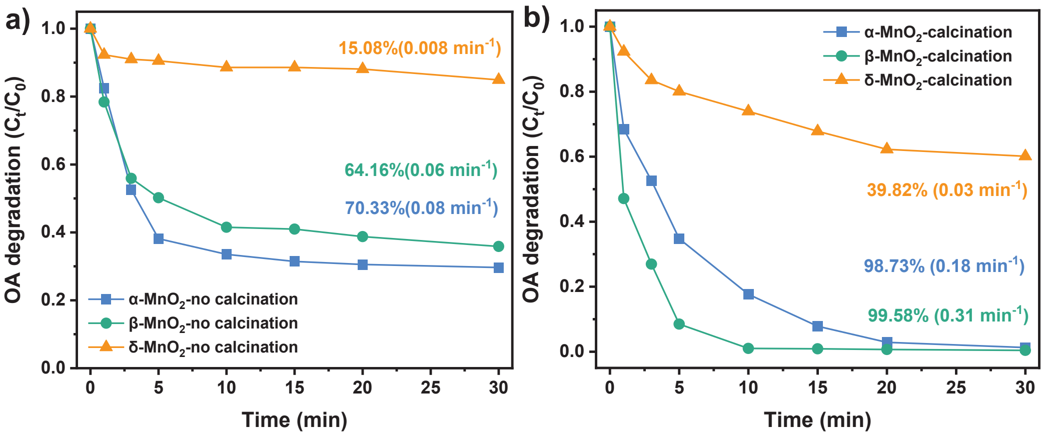

Fig. 4.1 The catalytic ozonation performances of catalysts without calcination a) and with calcination b). Experimental conditions: [OA]=20 mg L^{-1}, [Cat.]=300 mg L^{-1}, pH_0=7.0

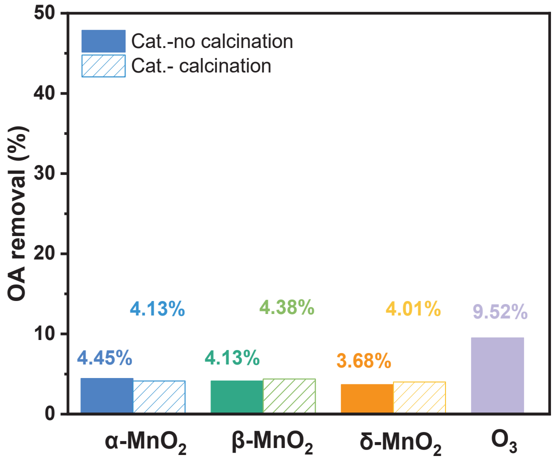

Fig. 4.2 The OA removal by catalysts and O_3 alone. Experimental conditions: [OA]=20 mg L^{-1}, [Cat.]=300 mg L^{-1}, pH_0=7.0

4.3.2 Optimization of reaction conditions

To further determine the reaction conditions such as dissolved O_3 concentration and catalyst dosage, the catalytic ozonation experiments were conducted in batch mode. As illustrated in Fig.4.3(a), when the initial O_3 concentration increased from 1 to 30 mg L^{-1}, the OA degradation efficiency rose from 1.64% to 8.65% in ozonation alone. The presence of α-MnO_2, β-MnO_2, and δ-MnO_2 catalysts (10 mg L^{-1}) could enhance the OA removal to 53.65%, 53.47%, and 49.77%, respectively at 1 mg L^{-1} of O_3. However, the continuous increase of O_3 concentration did not induce the growth of OA degradation in catalytic ozonation systems, which was related to the limited active sites provided by catalyst. Therefore, when the dosage of catalyst was raised to 50 mg L^{-1} (Fig.4.3(b)), the removal of OA in α-MnO_2/O_3, β-MnO_2/O_3, and δ-MnO_2/O_3

processes were augmented gradually with increasing O_3 concentration. Amongst, β-MnO_2 exhibited the best catalytic activity, more than 90% of OA degradation was achieved in 10 mins at an O_3 concentration of 5 mg L^{-1}. In conclusion, the dosage of catalyst and the concentration of O_3 were important factors in the catalytic ozonation system.

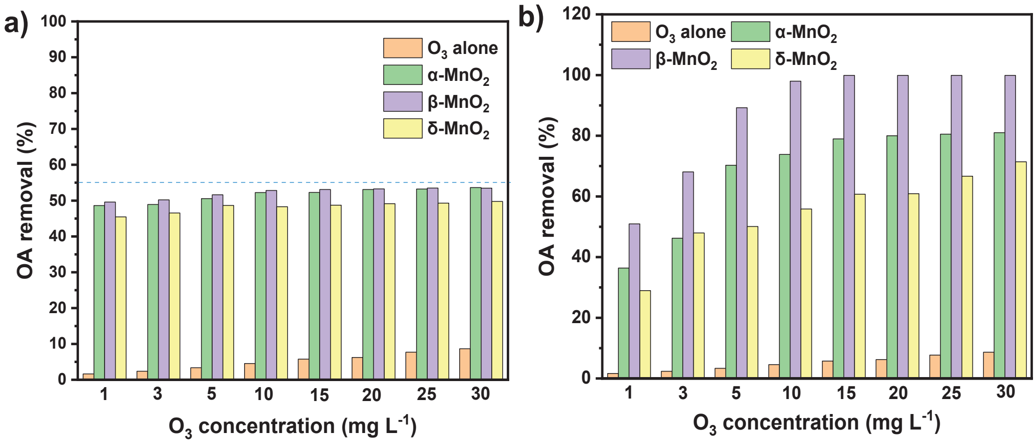

Fig. 4.3 The OA removal of various catalytic ozonation systems with 10 mg L^{-1} a) and 50 mg L^{-1} b) of catalysts. Experimental conditions: [OA]=10 mg L^{-1}, [O_3]=1-30 mg L^{-1}, pH_0=7.0.

4.3.3 The presence of MnO_2-OA complex

In catalytic ozonation experiments, it was found that the adding sequence of catalyst and O_3 solution had significant influence on OA degradation. As demonstrated in Fig.4.4, only 20.53% of OA was eliminated when O_3 stock solution was first added into OA solution. However, if the catalyst was added first, followed by the O_3 stock solution, the catalytic ozonation system could achieve 77.92% of OA removal. Wang et al. [13] reported that the δ-MnO_2/OA reaction system could efficiently degrade (67.83%) methyl parathion (MP) by the presence of Mn(III)-OA complex, which was primary active substance produced in the reaction system. They inferred that δ-MnO_2 was first reduced by OA to generate Mn(III), and the excess OA combined with Mn(III) to form Mn(III)-OA complex. Then, Mn(III)-OA complex combined with MP to form active complexes, thus, MP and its hydrolysis products were reduced by electron transfer [14]. Therefore, in our study, we suspected that adding the catalyst to the system first would lead to the formation of complex with a portion of OA. The complex reacted with O_3 to produce more reactive species, which further enhanced the degradation of OA. In addition, the electron transfer during complex formation could play a crucial role in facilitating the O_3 chain reaction.

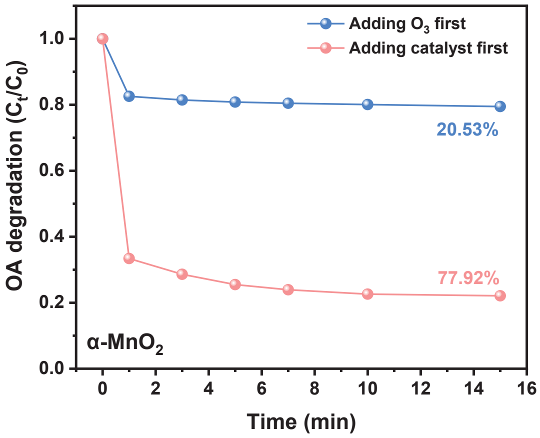

Fig.4.4 The effect of the adding sequence of α-MnO_2 and O_3 solution on catalytic ozone activity. Experimental conditions: [α-MnO_2]=50 mg L^{-1}, $[OA]_0$=10 mg L^{-1}, $[O_3]_0$=30 mg L^{-1}, pH_0=4.0 ± 0.2.

To investigate the effect of the mixing time between the catalyst (α-MnO_2) and OA on complex formation, O_3 stock solution was added 1min, 5 min, and 10 min after the catalyst was introduced to trigger the reaction. As explored in Fig.4.5, the contact time between α-MnO_2 and OA had no influence on the degradation of OA, with the degradation efficiency remaining around 78.22%. It was worth mentioning that the adsorption of OA by α-MnO_2 was less than 5% (Fig.4.2), which could be negligible. Therefore, it could be concluded that the mixing time between α-MnO_2 and OA had little effect on the generation of α-MnO_2-OA complex. During the experimental process, it was important to pay attention to the sequence of adding the catalyst and O_3 stock solution to facilitate complex formation, which would enhance the catalytic ozonation efficiency.

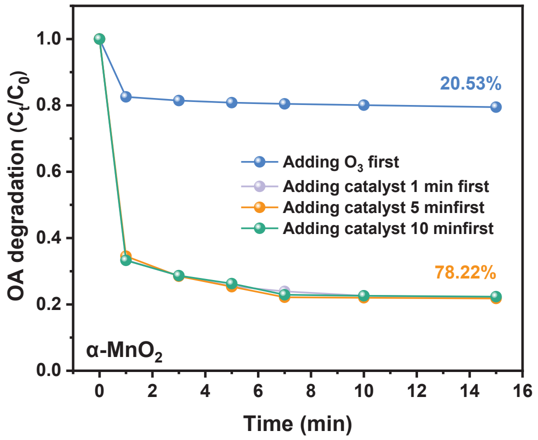

Fig.4.5 The effect of the mixing time of α-MnO_2 and OA solution on catalytic ozone activity. Experimental conditions: [α-MnO_2]=50 mg L^{-1}, $[OA]_0$=10 mg L^{-1}, $[O_3]_0$=30 mg L^{-1}, pH_0=4.0 ± 0.2.

Based on the experimental results mentioned above, the existence of OA might enhance the catalytic ozonation efficiency by forming the α-MnO_2-OA complex. Therefore, we further explore whether different structures of MnO_2 exhibited similar enhanced catalytic ozonation performance for pollutant removal in the presence of OA. Atrazine (ATZ) degradation was chosen to compare the activities of different systems, and the results were shown in Fig.4.6. The 43.6% of ATZ removal was achieved in O_3 alone within 3 min, while it was improved in α-MnO_2/OA/O_3 β-MnO_2/OA/O_3, and δ-MnO_2/OA/O_3 processes, which were 71.0%, 76.6%, and 67.1%, respectively. Meanwhile, as illustrated in Fig.4.6(b), the degradation of OA in α-MnO_2/OA/O_3 β-MnO_2/OA/O_3, and δ-MnO_2/OA/O_3 systems increased to 51.8%, 67.1%, and 34.3%, respectively, compared with the single ozonation (9.7%). The results indicated that the addition of OA might promote the formation of various MnO_2-OA complexes, which could facilitate the co-degradation of pollutants in HCO process.

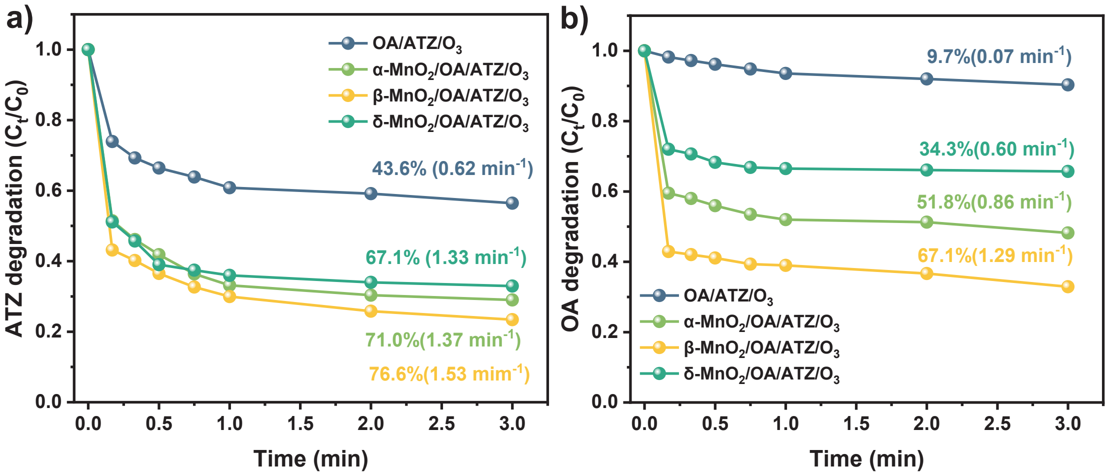

Fig.4.6 The ATZ degradation a) and OA degradation b) in different systems. Experimental conditions: [α-MnO_2]=[β-MnO_2]=[δ-MnO_2]=50 mg L^{-1}, $[OA]_0$=10 mg L^{-1}, $[O_3]_0$=5 mg L^{-1}, pH_0=4.3 ± 0.2.

4.3.4 Effect of other acids

It is unknown whether this process is effective for other organic acids or selective to special molecule structures. Therefore, formic acid (FA), acetic acid (AA), citric acid (CA), and pyruvic acid (PA) were introduced to the system in the same adding sequence as OA. As illustrated in Fig.4.7(a) and Fig.4.7 (c), the addition of FA and CA did not enhance catalytic ozonation performance for ATZ degradation. As for the presence of AA (Fig.4.7(b)), compared to ozonation alone (25.4%), the catalytic ozonation system (Cat/AA/ATZ/O_3) slightly increased ATZ removal by 5%-10%. Moreover, α-MnO_2 exhibited the highest activity, improving ATZ degradation by 25% in the existence of PA (Fig.4.7(d)). MnO_2 with different crystal structures presents varying catalytic activity, which are closely related to the differences in physicochemical properties. For instance, differences in crystalline structures can result in variations in specific surface area, which in turn affect the number of active sites and the adsorption ability of pollutants. Moreover, Zhang et al [15] used O_3/(CuO/CeO_2) system to degrade six distinct carboxylates (i.e., AA, CA, OA, PA, malonate and succinate). They revealed that the removal of carboxylates during the catalytic ozonation was selective, as those containing α-carbonyl and α-hydroxyl groups were more likely to form copper-carboxylate complexes and thus undergo further competitive degradation. Therefore, the complexation effects of different acids in the experiments may also be selective, which requires further investigation.

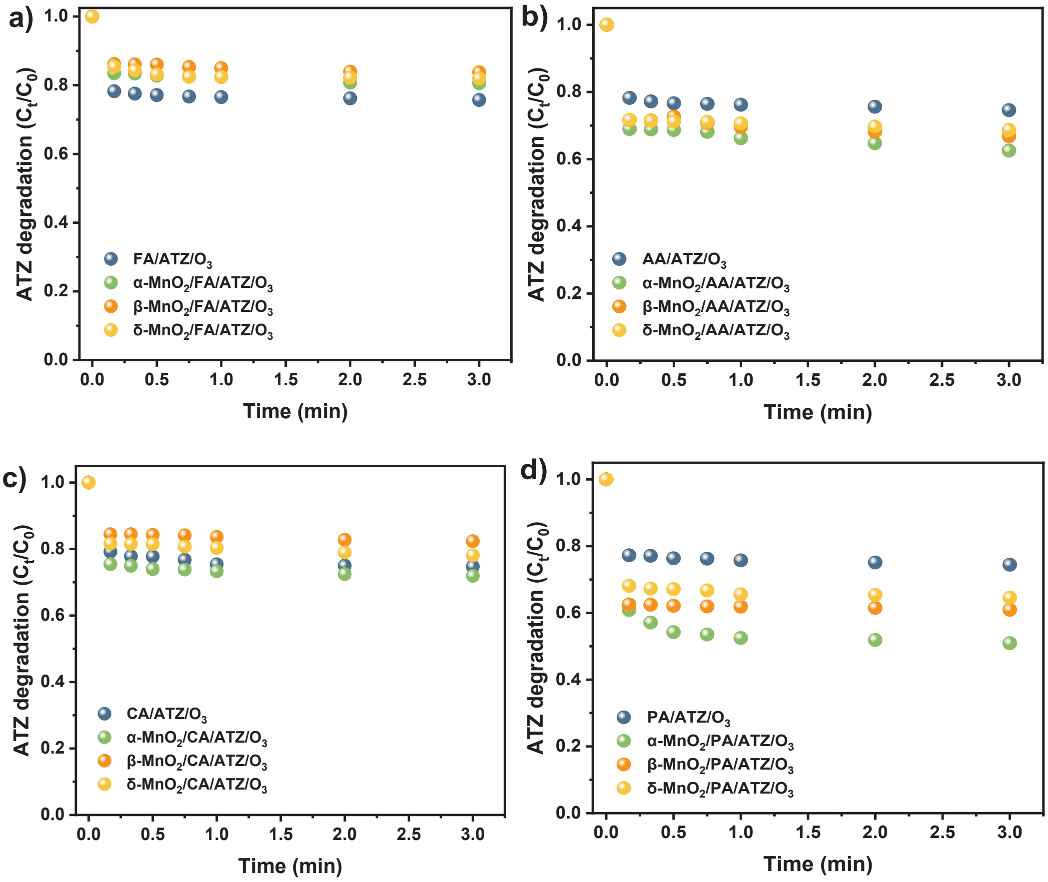

Fig.4.7 The effect of FA a), AA b), CA c), and PA d) on the ATZ degradation in different systems. Experimental conditions: [α-MnO_2]=[β-MnO_2]=[δ-MnO_2]=50 mg L^{-1}, $[Acid]_0$=10 mg L^{-1}, $[O_3]_0$=5 mg L^{-1}, pH_0=5.3 ± 0.2.

4.4 Conclusion

In this study, it was found that the adding sequence of the catalyst and O_3 stock solution would significantly influence the catalytic ozonation efficiency. When adding catalysts (α-MnO_2, β-MnO_2, and δ-MnO_2) into the reaction first, the α-MnO_2/OA/O_3 β-MnO_2/OA/O_3, and δ-MnO_2/OA/O_3 system could achieve the enhanced co-degradation of ATZ and OA, which might due the presence of MnO_2-OA complexes. Amongst, β-MnO_2 exhibited the highest activity with 76.6% of ATZ and 67.1% of OA removal. Moreover, considering whether this process is effective for other organic acids or selective to special molecule structures, other acids like FA, AA, CA, and PA were used in place of OA to conduct the experiment. The results suggested that the presence of PA might also promote catalytic ozonation efficiency through forming complex with MnO_2. However, the presence of complexes in the system needs to be further validated through experiments or characterization techniques. Additionally, the catalytic mechanisms of various crystal MnO_2-OA complexes still require in-depth investigation. Besides, the reasons for the different effects of various acids on MnO_2 catalytic ozonation system need to be further explored. These will be the key focus of subsequent research. Overall, this study provides new insights for the application of MnO_2 in catalytic ozonation for the degradation of pollutants in water and wastewater.

CHAPTER 5

Insights into the role of β-MnO_2 and oxalic acid complex expediting ozonation: Structural properties and mechanism

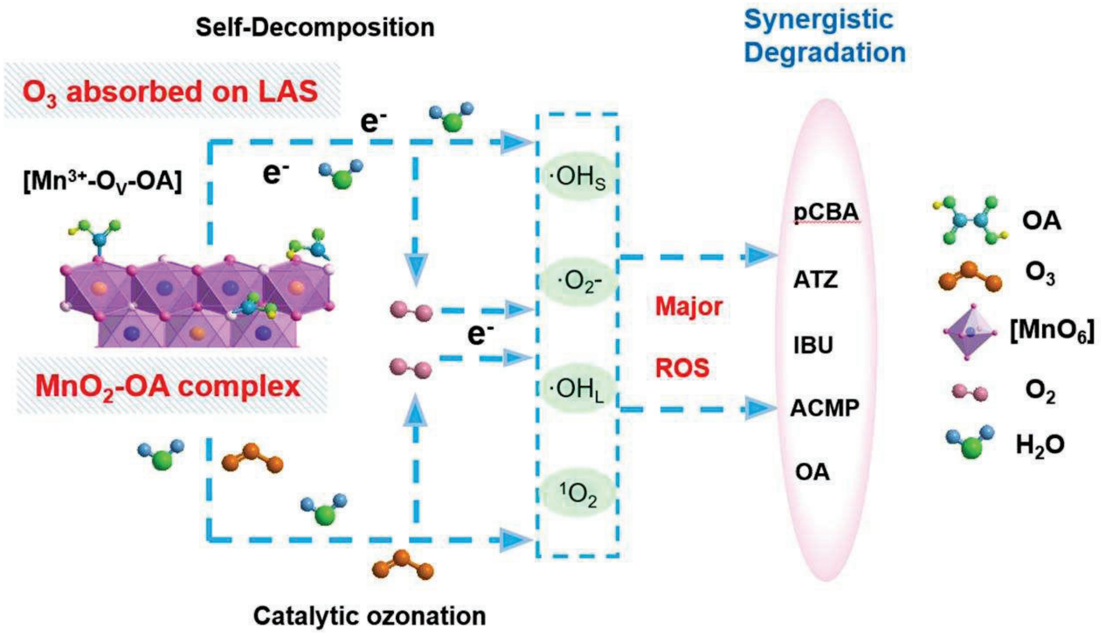

This chapter is redrafted from:

Jing Liu, Xiangjuan Yuan, Carmen Sans, Effect of complexation between manganese dioxides and organic acids on enhancing catalytic ozonation efficiency. Separation and Purification Technology 341 (2024) 126904. https://doi.org/10.1016/j.seppur.2024.126904.

5.1 Introduction

Several researchers worked on complexes and obtained different results. Andreozzi et al [1] pointed out that Mn^{2+} would be oxidized to Mn^{3+} thus forming Mn^{3+}-oxalate complexes, which could act as radical chain initiators to oxidize oxalate ions to oxalate ion radicals, hence promoting the oxidation efficiency. Beltran et at [2] found formation of Fe-oxalate complexes in heterogeneous (Fe_2O_3/Al_2O_3) catalytic ozonation could react with O_3 without the participation of hydroxyl radicals($^{\bullet}OH$). Thus, it could be found that the role of the complexes is not entirely the same. Our previous study (chapter 4) confirmed that the addition of OA (10 mg L^{-1}) into the Cat/O_3 processes would enhance the pollutant removal efficiency. Compared to α-MnO_2/OA/O_3 (71.0%) and δ-MnO_2/OA/O_3 processes (67.1%), β-MnO_2/OA/O_3 system exhibited the optimal pollutant degradation efficiency (76.6%) within 3 min. Therefore, to explore the interaction between MnO_2 and OA, β-MnO_2/OA/O_3 system was selected for further investigation.

In this study, β-MnO_2 was synthesized through the hydrothermal-calcination method and used for constructing β-MnO_2-OA complex in the HCO process. Due to the low reactivity through direct ozonation and high reactivity with $^{\bullet}OH$ ($k_{\bullet OH,pCBA}=5\times10^9$ $M^{-1}S^{-1}$, $k_{O_3,pCBA}\leqslant 0.5$ $M^{-1}S^{-1}$), 4-Chlorobenzoic acid (pCBA) was chosen to evaluate the catalytic ozonation activity [2]. A series of characterization techniques were used to explore the formation, interaction, and surface physicochemical properties between β-MnO_2 and OA. Additionally, the effects of β-MnO_2 dosage and the initial concentrations of O_3 and OA on both pCBA and OA degradation were systematically assessed in the HCO process. Special attention was attracted to recognizing active species and the role of β-MnO_2-OA complex. Ultimately, a feasible interface mechanism of β-MnO_2-OA complex in HCO process was illustrated.

5.2 Material and methods

5.2.1 Reagents

Reagents include 4-Chlorobenzoic acid (pCBA), Ammonium persulfate ($(NH_4)_2S_2O_4$, purity ≥98%), Sodium pyrophosphate (PP, purity ≥95%), tert-butanol (TBA), *p*-benzoquinone (BQ), potassium permanganate ($KMnO_4$), phosphoric acid (H_3PO_4), sodium thiosulfate ($Na_2S_2O_3$), manganese sulphate 1-hydrate ($MnSO_4$), oxalic acid 2-hydrate (OA), sodium azide (NaN_3, 99%), acetonitrile (for UHPLC, super gradient grade, 2,2,6,6-Tetramethyl-1-piperidinyloxy (TEMPO, purity > 97%) and 5,5-dimethyl-1-pyrolin-N-oxide (DMPO, purity > 97%). All aqueous solutions were prepared by Milli-Q system (Merck Millipore, Germany).

5.2.2 Preparation of β-MnO_2 catalyst

The β-MnO_2 was synthesized by a simple hydrothermal method. 3.38 g $MnSO_4$ and 4.56 g $(NH_4)_2S_2O_4$ were dissolved in 80 mL Milli-Q water. After continuously stirring for 2h at room temperature, the suspension was transferred into two 100 mL Teflon-lined stainless-steel autoclaves (Great wall, China) for heating 24 h at 90ºC. More details can be found in CHAPTER 3.

5.2.3 Characterization

The catalysts were characterized by XRD, FT-IR, HRTEM, XPS, H_2-TPR, O_2-TPD and Py-IR. Details of the procedures and parameters applied for characterizations were included in CHAPTER 3.

5.2.4 Catalytic activity tests and analysis

Batch ozonation experiments were conducted in 125mL milli-Q water. All samples (1.5 mL) in the experiments were taken out at a certain time interval under stirring (400rpm). Then quenched with excess $Na_2S_2O_3$ (0.01 M) to remove spare O_3 content. After filtered by 0.45 μm filter, the samples were further determined through High Performance Liquid Chromatography (HPLC). All of the experiments were performed in duplicate.

For adsorption experiments, a specific concentration of pollutants and β-MnO_2 was combined in 125 mL of Milli-Q water. The adsorption capacity of β-MnO_2 for the pollutants was found to be less than 5%, making it negligible.

In the single ozonation process, a defined volume of the O_3 stock solution was introduced into the reactor containing the pre-prepared pollutant solution, resulting in an initial O_3 concentration of approximately 2 mg L^{-1}.For the β-MnO_2/OA/O_3 process, a measured amount of β-MnO_2 catalyst was added to a mixture of OA and pCBA solutions. Subsequently, the appropriate volume of O_3 stock solution was introduced to initiate the catalytic ozonation reaction.

5.3 Results and discussion

5.3.1 The formation and activities of β-MnO_2-OA complex

Based on pre-experiments, introducing β-MnO_2 to the OA solution prior ozonation could promote the formation of β-MnO_2-OA complex, thereby enhancing the catalytic ozonation activity (Fig.5.1). As illustrated in Fig.5.2(a), compare to ozonation (51.6%) for pCBA degradation in 10 min, the β-MnO_2/O_3 system (43.8%) partially inhibited pCBA removal. Notably, the optimum catalytic ozonation performance with 90.4% of pCBA degradation was obtained in the β-MnO_2/OA/O_3 process, and the reaction rate constant (k) rose from 0.364 min^{-1} to 1.541 min^{-1}. Meanwhile, the degradation of OA in β-MnO_2/OA/O_3 system could reach to 65.14% (Fig.5.2(b)). The residual O_3 content in different processes were detected and they are shown in Fig.5.2(c). Compared to ozonation alone, the presence of β-MnO_2 would increase the O_3 depletion rate. Jiménez-López suggested that the accelerated O_3 depletion rate could be solely attributed to ozone adsorption on the catalyst surface [3]. Meanwhile, the effective decomposition of O_3 occurring on the surface of the catalyst can produce reactive oxygen species (ROS) and further promote the degradation of pollutants [4]. The adsorption of O_3 triggers reaction with surface groups, depleting active sites, and suppressing ROS generation, ultimately causing deactivation [3]. Therefore, the slight inhibition of pCBA degradation in the β-MnO_2/O_3 system could be explained by ineffective O_3 utilization. Furthermore, the lowest residual O_3 content was obtained in the β-MnO_2/OA/O_3/pCBA process, suggesting that the newly-formed β-MnO_2-OA complex could promote O_3 decomposition and utilization.

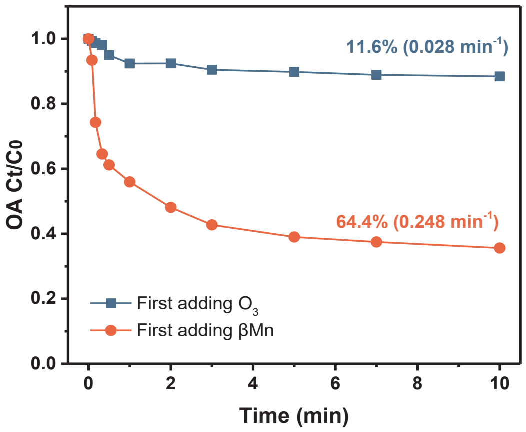

Fig.5.1 The effect of the adding sequence of βMn and O_3 solution on catalytic ozone activity. Experimental conditions: [βMn]=50 mg L^{-1}, $[OA]_0$=10 mg L^{-1}, $[O_3]$=2 mg L^{-1}, pH_0=4.0 ± 0.2.

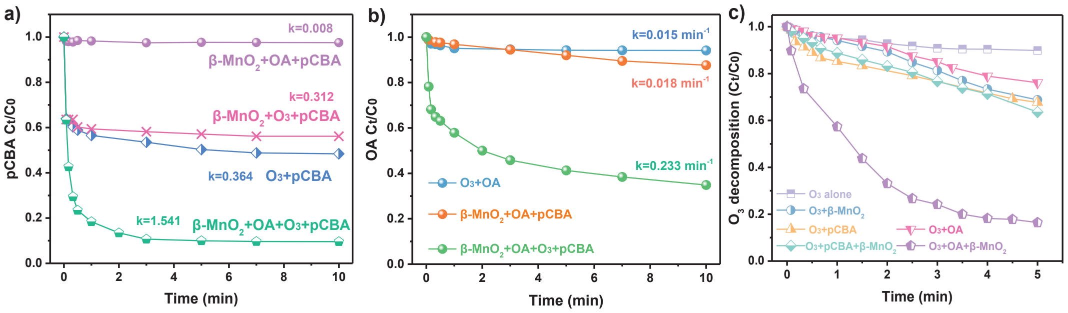

Fig.5.2 a) pCBA removal efficiency, b) OA degradation efficiency, and c) depletion of O_3 in different processes. Experimental conditions: $[pCBA]_0$=0.1 mg L^{-1}, [β-MnO_2]=50 mg L^{-1}, $[OA]_0$=10 mg L^{-1}, $[O_3]$=2 mg L^{-1}, pH_0=4.0 ± 0.2

Some other refractory contaminants such as atrazine (ATZ), acetamiprid (ACMP), and ibuprofen (IBU), were used as target pollutants to assess the efficiency of β-MnO_2/OA/O_3 process (Fig.5.3). The removal efficiencies of ACMP, IBU, and ATZ were increased by 27.96%, 54.18%, and 39.77%, respectively, compared with ozonation alone. The results verified that the β-MnO_2-OA complex in β-MnO_2/OA/O_3 process was conducive to the co-degradation of pollutants in HCO process.

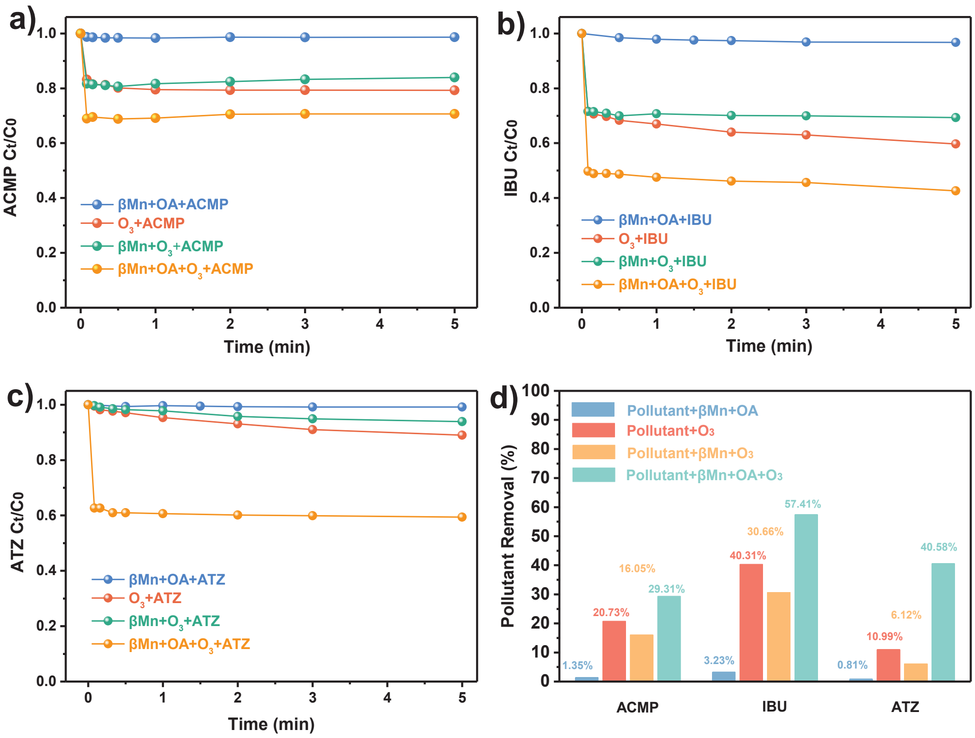

Fig.5.3 a) ACMP, b) IBU, and c) ATZ removal efficiency in different processes, d) the contrast of different pollutants degradation efficiency. Experimental conditions: $[ACMP]_0=[IBU]_0=[ATZ]_0$=5 mg L^{-1}, [βMn]=50 mg L^{-1}, $[OA]_0$=10 mg L^{-1}, $[O_3]$=2 mg L^{-1}, pH_0=4.0.

5.3.2 Effect parameters of β-MnO_2-OA complex application

The formation of β-MnO_2-OA complex was impacted by of β-MnO_2 concentration. When the amount of β-MnO_2 increased to 200 mg L^{-1} in β-MnO_2/O_3 system (Fig.5.4(a)), the strengthen adsorption of O_3 on the surface of catalyst resulted in more active sites being occupied [5]. However, the ineffective O_3 utilization reduced the pCBA removal efficiency to 23.27%. In the β-MnO_2/OA/O_3 process, with the β-MnO_2 dosage increased from 10 to 50 mg L^{-1}, the pCBA degradation raised from 68.83% to 90.4%. However, it decreased to nearly 41.82% as the dosage was further increased to 200 mg L^{-1}. Moreover, the removal of OA in the β-MnO_2/OA/O_3 process rose to approximately 70% (Fig.5.5(a)). The enhanced co-degradation efficiencies of OA and pCBA could be ascribed to the increased availability of active sites, which promotes direct ozonation utilization and ROS generation. [6]. However, excessive amounts of β-MnO_2 would agglomerate to restrict the practicality of active sites, which would influence the formation of β-MnO_2-OA complex depressing O_3 utilization [7, 8].

To investigate the influence of OA concentrations on the generation of β-MnO_2-OA complex, the elimination of pCAB and OA were evaluated in different processes. Owing to the competition between pCBA and OA for the ROS and O_3, the highest degradation efficiency of pCBA (37.96%) and OA (36.48%) was obtained at 2 mg L^{-1} of OA in the ozonation alone, which were shown in Fig.5.4(b) and Fig.5.5(c), respectively. However, for β-MnO_2/OA/O_3 processes, the pCBA degradation rate increased markedly from 41.68 % to 90.4% in 10 mins as OA concentrations rose from 2 mg L^{-1} to 10 mg L^{-1} (Fig.5.5(b)), meanwhile, the elimination efficiency of OA was more than 65% (Fig.5.5(c)). The formation of β-MnO_2-OA complex was affected by the content of OA, which impacted the co-degradation of pCBA and OA.

The influence of various O_3 concentrations (0.5 mg L^{-1} to 7 mg L^{-1}) on pCBA degradation were further explored and presented in Fig.5.4(c). As the O_3 concentration increased, the removal of pCBA in O_3 alone and β-MnO_2/O_3 processes were steadily enhanced. Sole ozonation achieved 57.29% of pCBA removal at 7 mg L^{-1} of O_3, while it was reduced slightly in the presence of β-MnO_2. In contrast, the pCBA elimination efficiency of the β-MnO_2/OA/O_3 system was 97.5% (Fig.5.5(d)) which was more than 1.5 times that of β-MnO_2/O_3 (55.11%). The corresponding OA degradation rates were raised gradually from 33.46% to 97.35%. Moderately increasing the ozone dose would enhance the catalytic ozonation performance of β-MnO2-OA complex, which might rapidly generate more active species through reacting with O_3, promoting the synchronous degradation efficiency of pCBA and OA.

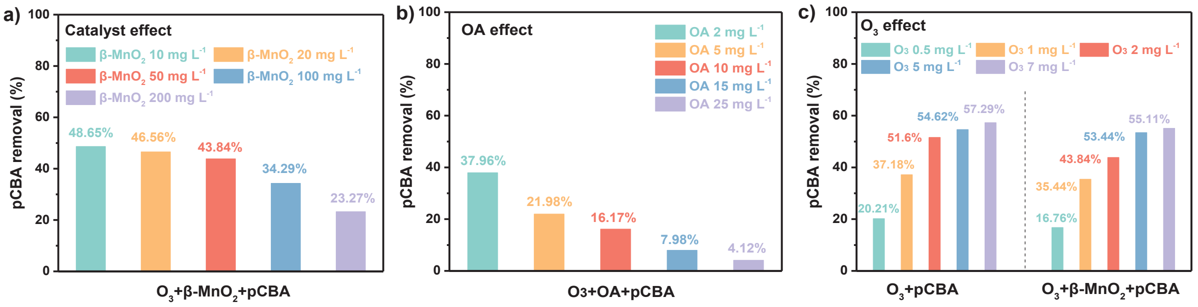

Fig.5.4 The effects of a) catalyst dosage, b) OA concentrations, and c) initial O_3 concentrations on pCBA removal efficiency in different processes. Experimental conditions: $[pCBA]_0$=0.1 mg L^{-1}, [βMn]=50 mg L^{-1} (except a)), $[OA]_0$=10 mg L^{-1} (except b)), $[O_3]$=2 mg L^{-1} (except c)), pH_0=4.0 ± 0.2.

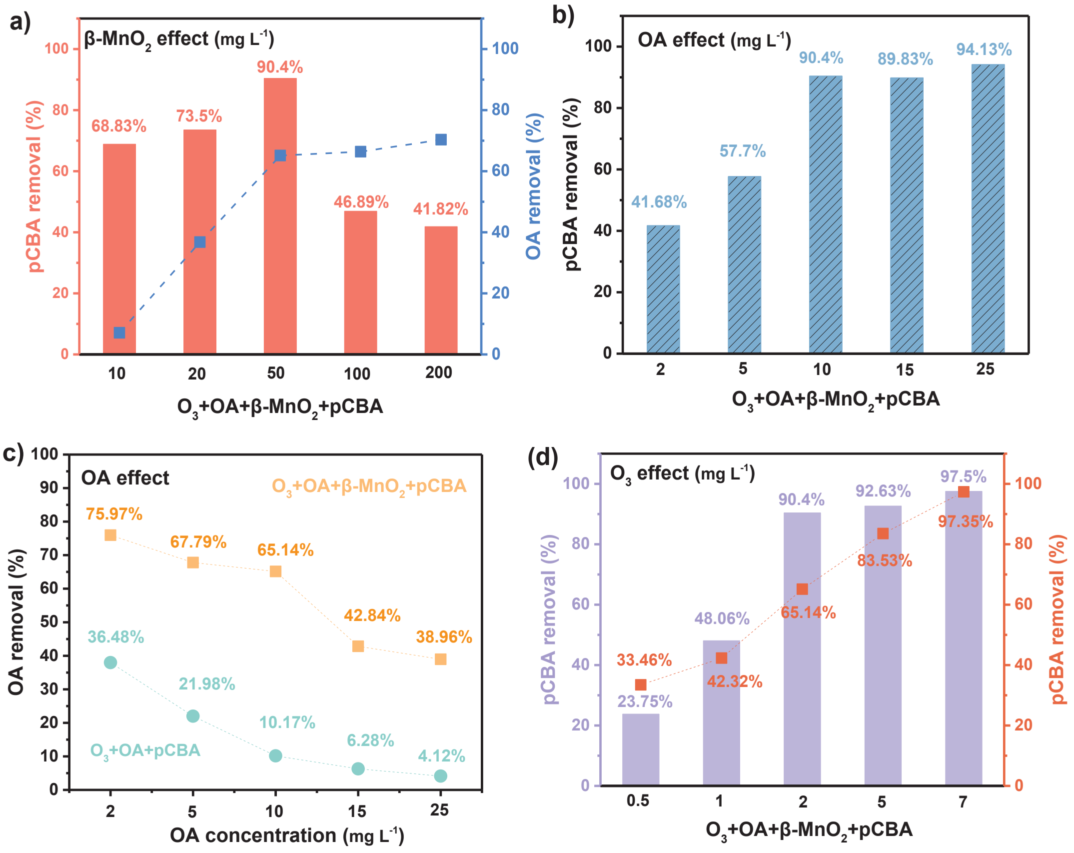

Fig.5.5 The effects of a) catalyst dosage and d) initial O_3 concentrations on pCBA and OA removal efficiency, b) OA concentrations on pCBA removal efficiency, and c) the effects of OA concentrations on OA removal efficiency in different processes. Experimental conditions: $[pCBA]_0$=0.1 mg L^{-1}, $[\beta\text{-}MnO_2]$=10 mg L^{-1} (except a)), [OA]=10 mg L^{-1}(except b) and c)), $[O_3]$=2 mg L^{-1}(except d)), pH_0=4.0 ± 0.2.

5.3.3 Characterizations of·β-MnO$_2$-OA complex

XRD pattern was used for analyzing the crystal structures of pristine β-MnO$_2$ and β-MnO$_2$-OA complex. As described in Fig.5.6(a), the diffraction peaks at the value of 2θ = 28.6°, 37.2°, 42.8°, 56.7°, 59.3°, 64.8°, and 72.2° were indexed to (110), (101), (111), (211), (220), (002), and (301) planes of a typical 1×1 tunnel structure of β-MnO$_2$ (PDF 81-2261) [9]. In contrast, no additional characteristic peaks were observed in the XRD pattern of the β-MnO$_2$-OA, except for a slight shift to a lower angle, indicating an increase in the interplanar distance [10, 11]. The changes in micro lattice structure proved the possibility of complexation between β-MnO$_2$ and OA, via the substitution of atoms with different atomic diameters. Additionally, the relatively weaker diffraction peaks of β-MnO$_2$-OA complex indicated a relatively lower crystallinity, which could offer more efficient diffusion channels for ions, thereby facilitating ions transfer [12].

The FT-IR analysis was performed in the range between 400 and 4000 cm^{-1}, as conducted in Fig.5.6(b) [13]. Same peaks of β-MnO$_2$ and β-MnO$_2$-OA complex found at 428 cm^{-1}, 486 cm^{-1}, at 712 cm^{-1}, 1382 cm^{-1}, 1483 cm−1, 1630 cm^{-1}, and 3500 cm^{-1} could be related to the vibrations of Mn−O bonds, Mn−O−Mn bonds, O−H bonds, H−O−H bonds, and the surface-adsorbed water species and hydroxyl groups, respectively [9, 14, 15], confirming the structural integrity of catalyst after the formation of β-MnO$_2$-OA complex. Moreover, several small peaks detected at around 2800 cm^{-1} were corresponded to the C−H symmetrical bending and stretching vibration of ethanol that used for drying materials in the analytic process [16]. It could be observed that the more intensified peaks of −OH groups were observed in β-MnO$_2$-OA complex, due to the intercalation of water molecules into tunnel structure during complex formation process [17].

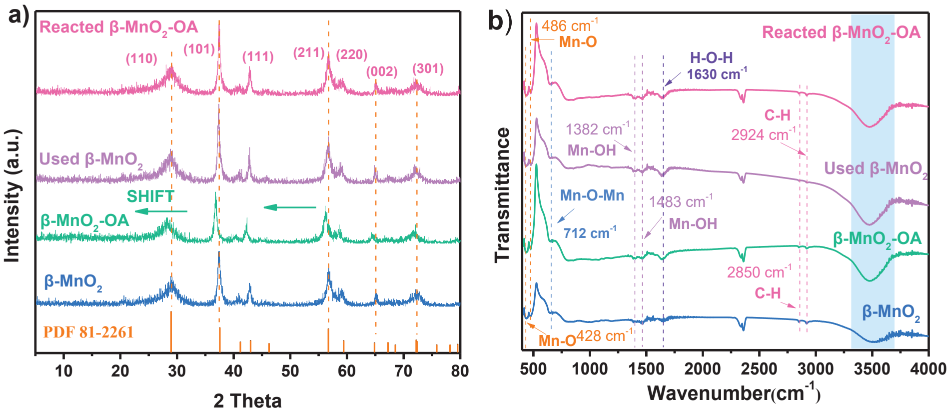

Fig.5.6 XRD patterns a) and FT-IR imagines b) of different catalysts.

The TEM image of β-MnO$_2$ revealed a mixture of nanorods with a diameter ranging from 20-100 nm (Fig.5.7(a, b)) and an interplane spacing of 0.24 nm was observed in Fig.5.7(c) corresponding to the (101) plane of β-MnO$_2$, which confirmed the successful synthesis of β-MnO$_2$ nanorods structure [18]. As shown in Fig.5.7(d, e), β-MnO$_2$-OA complex consisted of small rods, with some showing a tendency to aggregate and form larger particle complexes. The lattice fringe distances of 0.16 nm and 0.24 nm detected in Fig.5.7(f) could be also consistent with (211) and (101) lattice spaces of β-MnO$_2$ respectively [19]. In addition, the peaks in the spectrum of β-MnO$_2$ (Fig.5.7(g)) were ascribed to elemental Mn (56.3%) and O (43.7) only, extra elemental C (54.1%) discovered in Fig.5.7(h) was the evidence for the existence of β-MnO$_2$-OA complex. However, compared with the exposed facets of two composites, it was found that the lattice fringes sharpness of β-MnO$_2$-OA complex became blurry (red cycle), indicating the generation of crystal defect during the formation of complexes [20]. Meanwhile, as the length of nanorods decreased, the electron (e$^-$) transport was shortened, and the ion diffusion paths were also reduced. This facilitated easier e$^-$ transfer, thus enhancing the chemical performance of composite [11].

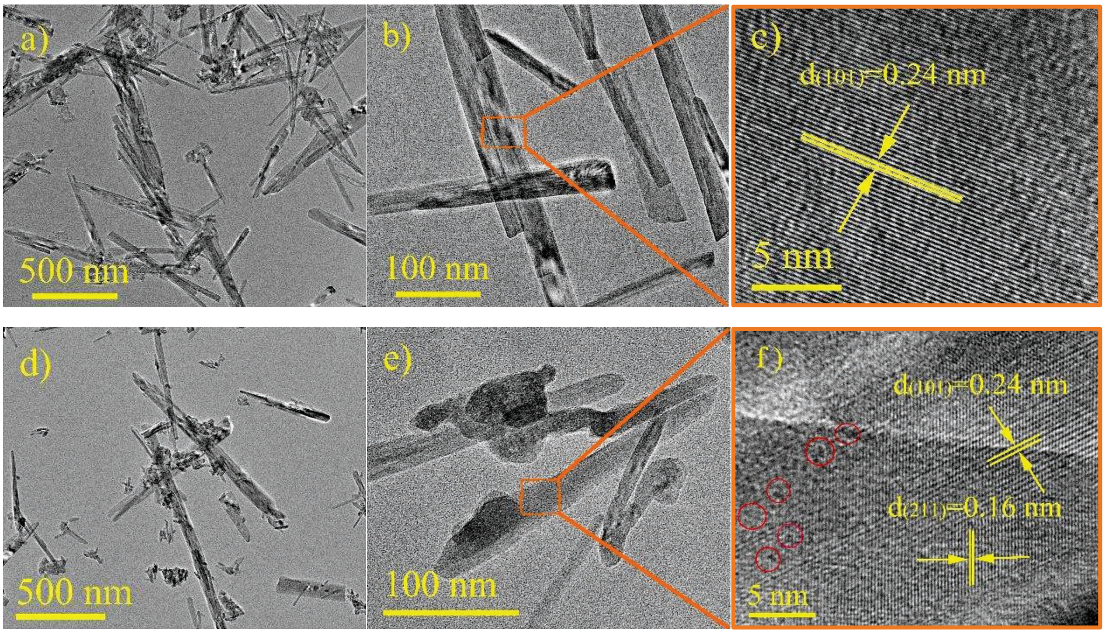

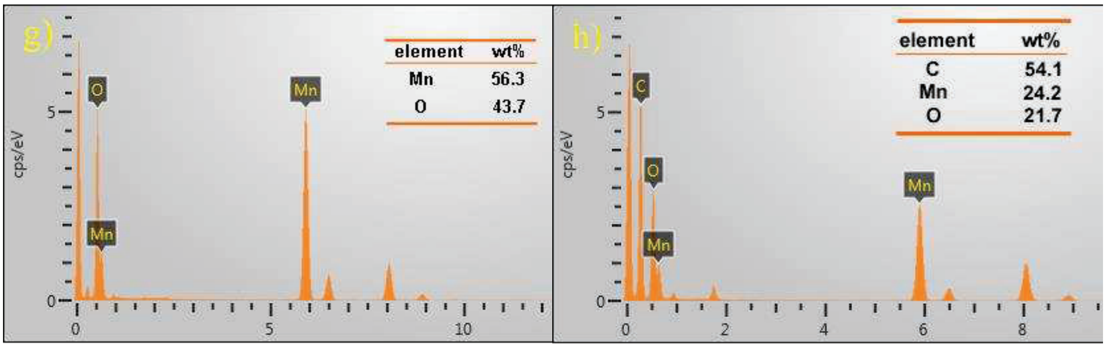

Fig.5.7 TEM images of β-MnO_2 (a, b) and β-MnO_2-OA complex (d, e), HRTEM images of β-MnO_2 (c) and β-MnO_2-OA complex (f), EDS mapping of β-MnO_2 (g) and β-MnO_2-OA complex (h)

As described in Fig.5.8(a), H_2-TPR was conducted with the temperature range of 50ºC−850ºC to reveal the manganese valence evolution [21]. The low-temperature reduction peaks of β-MnO_2 (384ºC) and β-MnO_2-OA complex (334ºC) might be attributed to the reduction of Mn^{4+} to Mn^{3+}/Mn^{4+}, the higher-temperature reduction peaks of β-MnO_2 (535ºC) and β-MnO_2-OA complex (441ºC) could be due to the reduction of Mn^{3+}/Mn^{4+} to Mn^{2+} [22]. In addition, when the temperature of H_2-TPR decreased, lattice oxygen (O_{lat}) reduced into surface absorbed oxygen (O_{abs}) gradually [23]. The peaks of β-MnO_2-OA complex were significantly shifted to the lower temperature, indicating the presence of more high-valent Mn species and active surface oxygen species [24]. Besides, the peak intensity of β-MnO_2-OA complex was remarkably stronger than that of β-MnO_2, which illustrated that more oxygen-containing functional groups over β-MnO_2-OA complex might be generated [25]. The above results suggested that the combination of OA with β-MnO_2 could effectively promote the catalyst redox property [24].

The activation and interaction of oxygen with catalysts were further studied by O_2-TPD in Fig.5.8(b). The desorption peaks could be divided into two parts: high temperature (HT, ＞500ºC) allocated to the O_{lat} and low temperature (LT, ＜500ºC) corresponded to the O_{abs} [26]. Here, β-MnO_2-OA complex provided a desorption peak at lower temperature of 140ºC implying the easier releasing of unstable oxygen, which would improve the mobility of active oxygen. Besides, the increased O_{abs} amount of β-MnO_2-OA complex was detected at 401ºC, indicating the higher oxygen storage capacity and more oxygen vacancies (O_V) [27]. Furthermore, a stronger peak of β-MnO_2-OA complex appeared at lower temperature (503ºC) testified the production of more active O_{lat} [20]. Overall, the generation of β-MnO_2-OA complex possessed more active oxygen species and higher oxygen migration ability.

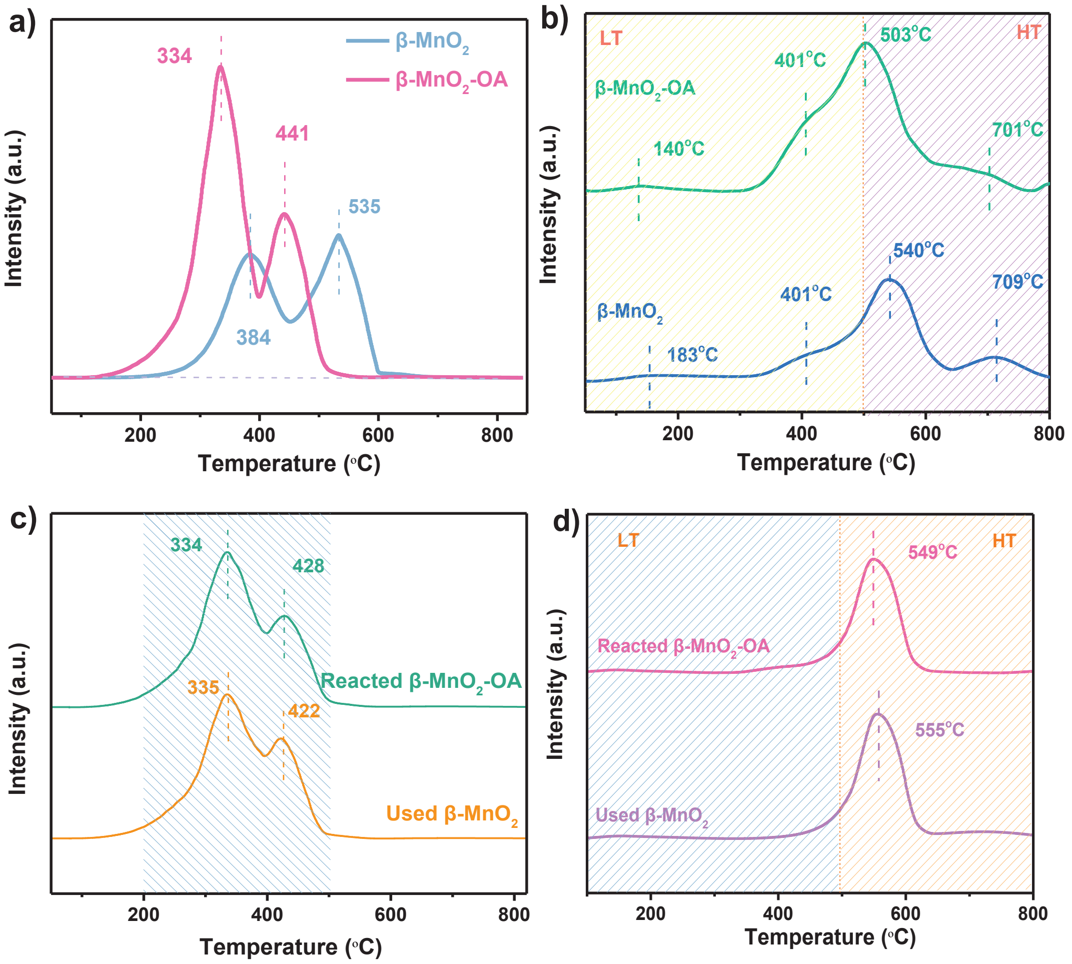

Fig.5.8 H_2-TPR profiles a) and c) of various catalysts, and O_2-TPD profiles b) and d) of various catalysts

The XPS survey spectrum illustrated in Fig.5.9(a) verified the presence of Mn 3s, O 1s, C 1s, and Mn 2p states of β-MnO_2 and β-MnO_2-OA complex [28]. As displayed in C 1s XPS pattern (Fig.5.9(b)), three peaks of β-MnO_2 located at 288.8 eV, 286.1 eV, and 284.8 eV were gained, corresponding to O−C=O, C−O, and C−C or/and C=C bonds, respectively, which could be attributed to the involvement of carbon-related materials that were required during testing process [29]. Due to the combination of OA, the O−C=O ratio of β-MnO_2-OA complex was increased to 11.44%.

In the Mn 2p signals of β-MnO_2 and β-MnO_2-OA complex (Fig.5.9(c)), two major peaks centered at 654.0 eV and 642.2 eV and could be fitted to the spin-orbit doublet of the Mn $2p_{1/2}$ and Mn $2p_{3/2}$ states. The binding energy gap (11.8 eV) perfectly matched the typical spin energy separation of β-MnO_2 structure [30]. The asymmetric peaks appeared at approximately 643.7 eV and 654.9 eV could be indexed to Mn^{4+} [31], verifying the existence of bulk MnO_6 octahedron (O−Mn−O) and the surface O−Mn−OH structure [16]. The peaks at 653.6 eV and 642.1 eV could be related to Mn^{3+}, which increased from 51.68% to 66.79% and 51.04% to 73.13% respectively during the formation of β-MnO_2-OA complex [31]. Therefore, more O_V would be created to maintain charge neutrality.

The O 1s spectra was further employed to investigate the chemical bonds of oxygen in Fig.5.9(d), three peaks at around 531.6 eV, 530.2 eV, and 529.7 eV of β-MnO_2 allocated to the O_{abs} (22.99%), surface Mn−O−OH (28.44%), and Mn−O−Mn (O_{lat}, 48.57%) [15, 16], respectively. Nevertheless, the larger peak of O_{lat} for β-MnO_2-OA (72.51%) shifted to a lower level (529.5 eV) and the disappearance of peak for surface−OH, implying a change in the Mn−O coordination configuration resulting from the chemical bond between β-MnO_2 and OA [27]. Additionally, β-MnO_2-OA complex exhibited an aggrandized intensity of O_{abs} (27.49%) suggesting it had more O_V. The XPS patterns further confirmed that the formation of the β-MnO_2-OA complex was driven by chemical bonding rather than simple physical adsorption. This led to an increase in Mn^{3+} and oxygen vacancies, which in turn enhanced the catalytic properties of the composite.

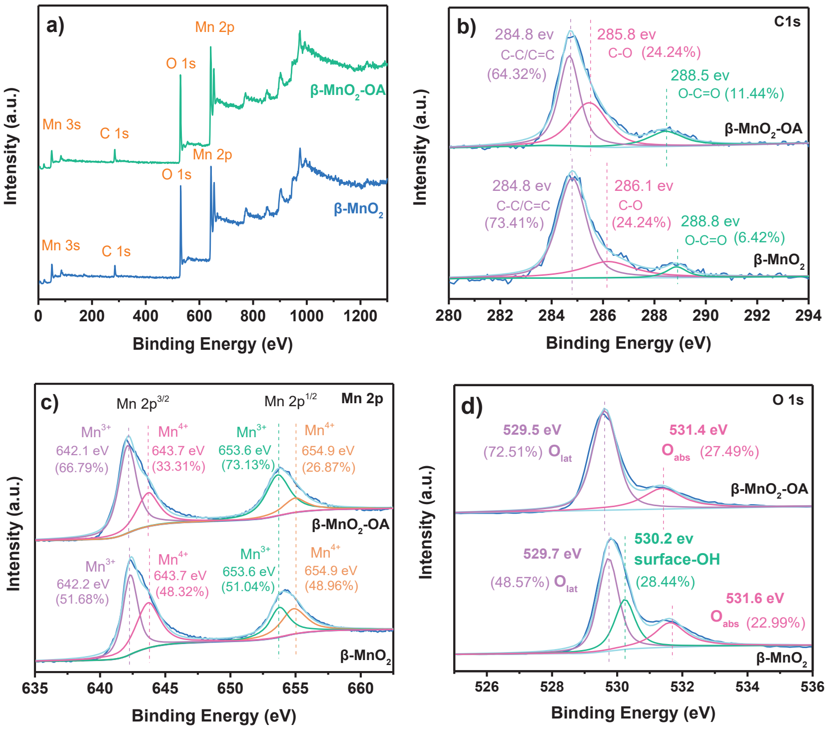

Fig.5.9 XPS spectra of β-MnO_2 and β-MnO_2-OA complex survey spectra a), C 1s b), Mn 2p c), and O 1s d)

The surface acidity of catalysts was discussed by the pyridine-IR measurements displayed in Fig.5.10. Two types of surface acid sites, namely Bronsted acid sites (B-acid) and Lewis-acid sites (L-acid), were associated with the exchange of free electrons and proton at metal oxides [32]. The peak the peaks at 1450 cm^{-1} and 1610 cm^{-1} originated from pyridine adsorbed on L-acid, the bands at 1545 cm^{-1} and 1641 cm^{-1} were due to B-acid, and the peak at 1490 cm^{-1} were related to L- and B-acid [26]. The amounts of L- and B-acid sites were plotted in Fig.5.11. Clearly, L-acid as the core active sites dominated B-acid in quantity for β-MnO_2 and β-MnO_2-OA complex, which could facilitate the activation of surface oxygen species to generate ROS [26]. And β-MnO_2-OA complex possessed more total acids sites not only at 150ºC (95.18 μmol/g) but also at 300ºC (44.41 μmol/g) (Table 5.1), providing explicit evidence of the improved distribution and strength of surface-active sites.

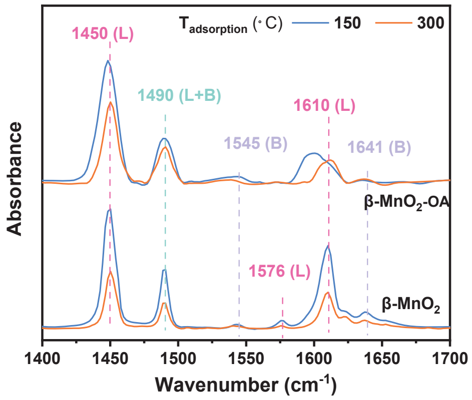

Fig.5.10 Pyridine-IR spectra of β-MnO_2 and β-MnO_2-OA complex at 150ºC and 300ºC

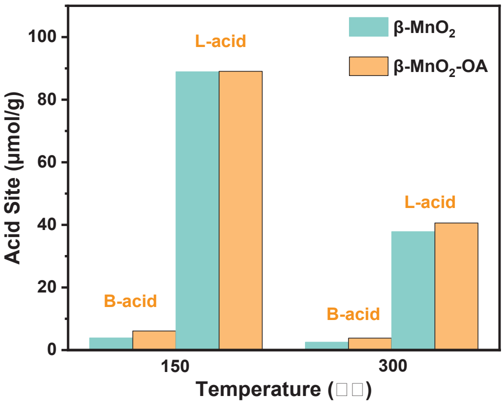

Fig.5.11 Amounts of the Lewis-acid sites and Bronsted-acid sites over these two samples plotted against the adsorption temperature of pyridine.

Table 5.1 Summary of surface acidity of catalyst by pyridine-IR measurement.

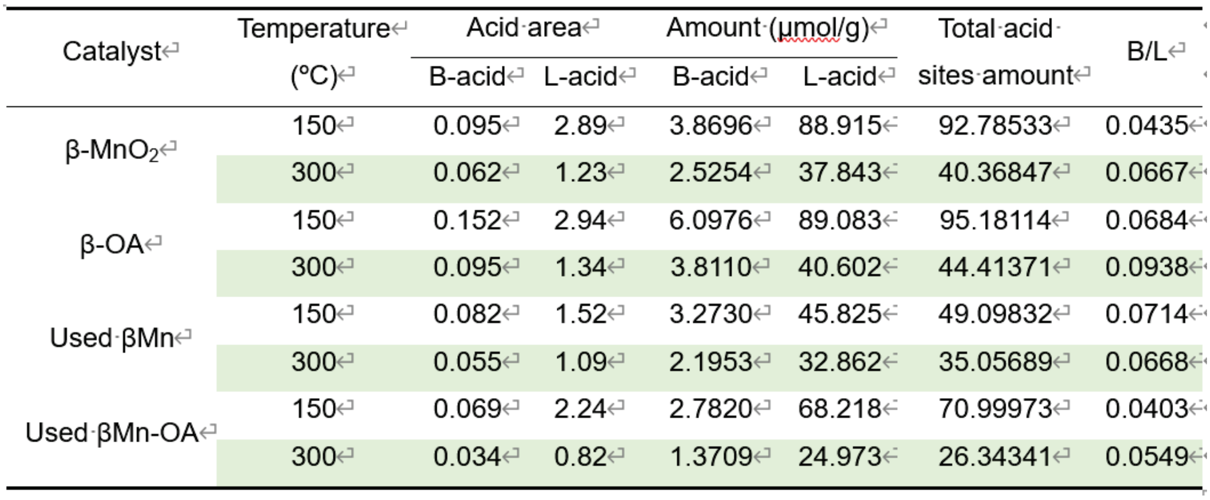

Catalyst	Temperature (°C)	Acid area		Amount (μmol/g)		Total acid sites amount	B/L
		B-acid	L-acid	B-acid	L-acid		
β-MnO_2	150	0.095	2.89	3.8696	88.915	92.78533	0.0435
	300	0.062	1.23	2.5254	37.843	40.36847	0.0667
β-OA	150	0.152	2.94	6.0976	89.083	95.18114	0.0684
	300	0.095	1.34	3.8110	40.602	44.41371	0.0938
Used βMn	150	0.082	1.52	3.2730	45.825	49.09832	0.0714
	300	0.055	1.09	2.1953	32.862	35.05689	0.0668
Used βMn-OA	150	0.069	2.24	2.7820	68.218	70.99973	0.0403
	300	0.034	0.82	1.3709	24.973	26.34341	0.0549

Based on the aforementioned results, the complexation between the β-MnO_2 and OA was driven by the formation of chemical bonds, without altering the structural integrity of the β-MnO_2 catalyst. In the β-MnO_2-OA complex, the shortened ion diffusion paths facilitated the e^- transfer, thereby accelerating O_3 decomposition chain reactions. The H_2-TPR and O_2-TPD results confirmed the enhanced redox property and higher oxygen migration ability of β-MnO_2-OA complex, which favor the generation of more ROS. Furthrmore, the improved distribution and strength of surface-active sites for β-MnO_2-OA complex would enhance the adsorption of O_3, promoting its decomposition to produce more ROS and increasing pollutant degradation.

5.3.4 Identification of reactive species

Pyrophosphate (PP) could form a strong and stable complex with Mn^{3+} (log $k_{apparent}$ = 31.35), therefore, it was used as a scavenger or complexing agent of Mn^{3+} [33, 34] to identify the role of Mn^{3+} in the β-MnO_2/OA/O_3 process. As shown in Fig.5.12, the degradation rates of pCBA (0.1 mg L^{-1}) were 90.1%, 33.21%, and 7.76%, respectively, with PP concentrations of 0, 0.4 and 1 mM. Meanwhile, the OA removal efficiencies were also depressed from 65.14% to 18.12%. These results indicate that PP could inhibit the formation of β-MnO_2-OA complex by reacting with Mn^{3+} through a complex reaction. The direct reaction between O_3 and β-MnO_2-OA complex was hindered, limiting ROS generation and thus suppressing the synchronous degradation of pCBA and OA.

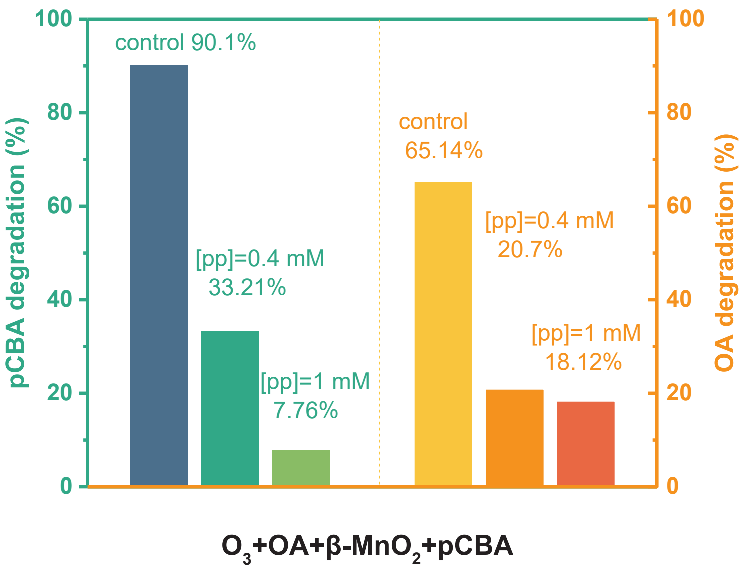

Fig.5.12 Effects of sodium pyrophosphate on pCBA removal efficiency and OA degradation efficiency inset. Experimental conditions: $[pCBA]_0$=0.1 mg L^{-1}, [β-MnO_2]=50 mg L^{-1}, [OA]=10 mg L^{-1}, [O_3]=2 mg L^{-1}, $[PP]_0$=0.4 and 1 mM

Methanol was selected as scavenger to quench $^{\bullet}OH$ in the liquid phase ($^{\bullet}OH_L$) and on the catalyst surface ($^{\bullet}OH_S$), while TBA was used as a scavenger for $^{\bullet}OH_L$ [35]. As shown in Fig.5.13(a), the addition of TBA in the β-MnO_2/OA/O_3 system reduced the pCBA degradation from 90.4% to 15.45%, while methanol almost completely inhibited pCBA degradation, lowering it to just 6.26%. Similar, TBA and methanol hindered the degradation of OA to 51.30% and 34.20%, respectively (Fig.5.13(b)). The results indicated that both $^{\bullet}OH_S$ and $^{\bullet}OH_L$ played significant roles in β-MnO_2/OA/O_3 system. Additionally, the ESR spectrum (Fig.5.14) displayed signals of DMPO-$^{\bullet}OH$ and DMPO-$^{\bullet}O_2^-$ adducts with typical intensity ratios of 1:2:2:1 and 1:1:1:1, respectively. A signal with a peak intensity pattern of 1:1:1, corresponding to TEMP-$^1O_2$ was also detected. These findings further verified the involvement of $^{\bullet}OH$, $^{\bullet}O_2^-$, and $^1O_2$ as active species in β-MnO_2/OA/O_3 process.

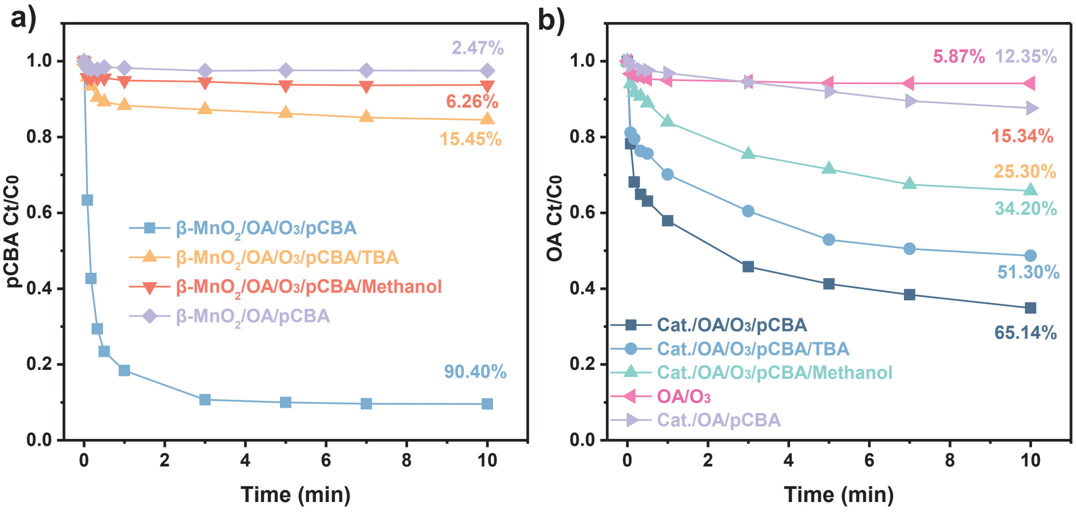

Fig.5.13 a) Effects of various scavengers on pCBA removal efficiency and b) OA degradation efficiency. Experimental conditions: $[pCBA]_0$=0.1 mg L^{-1}, [β-MnO_2]=50 mg L^{-1}, [OA]=10 mg L^{-1}, [O_3]=2 mg L^{-1}, [TBA]=1 mM, [Methanol]=2 mM.

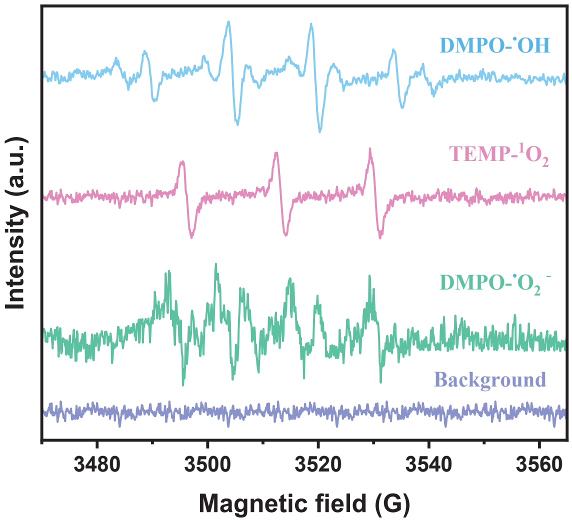

Fig.5.14 TEMP and DMPO trapped ESR spectra in β-MnO_2/OA/O_3 system.

5.3.5 The degradation mechanism of the β-MnO_2/OA/O_3 system.

As displayed in XRD patterns (Fig.5.6(a)), the peak of β-MnO_2-OA complex shifted to the low temperature, suggesting the microstructure change resulted from interaction between β-MnO_2 and OA. However, the peak shift of used β-MnO_2-OA complex disappeared. The co-degradation of OA in β-MnO_2/OA/O_3 system would influence the structure of the β-MnO_2-OA complex, implying the complexation of β-MnO_2 with OA, which markedly influenced catalytic ozonation.

Furthermore, compared to the β-MnO_2-OA complex (Fig.5.6(b)), the FT-IR spectrum of reacted β-MnO_2-OA complex showed a decrease in the intensity of Mn−O bonds and Mn−O−Mn modes. O_3 adsorbed onto the surface-active site of β-MnO_2-OA complex and reacted with surface groups, leading to the release of active O_{lat}. This process influenced the structure of Mn−O and Mn−O−Mn bonds.

The TEM images (Fig.5.15(a)) of reacted β-MnO_2-OA complex displayed three neighboring lattice fringes (and 0.14 nm, 0.24 nm, and 0.16 nm), which could be indexed to (002), (101), and (211) planes of β-MnO_2, respectively (Fig.5.15(b, c)). And the C element purity of notably reduced from 54.1% (Fig.5.7(h)) to 5.7% (Fig. 5.15(d)), further verifying β-MnO_2-OA complex bond breaking during the HCO process.

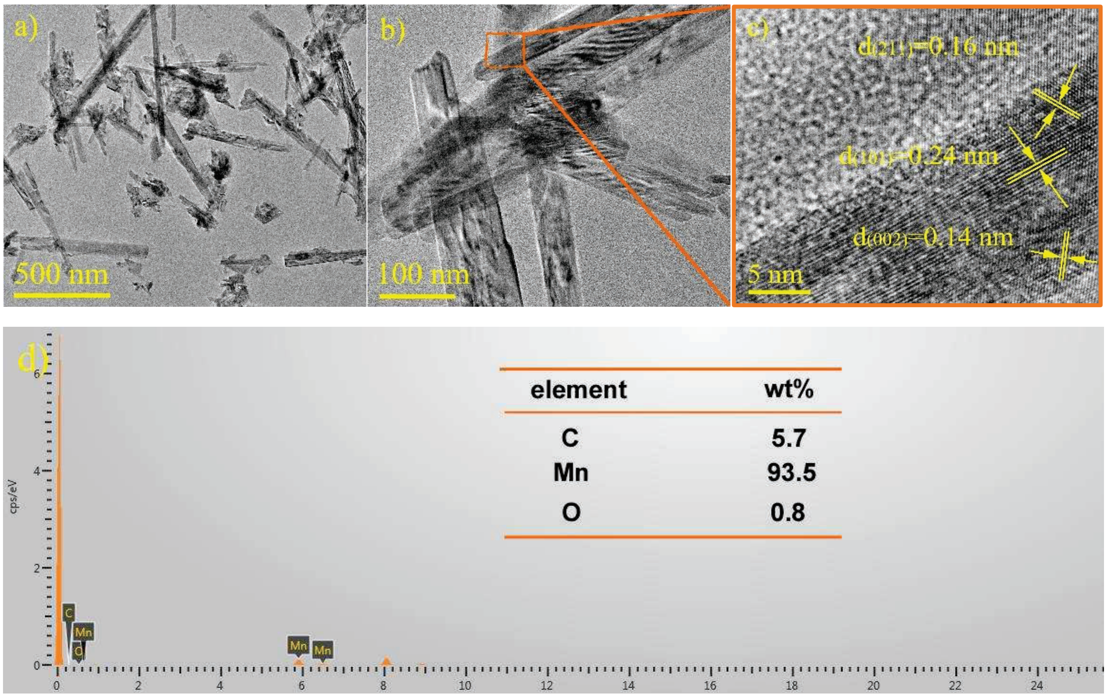

element	wt%
C	5.7
Mn	93.5
O	0.8

Fig.5.15 TEM images of actived βMn-OA complex in catalytic ozonation system.

The XPS results of the reacted β-MnO_2-OA complex are shown in Fig.5.16. It is noteworthy that the intensity of O−C=O for reacted β-MnO_2-OA complex decreased from 11.44% (Fig.5.9(b)) to 9.96% (Fig.5.16 (b)), the complexation has been affected by the degradation of OA. As revealed in Mn 2p spectrum (Fig.5.16(c)), the percentage of Mn^{4+} (Mn $2p_{1/2}$) increased from 26.87% to 44.85%, while the content of Mn^{3+} decreased from 73.13% to 55.15%. The decline of Mn^{3+} content could disfavor the sustained presence of β-MnO_2-OA complex. Compared to the used β-MnO_2 (Fig.5.17), there were three peaks of Mn^{3+} (641.9 eV), Mn^{4+} (642.9 eV), and Mn^{2+} (645.0 eV) in reacted β-MnO_2-OA complex [30] (Fig.5.16(c)). The presence of multivalent states of

Mn would strengthen the e⁻ transfer in the β-MnO_2/OA/O_3 system. Moreover, the H_2-TPR profiles of used β-MnO_2 and reacted β-MnO_2-OA complex (Fig.5.8c) with two reduction peaks (200ºC−450ºC) also confirmed the Mn valence changes during catalytic ozonation reaction [32].

As demonstrated in Fig.5.16(d), the ratio of O_{abs}/O_{lat} (0.45) in the O 1s spectra of reacted β-MnO_2-OA complex was higher than that of the fresh β-MnO_2-OA complex (0.38), implying more O_{abs} was generated and more O_{lat} participated in catalytic ozonation reaction. Furthermore, a strong desorption peak at 500ºC−600ºC in O_2-TPD spectra of reacted β-MnO_2-OA complex (Fig.5.8(d)) further exhibited the release of more O_{lat} from the layer closed to the surface [36].

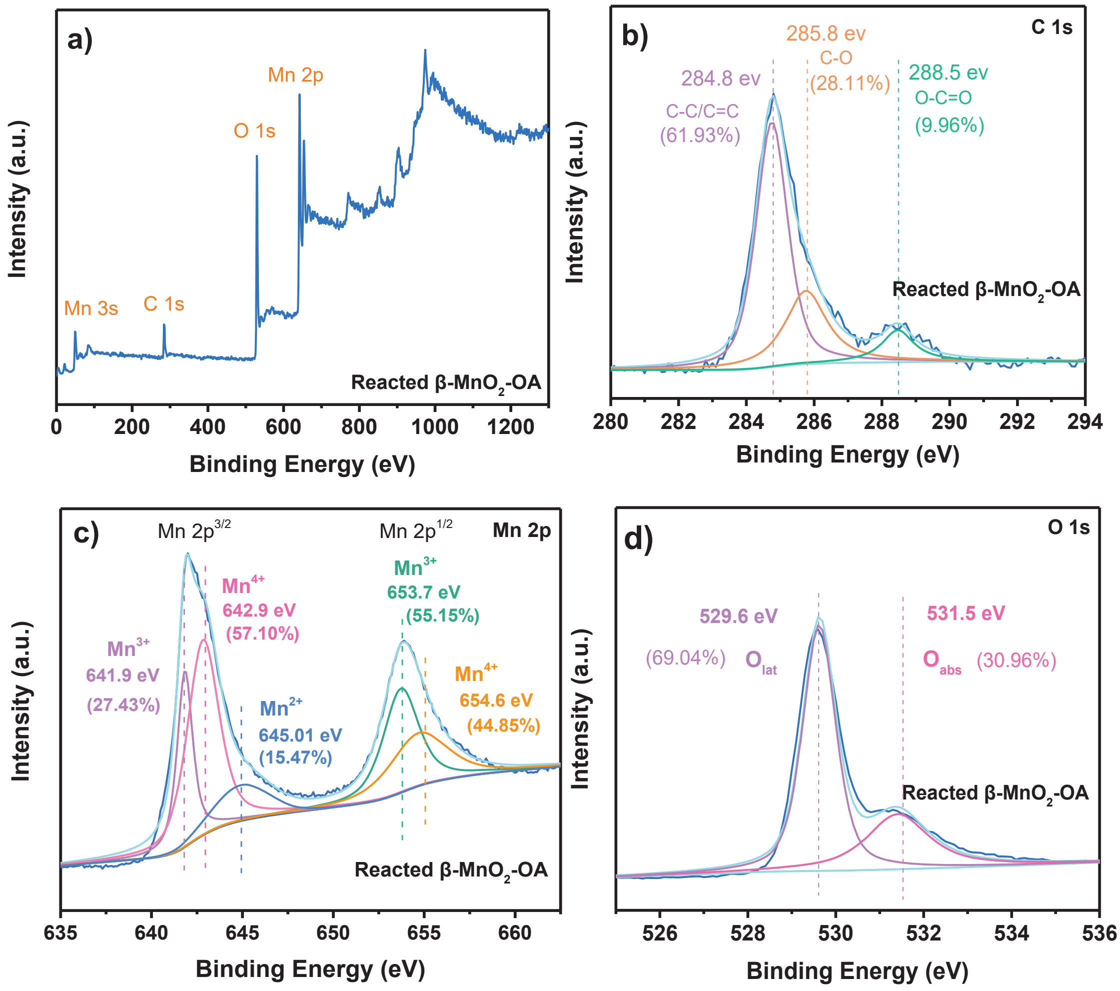

Fig.5.16 XPS images of reacted β-MnO_2-OA complex in survey spectra a), C 1s b), Mn 2p c), and O 1s d).

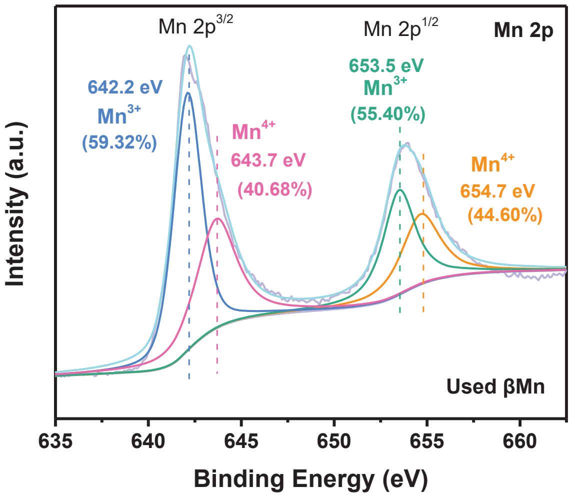

Fig.5.17 XPS image of used βMn in Mn 2p spectrum.

Besides, as exhibited in Table 5.1, the total acid sites of reacted β-MnO_2-OA complex were reduced from 95.18 μmol/g to 70.99 μmol/g and 44.41 μmol/g to 26.34 μmol/g. It was indicated that L-acid (LAS), acting as core active sites, would be occupied when O_3 was adsorbed on the surface [7]. The existence of β-MnO_2-OA complex provides additional active sites for O_3 adsorption. This facilitated a series of O_3 chain reactions, leading to the generation of ROS, through e^- transfer, lattice oxygen releasing, and surface oxygen migration. Ultimately, the co-degradation of OA and pCBA would be achieved in the HCO process, which may disrupt the complexation structure of β-MnO_2-OA.

In conclusion, a feasible mechanism of co-degradation of pCBA and OA in β-MnO_2/OA/O_3 system was proposed. As displayed in Eq.(5.1), β-MnO_2-OA complex was formed due to presence of Mn^{3+}, while additional Ov was created to maintain charge neutrality. A H_2O molecule would be adsorbed and occupy the surface Ov forming surface-OH^{2+} [37]. This surface-OH^{2+} then transformed into surface-$^{\bullet}OH$ with the release of protonated ozone radical ($HO_3^{\bullet}$, Eqs.(5.2-5.3)), which would further decompose to produce $^{\bullet}OH$ (Eq.(5.4)). The coexistence of surface-$^{\bullet}OH$ and $^{\bullet}OH_L$ could facilitate the degradation efficiency of pCBA.

$$MnO_2+OA+H_2O \rightarrow [Mn^{3+} - O_V - OA]+O_2 \tag{5.1}$$

$$O_V+H_2O \rightarrow surface - OH_2^{+} \tag{5.2}$$

$$\text{surface} - \text{OH}_2^+ + \text{O}_3 \rightarrow \text{surface} - {}^{\bullet}\text{OH} + \text{HO}_3^{\bullet} \quad (5.3)$$

$$\text{HO}_3^{\bullet} \rightarrow {}^{\bullet}\text{OH} + \text{O}_2 \quad (5.4)$$

The releasing of O_{lat} were achieved as displayed in Eqs.(5.5-5.6) [38]. Additionally, the improved redox properties would accelerate e⁻ transfer between multivalent states of Mn species (Eqs.(5.7-5.8)). The reaction between O_2^-/ O_2^{2-} and O_3 could create other ROS ($O_2^{\bullet-}$/$^1O_2$/$^{\bullet}OH$) through charge-transfer interactions (Eq.(5.9)). Finally, OA could be attacked by ROS to produce CO_2 and O_2 through desorption and e⁻ rearrangement (Eq.(5.10)).

$$\begin{aligned}[\text{Mn}^{3+} - \text{O}_\text{V} - \text{OA}] - LAS + \text{O}_3 &\rightarrow [\text{Mn}^{3+}/\text{Mn}^{4+}] - \text{O} - \text{O}_3 \\ &\rightarrow [\text{Mn}^{3+}/\text{Mn}^{4+}] - \text{O}_2^- + \text{O}_2\end{aligned} \quad (5.5)$$

$$2[\text{Mn}^{3+}/\text{Mn}^{4+}] - \text{O}_2^- \rightarrow [\text{Mn}^{3+}/\text{Mn}^{4+}] - \text{O}_2^{2-} + \text{O}_\text{abs} \quad (5.6)$$

$$2\text{Mn}^{3+} + 2\text{H}_2\text{O} \rightarrow \text{Mn}^{2+} + \text{MnO}_2 + 4\text{H}^+ \quad (5.7)$$

$$[\text{Mn}^{3+}/\text{Mn}^{4+}] \overset{e^-}{\leftrightarrow} [\text{Mn}^{3+}/\text{Mn}^{4+}/\text{Mn}^{2+}] \quad (5.8)$$

$$[\text{O}_2^-/\text{O}_2^{2-}] + \text{O}_3 + \text{H}_2\text{O} \overset{e^-}{\rightarrow} [{}^{\bullet}\text{OH}/{}^1\text{O}_2/\text{O}_2^{\bullet-}] \quad (5.9)$$

$$\text{OA} + [{}^{\bullet}\text{OH}/{}^1\text{O}_2/\text{O}_2^{\bullet-}] \rightarrow [\text{Mn-O}] + \text{CO}_2 + \text{H}_2\text{O} \quad (5.10)$$

5.4 Conclusions

The β-MnO_2-OA complex, derived from β-MnO_2 synthesized via the hydrothermal method, demonstrated a significant enhancement in ozonation efficiency. Within just 10 minutes, 90.4% degradation of pCBA and 65.2% removal of OA were achieved using 50 mg L^{-1} of β-MnO_2, 10 mg L^{-1} of OA, and a minimal O_3 concentration of 2 mg L^{-1}. Moreover, the rate constant (k) for the β-MnO_2/OA/O_3 system reached 1.541 min^{-1}, quadrupling that of ozonation alone (0.364 min^{-1}). Increasing the O_3 concentration to 7 mg L^{-1} enabled near-simultaneous complete elimination of both compounds. The study delved into the bonding interactions and surface physicochemical characteristics of the β-MnO_2-OA complex through comprehensive characterization methods.

Findings highlighted the crucial role of Mn^{3+} in forming the β-MnO_2-OA complex. This complexation enhanced the electron transfer capability, improved redox properties, and generated more active Ov on the catalyst surface, leading to superior catalytic activity. Radical scavenger experiments further revealed that pCBA degradation was primarily driven by the presence of $^{\bullet}OH_S$ and $^{\bullet}OH_L$ radicals, with other ROS, such as $O_2^{\bullet-}$ and $^1O_2$, contributing to OA removal. In summary, the research provided deeper insights into the complexation between OA and Mn-based catalysts, advancing the understanding of catalytic ozonation processes in aqueous systems.

CHAPTER 6

Muti-MnO_2-oxalic acid complexes mediated catalytic ozonation: Phase effects, ROS contribution and Mechanisms

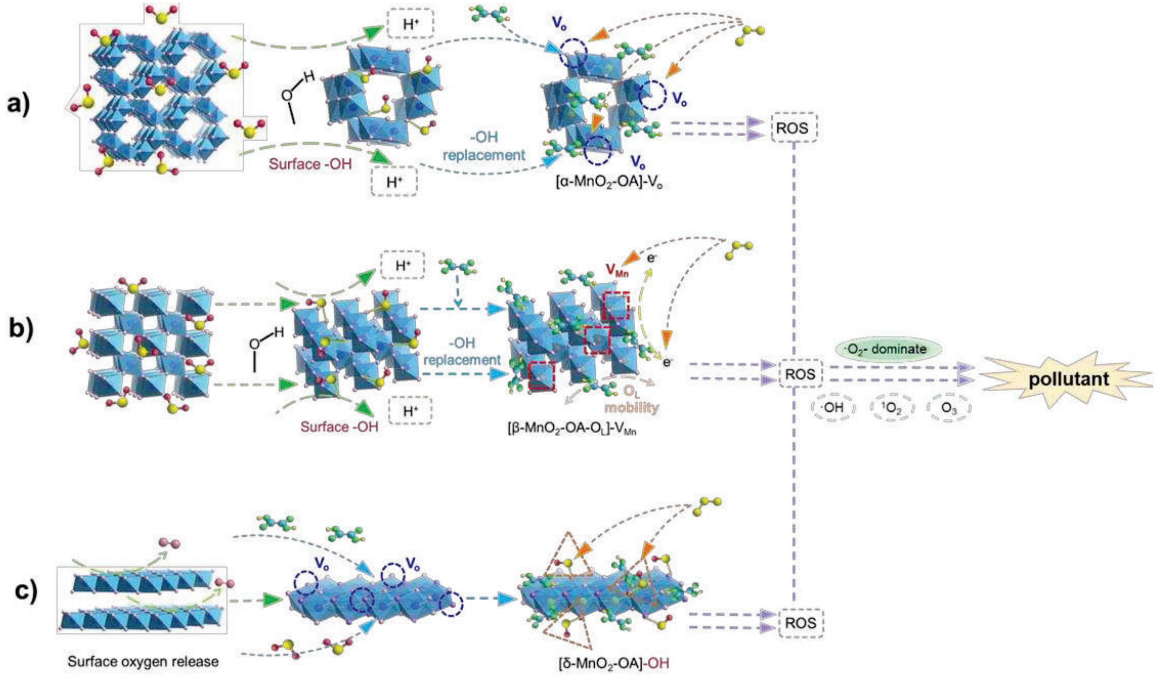

This chapter is redrafted from:

Jing Liu, Xiangjuan Yuan, Carmen Sans, Exploring Phase Effects and ROS Contributions in Catalytic Ozonation of Polymorphic MnO_2-Oxalic Acid Complexes, Submitted to Separation and Purification Technology (2025).

6.1 Introduction

Our previous study found that the addition of oxalic acid (OA) to the solution promoted the formation of the β-MnO_2-OA complex. This complex not only enhanced the k value of the β-MnO_2/OA/O_3 process for pCBA degradation (1.541 min^{-1}), which was four times higher than ozonation alone, but also achieved the co-degradation of pCBA (90.4%) and OA (65.2%). The generation of β-MnO_2-OA complex could improve the redox properties and the electron transfer ability of catalyst, while also enhance O_3 availability. However, other studies have reached different conclusions about the performance and mechanisms of MnO_2/acid system in the pollutants removal. For example, Wang et al. [1] reported that δ-MnO_2-OA complex could achieve effective methyl parathion (MP) degradation (67.83%). Initially, excess OA combined with Mn^{3+} generated by the reduction of δ-MnO_2 to form Mn^{3+}-OA complex. This Mn^{3+}-OA complex then combined with MP or its hydrolysis products to generate new active complexes. These new complexes acted as primary active species, reducing MP or its hydrolysis products. Sun et al. [2] constructed MnO_2/organic acid systems using MnO_2 colloid for tetracyclines (TC) degradation. The results showed that 62.5% of TC degradation in the OA system was due to the Mn^{3+}-oxalate complex, 90.7% of TC removal in L-tartaric acid system was due to the direct oxidization by Mn (Ⅲ).

To date, few studies have discussed the effects of OA as a complex agent on the catalytic ozonation of pollutants by MnO_2 with different crystal phases. Additionally, the catalytic efficiencies and mechanisms of various MnO_2-OA complexes have not been compared and concluded. Therefore, it is attractive to explore the complexity between different crystalline MnO_2 and OA and the HCO mechanism. In summary, the specific objectives of this study were: 1) to synthesize α-, β-, and δ-MnO_2 materials use for constructing MnO_2-OA complexes, 2) to compare the catalytic ozonation activity of MnO_2-OA complexes through atrazine (ATZ) degradation, 3) to analyze the influence of different MnO_2 structures and surface properties on the formation of MnO_2-OA complexes, 4) to quantify the ROS produced in the catalytic ozonation and evaluate the contribution for ATZ degradation, 5) to discuss and compare the catalytic ozonation mechanisms involving various MnO_2-OA complexes reaction.

6.2 Material and methods

6.2.1 Chemicals

All chemicals including ($KMnO_4$), (ATZ), (PP), (2,4-D), ($(NH_4)_2S_2O_8$), (TA), (TBA), (BQ), (MDE), ($Na_2S_2O_3$), ($MnSO_4$), ($C_2H_2O_4$), (NaOH), (NaN_3), acetonitrile, H_3PO_4, and HCl.

6.2.2 Preparation of catalysts

A modified hydrothermal-calcination method was used to synthesize α-MnO_2, β-MnO_2, and δ-MnO_2 catalysts. The precursor, hydrothermal temperature and hydrothermal duration are displayed in Table 6.1.

Table 6.1 Reagent and conditions for preparing different catalysts.

Catalyst	Precursor	Temperature	Duration
α-MnO_2	1.25 g $KMnO_4$ + 0.53 g $MnSO_4 \cdot H_2O$, 80 mL water	160ºC	14 h
β -MnO_2	3.38 g $MnSO_4 \cdot H_2O$ + 4.56 g $(NH_4)_2S_2O_8$, 80 mL water	90ºC	24 h
δ-MnO_2	1.50 g $KMnO_4$ + 0.28 g $MnSO_4 \cdot H_2O$, 80 mL water	160ºC	15 h

6.2.3 Characterization

The catalysts were characterized through the Fourier transform infrared (FT-IR) spectra, X-ray powder diffraction (XRD) patterns, the X-ray photoelectron spectra (XPS), scanning electron microscope (SEM), Brunauer-Emmett-Teller (BET) analysis, and the oxygen temperature programmed desorption (O_2-TPD).

6.2.4 Experiment procedure

6.2.4.1 Catalytic activity experiments

Batch ozonation experiments were conducted in a 250 mL glass beaker. Ozone stock solution was prepared in the same method as previous study [3]. Typically, a certain quantity of catalyst (α-/β-/δ-MnO_2) was added to a mixture of OA and ATZ solution, then, catalytic ozonation reaction was initiated by the addition of the O_3 stock solution with initial reaction concentration of 5 mg L^{-1}. Each experiment was conducted in at least duplicate.

6.2.4.2 The identification and quantification of ROS

In this study, TA, 2,4-D, and MDE as ROS probes, were introduced into the same catalytic ozonation system with ATZ and OA at low concentration (0.1 mg L^{-1}) to identify and calculate the contribution of ROS. Furthermore, the adsorption of the probes and ATZ on the surface of catalysts can be negligible. Therefore, the degradation of ATZ, 2,4-D, TA, and MDE in HCO system can be illustrated as Eqs. (6.1-6.4).

$$ln\left(\frac{[ATZ]_0}{[ATZ]_t}\right) = k_{\cdot OH,ATZ}\int[\cdot OH]\,dt + k_{O_2^{\cdot -},ATZ}\int[O_2^{\cdot -}]dt + k_{^1O_2,ATZ}\int[^1O_2]dt + k_{O_3,ATZ}\int[O_3]\,dt \tag{6.1}$$

$$ln\left(\frac{[TA]_0}{[TA]_t}\right) = k_{\cdot OH,TA}\int[\cdot OH]\,dt + k_{O_2^{\cdot -},TA}\int[O_2^{\cdot -}]dt + k_{^1O_2,TA}\int[^1O_2]dt + k_{O_3,TA}\int[O_3]\,dt \tag{6.2}$$

$$ln\left(\frac{[MDE]_0}{[MDE]_t}\right) = k_{\cdot OH,MDE}\int[\cdot OH]\,dt + k_{O_2^{\cdot -},MDE}\int[O_2^{\cdot -}]dt + k_{^1O_2,MDE}\int[^1O_2]dt + k_{O_3,MDE}\int[O_3]\,dt \tag{6.3}$$

$$ln\left(\frac{[2,4\text{-}D]_0}{[2,4\text{-}D]_t}\right) = k_{\cdot OH,2,4\text{-}D}\int[\cdot OH]\,dt + k_{O_2^{\cdot -},2,4\text{-}D}\int[O_2^{\cdot -}]dt + k_{^1O_2,2,4\text{-}D}\int[^1O_2]dt + k_{O_3,2,4\text{-}D}\int[O_3]\,dt \tag{6.4}$$

$$O_{3,exp} = \int[O_3]dt \tag{6.5}$$

$k_{O_3,compound}$, $k_{\cdot OH,compound}$, $k_{O_2^{\cdot -},compound}$, and $k_{^1O_2,compound}$ are the second-order rate constant for the reaction of probe compounds and ATZ with O_3, $^{\bullet}OH$, $O_2^{\bullet -}$, and $^1O_2$, respectively, which are listed in Table 6.2. O_3 exposure ($\int[O_3]dt$) was determined from the time integrated O_3 concentration during the treatment time Eq. (6.5). The exposures of $^{\bullet}OH$, $O_2^{\bullet -}$, and $^1O_2$ were calculated through Eqs.(6.2-6.4), which were displayed as $\int[{}^{\cdot}OH]\,dt$, $\int[O_2^{\cdot-}]dt$, and $\int[{}^1O_2]dt$, respectively, based on the observed abatement efficiency of IMD, 2,4-D, and MDE in the same HCO system.

Table 6.2 Second-order rate constants for the reaction of test micropollutants with O_3, $^{\cdot}OH$, $O_2^{\cdot-}$, and $^1O_2$.

Compounds	k_{O_3} **($M^{-1}s^{-1}$)**	$k_{^{\cdot}OH}$ **($M^{-1}s^{-1}$)**	$k_{O_2^{\cdot-}}$ **($M^{-1}s^{-1}$)**	$k_{^1O_2}$ **($M^{-1}s^{-1}$)**
TA	0.04	3.3×10^9	1.1×10^4	1.2×10^7
2,4-D	29.1	5.1×10^9	8.3×10^5	No·Reaction
MDE	<1	6×10^9	No·Reaction	1.5×10^8
ATZ	2.3	2.4×10^9	4.1×10^5	$<4\times10^4$

6.2.5 Analysis methods

ATZ degradation was analyzed by an Infinity 1260 HPLC from Agilent The concentrations of TA, 2,4-D, and MDE were separated by Vanquish HPLC-MS 137, equipping with Orbitrap IQ-X detector. The mobile phase gradient elution procedure and the detailed detective instrument information was displayed in Table 6.3.

Table 6.3 The mobile phase gradient elution procedure used for probes analysis

Mobile phase gradient elution procedure		
Time (min)	Mobile phase formic acid	Mobile phase acetonitrile
0.0	95	5
10	65	35
11	35	65
16	0	100
18	0	100
18.5	95	5
22	95	5

6.3 Results and discussion

6.3.1 The structural properties of various MnO_2

As shown in Fig.6.1(a), the XRD patterns of three as-prepared samples were analyzed. The diffraction peaks detected at 2θ values of 22.5º, 28.7º, 37.5º, 42.0º, 49.9º, 56.6º, 59.9º, 65.3º and 68.9º (PDF 44-0141) could be assigned to the (110), (200), (310), (211), (301), (411), (600), (521), (002), and (541) of α-MnO_2, indicating the existence of MnOx with a tetragonal structure [4]. Furthermore, weak and broad diffraction peaks of δ-MnO_2 were also observed at 2θ = 12.5º, 25.1º, 37.2º, and 65.5º corresponding to the (001), (002), (110), and (020) crystal planes [5]. The evident peaks at 28.6º, 37.3º, 40.9º, 42.8º, and 56.7º were related to the (110), (101), (111), (211), (220), and (301) crystal planes, respectively, representing the rutile structure of β-MnO_2 (PDF 81-2261) [6]. The XRD results clearly revealed the successful fabrication of multi-forms of MnO_2 crystallographic.

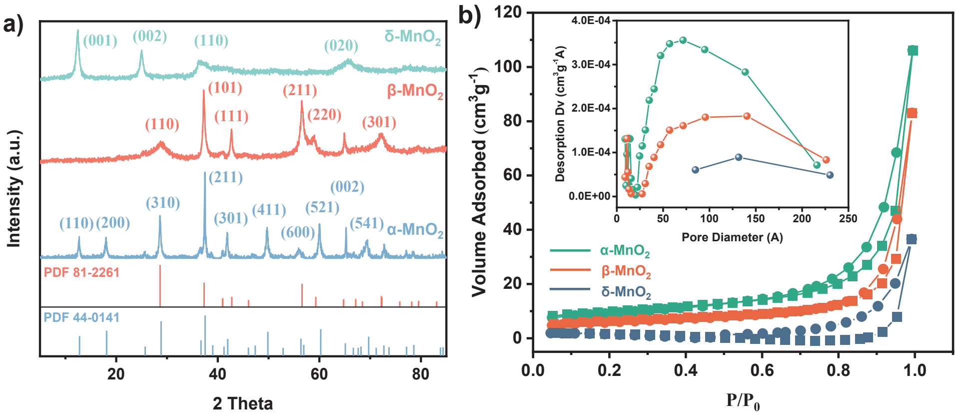

Fig.6.1 XRD patterns of different MnO_2 composites a) and N_2 adsorption/desorption isotherm b)

Fig.6.1(b) exhibited the N_2 adsorption-desorption isotherms of as-prepared MnO_2 samples. All three catalysts displayed a similar characteristic type IV adsorption curve with a hysteresis loop occurring at relative pressure (P/P_0) between 0.4 and 1.0, suggesting the presence of mesopores [7]. The specific surface areas, pore size distributions, and pore volumes were summarized in Table 6.4. Due to differences in morphological structure, the catalysts presented varying specific surface areas in the following order: δ-MnO_2 (6.2987 $m^2\,g^{-1}$) < β-MnO_2 (21.6721 $m^2\,g^{-1}$) < α-MnO_2 (33.2261 $m^2\,g^{-1}$). Moreover, the SEM images of the various crystal structures of catalysts were explored in Fig.6.2. α-MnO_2 existed a uniform shape of nanowires with the width of 50-70 nm and length of 0.5-3 μm [8]. β-MnO_2 had dandelion-like nanospheres with a diameter of 2-8 μm, which consisted of nanorods with the width of 40-60 nm on the surface. And δ-MnO_2 exhibited a flower-like sphere morphology consisting of nanoflakes.

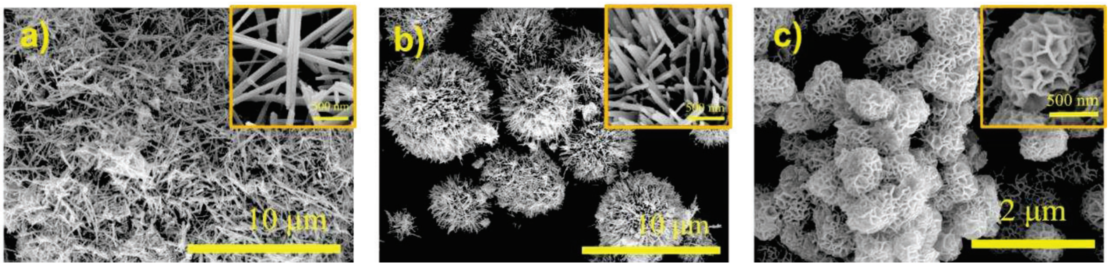

Fig.6.2 SEM images of α-MnO_2 a), β-MnO_2 b), and δ-MnO_2 c).

Table 6.4 Summarization of BET surface areas, pore volumes, and average pores for preparing different catalysts.

Catalyst	BET surface area ($m^2 \cdot g^{-1}$)	Total pore volume ($cm^3 \cdot g^{-1}$)	Average pore diameter (nm)
α-MnO_2	33.2261	0.0744	8.9530
β-MnO_2	21.6721	0.0443	8.1873
δ-MnO_2	6.2987	0.0092	5.8529

The FT-IR analysis was conducted in Fig.6.3(a) with the range between 400 and 4000 cm^{-1}. Same peaks of three samples appeared at 530 cm^{-1} and 462 cm^{-1} could be indexed to the vibrations of Mn-O bonds [9] and the absorption band at 712 cm^{-1} was ascribed to the Mn-O-Mn stretching vibration, indicating the successful formation of octahedral [MnO_6] [10]. Several small peaks in the range of 1000-1500 cm^{-1} for the three composites could be attributed to the bending vibrations of hydroxyl (−OH) groups bonded to Mn atoms [11, 12]. In the case of δ-MnO_2, a broad peak at 3400 cm^{-1} were associated with O−H bonds stretching vibrations originating from water adsorbed on the catalyst surface [12]. Furthermore, a strong intensity band at 1114

cm^{-1} was clearly observed for β-MnO_2, which was usually appeared in low temperature hydrothermal preparation of nanostructured materials [13].

The O_2-TPD experiments were operated to explore the mobility of oxygen species (Fig.6.3(b)). The desorption peaks below 300°C correspond to the surface-adsorbed oxygen species (O_S). The second desorption peaks, observed in 300-500°C range, could be attributed to subsurface lattice oxygen (O_{SL}), which is associated with the reduction of Mn^{4+} to Mn^{3+}. While the third peaks, occurring above 500°C, are linked to the release of lattice oxygen (O_L) [14, 15]. Compared to α-MnO_2 and β-MnO_2, larger desorption peak of O_S was found over δ-MnO_2 (172 °C). It means that more active oxygen species were detected on the surface of catalyst. As the generation, activation, and migration of reactive Os typically relied on oxygen vacancies (Vo), the result suggested that δ-MnO_2 contained highest activity of mobile oxygen and largest amount of Vo [15, 16].

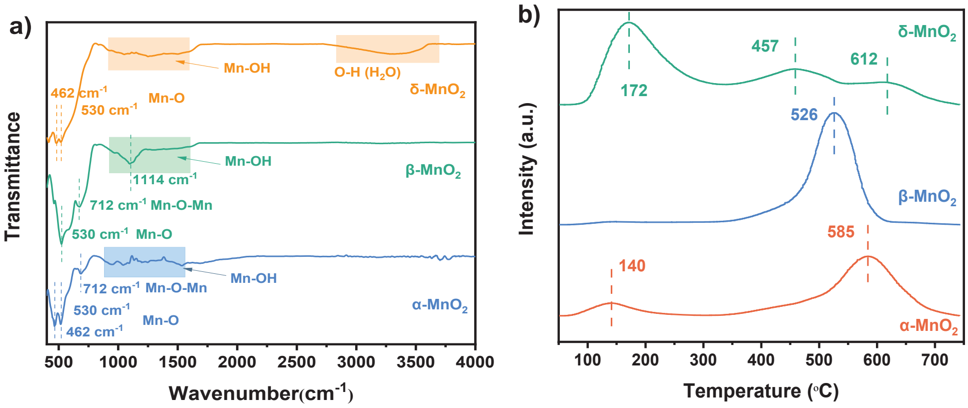

Fig.6.3 FT-IR spectrum a) and O_2-TPD profiles b) of α-MnO_2, β-MnO_2, and δ-MnO_2.

XPS spectrum was used for determining the surface chemical element states of α-/β-/δ-MnO_2 materials. Based on Fig.6.4(a), the investigated scan spectrum suggests that catalysts consist mainly of Mn and O. After calibrating the binding energies, The C 1s spectrum (Fig.6.4(b)) was divided into three peaks at ~288.4, ~284.7, and ~285.6 eV, which could be ascribed to C−C/C=C/C−H, O−C=O, and C−O bonds, respectively [17]. For the O 1s spectra in Fig.6.4(c), the peak at lower binding energy (< 530.3 eV) could be corresponding to lattice oxygen (O_I: O_2^-), and the peak at 530.0~531.8 eV (donated O_{II}) could be assigned to the adsorbed oxygen (O_2^{2-}, O^{2-}, O^-) and -OH groups [18, 4, 15]. As presented Table 2, the O_{II}/O_I ratio of δ-MnO_2 (0.38) was higher than that of α-MnO_2 (0.20) and β-MnO_2 (0.32), indicating δ-MnO_2 had most abundant surface adsorbed oxygen due to the presence of Vo on the catalyst surface [19]. Moreover, the Mn 2p$_{3/2}$ signal (Fig.6.4(d)) fitting for catalysts could be deconvoluted into three peaks with binding energy at ~641.9, 643.4, and 645.3 eV attributed to Mn^{3+}, Mn^{4+}, and Mn^{2+}, respectively [20]. δ-MnO$_2$ showed the highest (1.57) Mn^{3+}/Mn^{4+} ratio whereas β-MnO$_2$ exhibited the lowest (0.54) (Table 6.5). The existence of Mn^{3+} in the MnO$_2$ catalyst would produce Vo to maintain electrostatic balance [5]. In general, compared to α-MnO$_2$ and β-MnO$_2$, δ-MnO$_2$ had the highest amount of Mn^{3+} and Vo, which could enhance the adsorption of O$_3$ on catalyst surface and then decompose into more ROS.

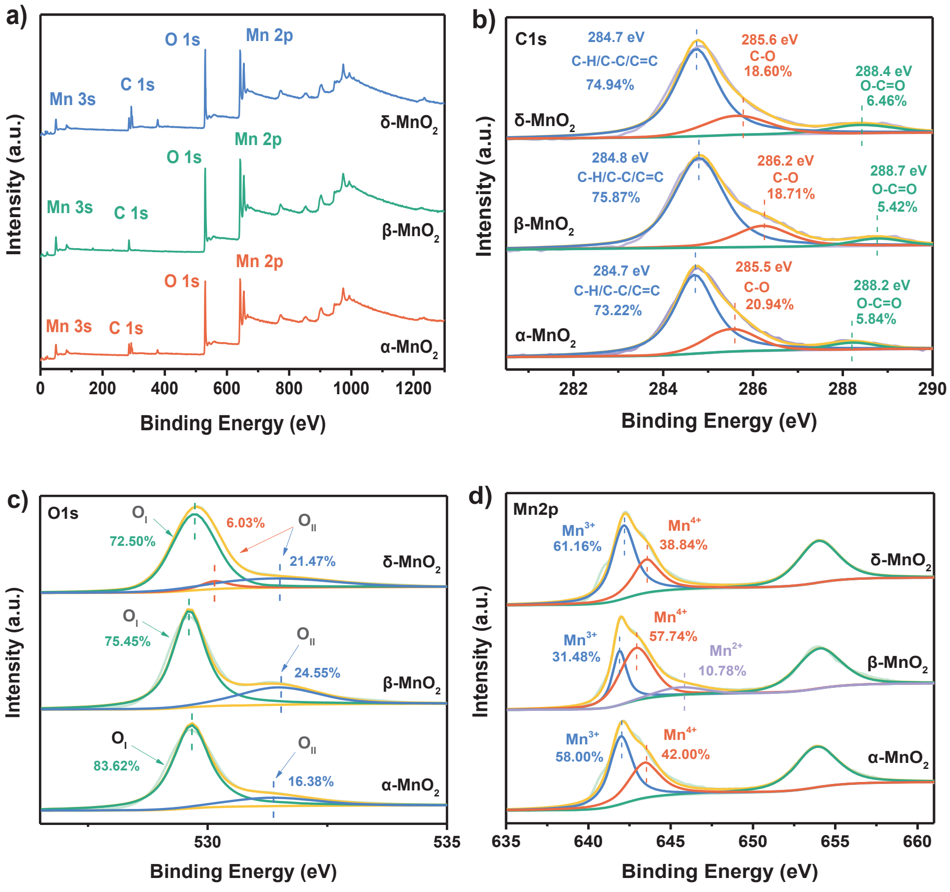

Fig.6.4 XPS spectrum for α-MnO$_2$, β-MnO$_2$, and δ-MnO$_2$ composites: survey spectra a), C 1s b), O 1s c), and Mn 2p d).

Table 6.5 XPS results of different catalysts

Catalyst	O 1s									Mn 2p
	O_I		O_{II}				O_{III}		O_{II}/O_I	Mn^{3+}/Mn^{4+}
			-OH groups, O_2^{2-}, O^-, O^{2-}							
	Peak (eV)	Area (%)	Peak (eV)	Area (%)	Peak (eV)	Area (%)	Peak (eV)	Area (%)	ratio	ratio
α-MnO_2	529.7	83.62			531.3	16.38			0.20	1.38
β-MnO_2	529.6	75.45			531.5	24.55			0.32	0.54
δ-MnO_2	529.7	72.50	530.2	6.03	531.4	21.47			0.38	1.58
α-MnO_2-OA	529.6	55.96	530.2	15.92	531.5	28.12			0.79	1.52
β-MnO_2-OA	529.3	60.96			531.0	19.83	532.4	21.21	0.33	1.65
δ-MnO_2-OA	529.8	58.69	530.3	16.19			532.3	25.12	0.28	1.60

6.3.2 Enhanced catalytic ozonation mediated by MnO_2-OA complexes

As described in Fig.6.5(a), the ATZ removal in sole O_3 was 44.33% and it was slightly inhibited in the β-MnO_2/O_3 (40.24%) and α-MnO_2/O_3 (41.45%) processes. Otherwise, the existence of δ-MnO_2 enhanced the ATZ degradation (60.73%) and corresponding rate constant (*k*) over 1 min increased to 0.93 min^{-1}. δ-MnO_2 exhibited the highest Vo amount and mobile oxygen species activity, which could improve O_3 adsorption and decomposition to generate more ROS, thus facilitating the degradation of ATZ. Previous study has confirmed that a complex can form between OA and MnO_2, enhancing the catalytic ozonation efficiency. To explore the influence of OA on complex formation with various MnO_2, the degradation of ATZ in α-MnO_2/OA/O_3, β-MnO_2/OA/O_3, and δ-MnO_2/OA/O_3 systems was compared. As described in Fig.6.5(b), the introduction of OA (10 mg L^{-1}) markedly promoted the ATZ elimination in three systems, achieving removal rates of 78.61%, 84.47%, and 69.87%, respectively. And the surface adsorption of ATZ (<2%) (Fig.6.5(c)) and OA (<5%) (not exhibited) by the complexes can be negligible. Meanwhile, Fig.6.5(d) revealed the rate of O_3 depletion, which was distinctively enhanced by α-MnO_2/OA/O_3 (39.60%), β-MnO_2/OA/O_3 (77.24%), and δ-MnO_2/OA/O_3 (59.04%). This suggested that the formed α-MnO_2-OA, β-MnO_2-OA, and δ-MnO_2-OA complexes improved the effective utilization of O_3, thereby producing more active substances to enhance the elimination of ATZ in the system.

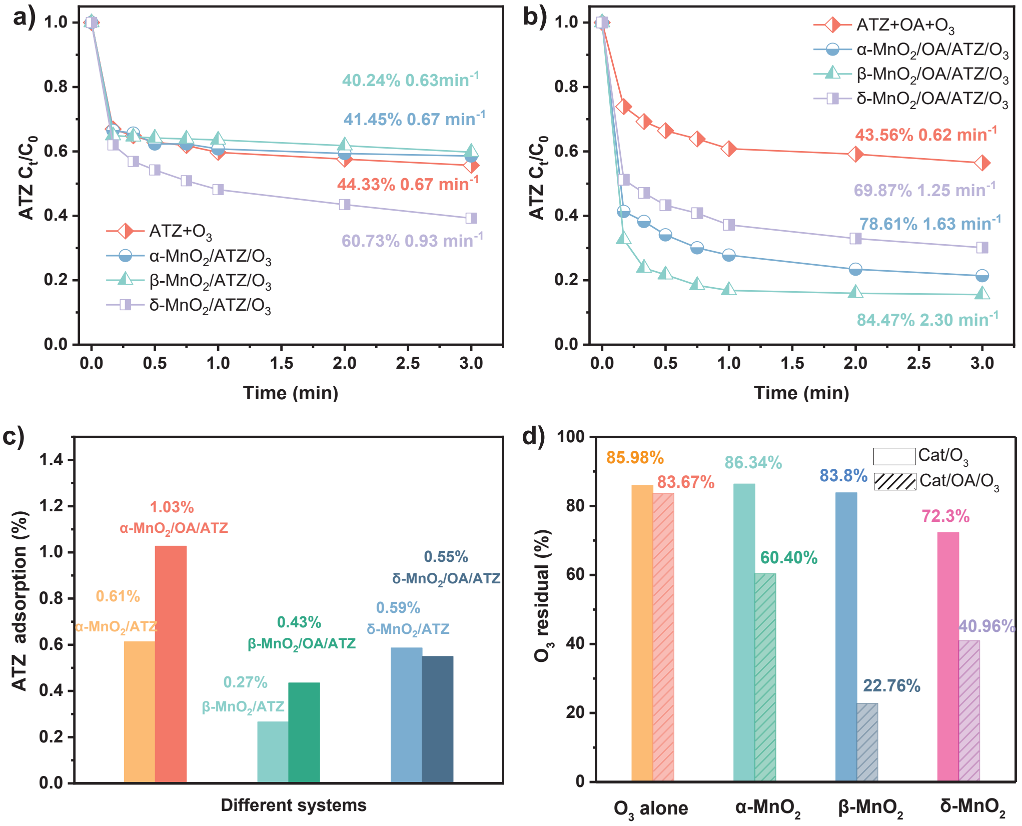

Fig.6.5 ATZ removal efficiency in different Cat/O_3 systems a), Cat/OA/O_3 systems b), catalyst alone c), and depletion of O_3 in different processes d). Experimental conditions: $[ATZ]_0$=5 mg L^{-1}, [Cat]=50 mg L^{-1}, $[OA]_0$=10 mg L^{-1}, $[O_3]_0$=5 mg L^{-1}, pH_0=4.0 ± 0.2.

To clarify the effect of complexation between OA and MnO_2 on the catalytic ozonation system, the removal efficiency of ATZ under various molar ratios of catalyst to OA was assessed in Fig.6.6. As shown in Fig.6.6(a), the ATZ degradation at molar ratios of α-MnO_2 to OA from 1:0.04 to 1:0.8 was 44.35%, 59.07%, 78.61%, 88.27%, and 95.09% after 3 min reaction. Similar removal trends were observed in β-MnO_2/OA/O_3, when molar ratios rose to 1:0.8, the degradation of ATZ was gradually promoted from 59.96% to 93.43% (Fig.6.6(b)). The introduction of OA would promote the rapid formation of α-MnO_2-OA and β-MnO_2-OA complexes, which affected the removal of ATZ. As for δ-MnO_2/OA/O_3 process displayed in Fig.6.6(c), δ-MnO_2 catalytic ozonation achieved 60.73% of ATZ degradation, while it was reduced slightly at molar ratio of 1:0.04 (40.63%) and 1:0.1 (46.35%). The inhibition was owing to the competition between ATZ and OA for the ROS and O_3. However, when the ratio of OA grew continuously up to 1:0.8, the elimination of ATZ increased to 96.71%. The generation of δ-MnO_2-OA complex depended on the content of OA. Moderately increasing the OA dose would enhance formation of α-MnO_2-OA, β-MnO_2-OA, and δ-MnO_2-OA complexes, which might generate more ROS through strengthening reaction with O_3, thereby boosting the catalytic ozonation performance.

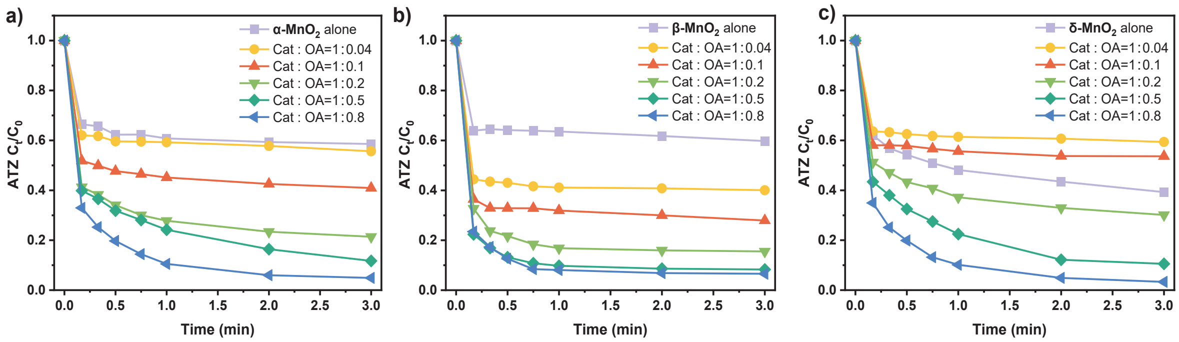

Fig.6.6 The effects of molar ratios (1:0.04-1:0.8) of α-MnO_2 to OA a), β-MnO_2 to OA b), and δ-MnO_2 to OA c) on ATZ removal efficiency in catalytic ozonation systems. Experimental conditions: $[ATZ]_0$=5 mg L^{-1}, [Cat]=50 mg L^{-1}, $[OA]_0$=2-40 mg L^{-1}, $[O_3]_0$=5 mg L^{-1}, pH_0=4.0 ± 0.2.

Furthermore, the potential of Cat/OA/O_3 system for practical application, the recycling experiments were conducted using α-MnO_2, β-MnO_2, and δ-MnO_2 catalysts with the molar ratio of 1:0.8. The used catalysts were separated, washed 4 times with Mili-Q water, dried at 60ºC for 12 h, and reused in subsequent experiments. As shown in Fig.6.7, the degradation efficiency of ATZ remained around 90% even after the 4th cycle. However, the observed pseudo-first-order rate constant (k_{obs}) values for the α-MnO_2/OA/O_3, β-MnO_2/OA/O_3, and δ-MnO_2/OA/O_3 processes decreased from 1.32 to 1.04 min^{-1}, 1.33 to 0.84 min^{-1}, and 1.44 to 1.25 min^{-1}, respectively.

To assess the impact of metal ion in the solution, the release of Mn ion was monitored during ozonation to further access the reusability of catalysts. Low Mn ion release (< 0.4 mg L^{-1}) was detected in all three processes after the first reaction. By the end of the cycles, the Mn ion concentration in the solution increased to approximately 2.62 mg L^{-1}, 2.58 mg L^{-1}, and 3.27 mg L^{-1} in α-MnO_2/OA/O_3, β-MnO_2/OA/O_3, and δ-MnO_2/OA/O_3 processes, respectively. The increased dissolution of Mn ions likely reduced the active Mn species on the catalyst surface, affecting the formation of the MnO_2-OA complex and subsequently inhibiting its reaction rate. Additionally, it has been reported that the deposition of reaction intermediates on the catalyst surface, blocking active sites [21], could also contribute to the decline in the corresponding k_{obs} values. On the other hand, Graham et al [22] reported that the introduction of a small amount of Mn^{2+} in O_3/Mn^{2+} oxidation process can directly promote the decomposition of O_3, generating •OH. Therefore, the increase in the dissolved amount of Mn ions in the Cat/OA/O_3 system could promote the generation of •OH, which might be one of the reasons why the degradation of ATZ remains around 90% after four cycles.

To further study the stability of the catalysts, the phase structure of reacted α-MnO_2, β-MnO_2, and δ-MnO_2 were examined by XRD. As illustrated in Fig.6.8, the baseline of spectrum shifts upward due to the dissolution Mn ions. Additionally, the crystal planes (110), (200), (310), (211), (301), (411), (600), (521), (002), and (541) observed in the reacted α-MnO_2 spectrum, as well as the peaks corresponding to (110), (101), (111), (211), (220), and (301) in the reacted β-MnO_2 spectrum, and the (001), (002), (110), and (020) crystal planes in the reacted δ-MnO_2 spectrum, were the same characteristic peaks as those in original α-MnO_2, β-MnO_2, and δ-MnO_2 catalysts (Fig.6.1). These results demonstrated the structural stability of the catalysts. The reusability tests of the α-MnO_2, β-MnO_2, and δ-MnO_2 catalysts provided new insights into the application of Cat/OA/O_3 system for water purification.

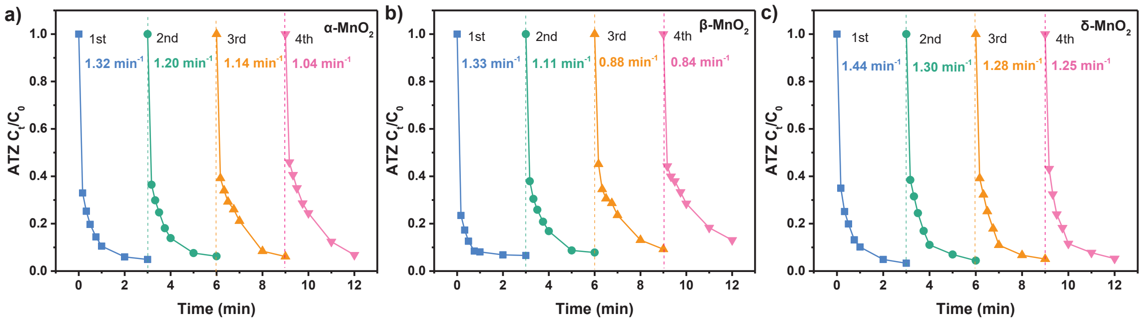

Fig.6.7 The recycling experiments of α-MnO_2 a), β-MnO_2 b), and δ-MnO_2 c). Experimental conditions: Experimental conditions: $[ATZ]_0$=5 mg L^{-1}, [Cat]=50 mg L^{-1}, $[OA]_0$=40 mg L^{-1}, $[O_3]_0$=5 mg L^{-1}, pH_0=4.0 ± 0.2.

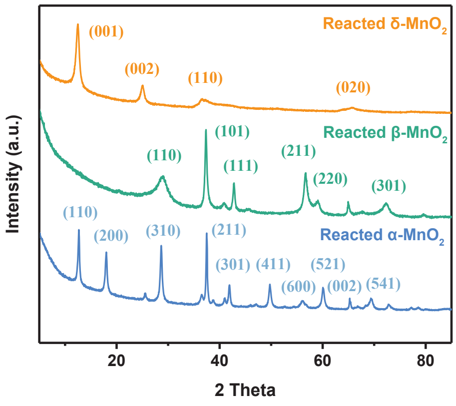

Fig.6.8 XRD patterns of different MnO_2 composites after reaction in Cat/OA/O_3 system.

Considering the conditions for complex generation, the influence of various pH values was explored in Fig.6.9. With the increase of pH value from 3.0 to 7.0, the catalytic ozonation removal of ATZ was no significant changes in the presence of only catalyst (α-MnO_2 or β-MnO_2), remaining around 43% (Fig.6.9(a)). In the case of δ-MnO_2, the removal efficiency of ATZ was reduced from 63.27% to 48.29%, which was related to the charge of catalyst surface and O_3 utilization efficiency [23]. As compared in Fig.6.9(b), more than 95% of ATZ was degraded within 3 min by the formed complexes at pH 3.0. Subsequently, the catalytic ozonation activities of three complexes were obviously restrained (<40%) as pH increased to 7.0. These results were primarily attributed to the increased solubility of MnO_2 in OA at acidic pH, which promoted the production of Mn^{3+}. Furthermore, Mn^{3+} complex formed with OA exhibited greater stability and enhanced catalytic ozonation activity under acidic conditions, while its effectiveness decreased under alkaline pH conditions [24].

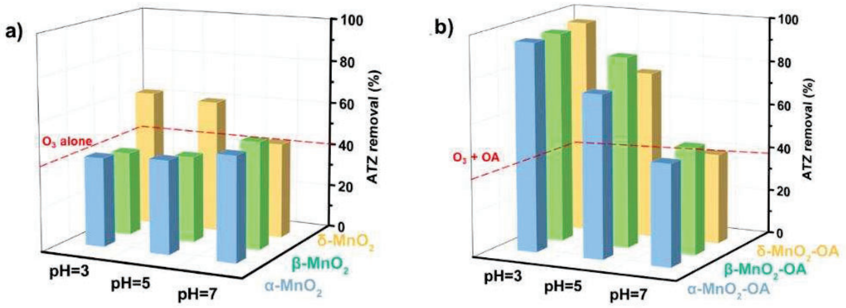

Fig.6.9 The effects of pH values of solution on ATZ removal in different Cat/O_3 systems a), and Cat/OA/O_3 systems. Experimental conditions: $[ATZ]_0$=5 mg L^{-1}, [Cat]=50 mg L^{-1}, $[OA]_0$=40 mg L^{-1}, $[O_3]_0$=5 mg L^{-1}, pH_0=3.0~7.0.

6.3.3 Characterizations of MnO_2-OA complexes

The addition of OA in the solution accelerated the formation of MnO_2-OA complex, which impacted the catalytic ozonation performance. To compare the chemical composition, surface properties, and structures of the formed α-MnO_2-OA, β-MnO_2-OA, and δ-MnO_2-OA complexes, the O_2-TPD, FT-IR, and XPS characterizations were further conducted.

In FT-IR spectrum (Fig.6.10(a)), several high-frequency modes of three samples below 750 cm^{-1} represented the vibrations of Mn-O-Mn and Mn-O bonds, illustrating that the newly formed complexes had not altered the fundamental unit structure of

MnO_2 [25]. But the peak intensity decreased signifying the weakened Mn-O bonds. Compared to the initial MnO_2 catalysts (Fig.6.3(a)), the peaks in the range of 1000-1500 cm^{-1} were weaken in the spectra of α-MnO_2-OA complex. Moreover, the peak at 1114 cm^{-1} had completely disappeared in the case of β-MnO_2-OA complex. The results indicated that complexation of OA with α-MnO_2/β-MnO_2 occurred by replacing some -OH groups on the catalysts (α-and β-MnO_2) surface [26, 27]. However, peaks in the 1000-1500 cm^{-1} range as well as a broad peak around 3400 cm^{-1} were still observed in spectra of δ-MnO_2-OA complex. This implied that -OH groups remained and an amount of H_2O was adsorbed on the catalyst surface after δ-MnO_2 complexation with OA [11].

The analysis of O_2-TPD spectra was shown in Fig.6.10(b). In the comparison with α-MnO_2 (Fig.6.3(b)), a desorption peaks of α-MnO_2-OA complex shifted from 140ºC to 130ºC (O_S). Theoretically, O_S as labile oxygen, the lower the temperature of O_S release was, the looser they had been adsorbed on the catalyst surface, which indicated more Vo existed in the catalyst [27]. In the spectra of β-MnO_2-OA complex, the peak of O_L moved towards a lower temperature (514ºC) from 526ºC (Fig.6.3(b)), implying the lattice oxygen in the framework had become more unstable [28]. This phenomenon was explained by increased Mn vacancies (V_{Mn}), which weakened Mn-O bonds in the crystal framework and thus enhanced lattice oxygen mobility [15, 29]. Moreover, upon forming δ-MnO_2-OA complex, the peak intensity of O_S (149ºC) decreased, while those of O_{SL} (447ºC) and O_L (512ºC) increased, indicating a substantial rise in O_L content [16]. Meanwhile, the O_L shifted sharply from 612ºC to 512ºC, suggesting a notable enhancement in O_L activity within δ-MnO_2-OA complex.

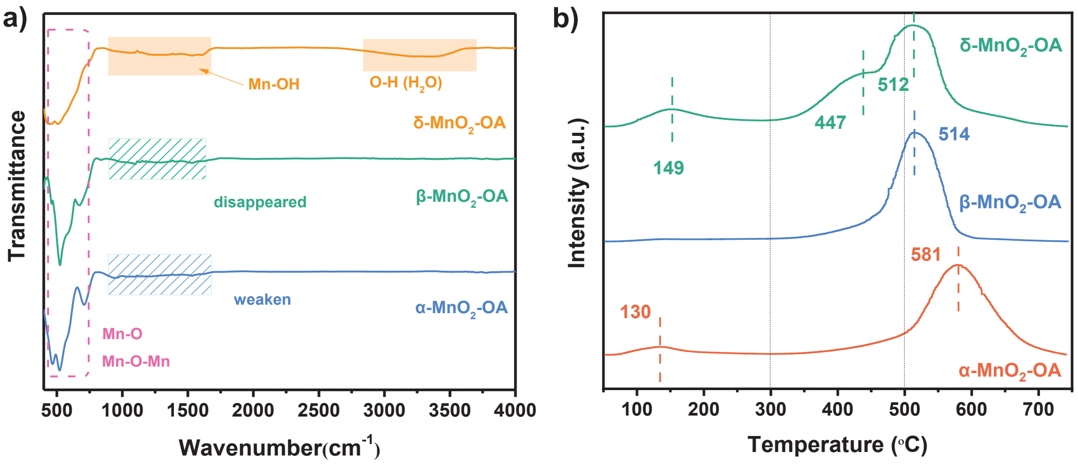

Fig.6.10 FT-IR spectrum a) and O_2-TPD profiles b) of α-MnO_2-OA, β-MnO_2-OA, and δ-MnO_2-OA complex.

The complete XPS survey spectrum of complex was revealed in Fig.6.11(a), it was observed that the peak intensity of C1s in β-MnO_2-OA complex has increased significantly, suggesting a stronger combination ability between β-MnO_2 and OA.

Meanwhile, the O−C=O and C−O ratios of β-MnO_2-OA complex increased from 5.42% to 5.64% and from 18.71% to 23.70%, respectively (Fig.6.11(b)).

In the O 1s signals of α-MnO_2-OA, β-MnO_2-OA, and δ-MnO_2-OA complexes, binding energy of peak above 532.0 eV could be associated with adsorbed molecular water (O_{III}) [18]. As shown in Fig.6.11(c) and Table 6.4, the O_I peak of three complexes decreased compared to original MnO_2, which confirmed the weakened Mn-O bonds during the formation process of complex. Moreover, in the case of α-MnO_2-OA complex, two peaks at 530.2 and 531.5 eV could be assigned to O_{II}, which intensity rose to 15.92% and 28.12%, respectively. The improved O_{II}/O_I ratio (0.79) indicated the generation of more Vo during the combination of α-MnO_2 and OA [17]. For β-MnO_2-OA complex, O_{II} peak (531.0 eV) decreased from 24.55% to 19.83% further verifying the substitution of surface -OH groups. Due to the weakened Mn-O bonds of β-MnO_2-OA complex, Mn−O coordination configuration changed, which could induce the formation of V_{Mn}, thus enhancing the adsorption of O_3 and water molecules (H_2O) on the catalyst surface [15]. That could be the reason for the appearance of peak at 532.4 eV (21.21%). In terms of δ-MnO_2-OA complex, the peak at 530.3 eV increased markedly from 6.03% to 16.19%, implying the creation of a large amount of surface -OH [26]. However, the O_{II}/O_I ratio of δ-MnO_2-OA complex decreased from 0.38 to 0.28, indicating that the formation of the complex did not lead to an increase in Vo.

The Mn $2p_{3/2}$ spectra of α-MnO_2-OA complex in Fig.6.11(d) was deconvoluted into two peaks assigned to Mn^{3+} (642.0 eV) and Mn^{4+} (643.05 eV) [18]. It was noted that the Mn^{3+}/Mn^{4+} ratio (1.52) was more than that of pristine α-MnO_2 (1.38) (Table 6.4), suggesting the much larger content of Mn^{3+} on the surface of complexation catalyst, which could promote the formation of surface Vo over α-MnO_2-OA complex to preserver charge balance [21]. Three peaks were found in Mn $2p_{3/2}$ spectra of β-MnO_2-OA complex at 641.6 (Mn^{3+}), 642.8 (Mn^{4+}), and 644.5 eV (Mn^{2+}) [20]. The percentage of Mn^{4+} decreased and that of Mn^{3+} and Mn^{2+} increased. During the complexation process, Mn^{4+} in the frameworks was progressively reduced to Mn^{3+} and subsequently to Mn^{2+}, with its two 3s electrons being transferred to Mn–O orbitals [30]. This reduction led to an increase in V_{Mn} and Mn^{3+}/Mn^{4+} ratio (1.65) [15]. Besides, the relative Mn^{3+}/Mn^{4+} ratio of δ-MnO_2-OA complex was not distinctly change (1.60), suggesting the excellent stability of catalyst in the combination process with OA [31].

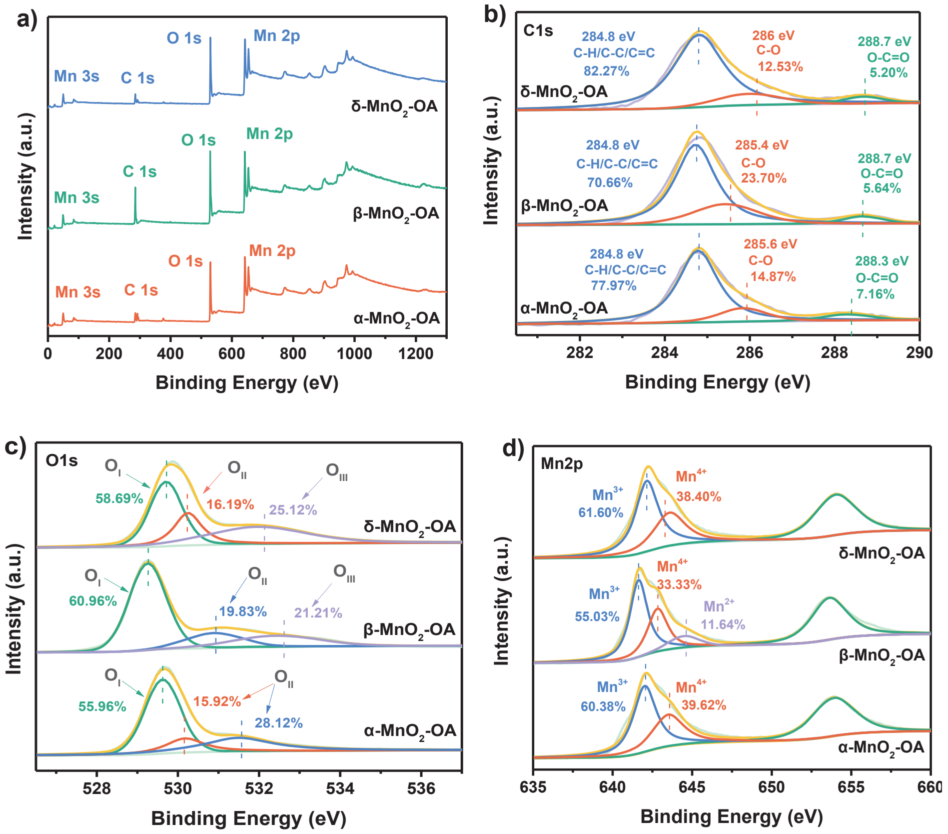

Fig.6.11 XPS spectrum for α-MnO2-OA, β-MnO2-OA, and δ-MnO2-OA complexes: survey spectra a), C 1s b), O 1s c), and Mn 2p d).

6.3.4 Identification of reactive species

6.3.4.1 Role of Mn^{3+} species

Based on the XPS analysis, after forming complexes by adding OA into the solution, the amount of Mn^{3+} of α-MnO2-OA, β-MnO2-OA, and δ-MnO2-OA complexes increased. To investigate the role of Mn^{3+} during the process of complexation, pyrophosphate (PP) was added into catalytic ozonation systems, which could be a scavenger of Mn^{3+} (log k$_{apparent}$ = 31.35). As exhibited in Fig.6.12, the ATZ (5 mg L^{-1}) degradation efficiencies of α-MnO2/OA/O3, β-MnO2/OA/O3, and δ-MnO2/OA/O3 systems were restrained by 64.46%, 49.64%, and 57.70%, respectively, with 0.5 mM of PP concentration. PP could complex with Mn^{3+} that would inhibit the complexation between MnO2 and OA. The reduction of complexes limited further reactions with O3, resulting in less ROS production, thus, hindering the degradation of ATZ. These findings indicated that the formations of α-MnO2-OA, β-MnO2-OA, and δ-MnO2-OA complexes depended on the presence of Mn^{3+} in the system.

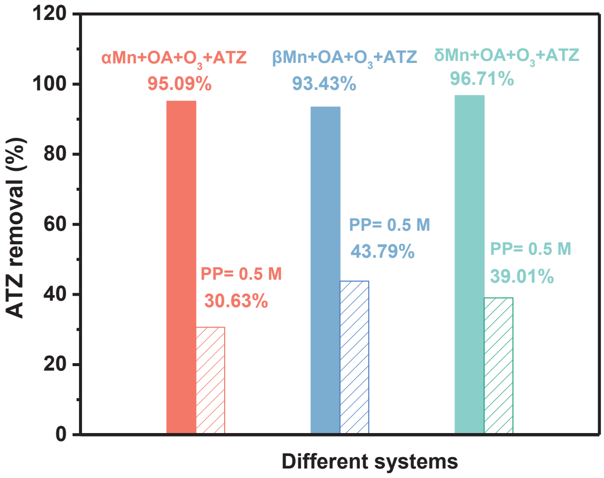

Fig.6.12 Effects of sodium pyrophosphate on ATZ removal efficiency. Experimental conditions: $[ATZ]_0$=5 mg L^{-1}, [Cat]=50 mg L^{-1}, [OA]=40 mg L^{-1}, $[O_3]_0$=5 mg L^{-1}, $[PP]_0$=0.5 mM.

6.3.4.2 Roles of ROS via scavenger experiments

Compared to O_3 alone (44.33%), α-MnO_2/O_3 (41.45%), and β-MnO_2/O_3 (40.24%), δ-MnO_2/O_3 process achieved the highest performance (60.73%) for ATZ degradation. In this study, 1 mM of TBA, *p*-BQ, and NaN_3 were introduced to catalytic ozonation system as the quenchers of $^{\bullet}OH$, $O_2^{\bullet-}$, and $^1O_2$, respectively. As shown in Fig.6.13, the degradation of ATZ was inhibited by the presence of TBA (31.41%), *p*-BQ (7.02%), and NaN_3 (5.17%) in the δ-MnO_2/O_3 system. Considering that TBA as scavenger could quench $^{\bullet}OH$ in bulk liquid phase ($^{\bullet}OH_L$), methanol (1 mM) was used to further evaluate the role of both $^{\bullet}OH_L$ and surface-bound $^{\bullet}OH$ ($^{\bullet}OH_S$) in ATZ degradation [32]. It was found that the ATZ removal in the existence of methanol (31.12%) was similar to that in the presence of TBA. The results implied that the degradation of ATZ in δ-MnO_2/O_3 process relied on the presence of $^{\bullet}OH$, $O_2^{\bullet-}$, and $^1O_2$.

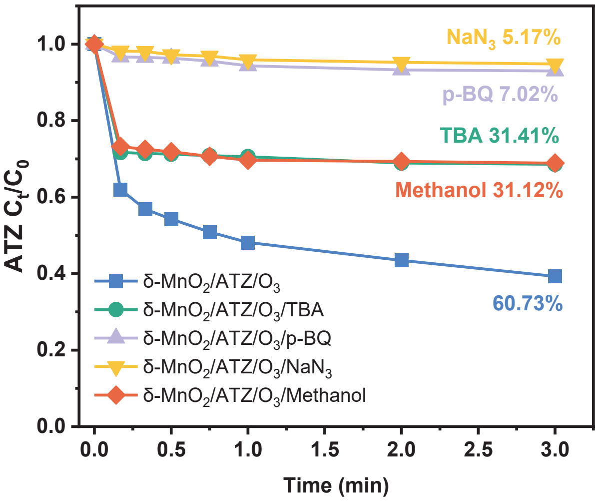

Fig.6.13 Effects of various scavengers on ATZ removal efficiency in δ-MnO_2/O_3 systems. Experimental conditions: $[ATZ]_0$=5 mg L^{-1}, [Cat]=50 mg L^{-1}, [OA]=40 mg L^{-1}, $[O_3]_0$=5 mg L^{-1}, [TBA]=[*p*-BQ]=[NaN_3]=[Methanol]=1 mM.

As investigated in Fig.6.14(a-c), the addition of TBA in α-MnO_2/OA/O_3, β-MnO_2/OA/O_3, and δ-MnO_2/OA/O_3 systems inhibited ATZ removal by less than 5%. For comparison, the presence of methanol could hinder ATZ degradation by more than 20%, which indicated that $^{\bullet}OH_S$ participated in the reaction improving catalytic efficiency. Furthermore, the presence of *p*-BQ, and NaN_3 almost restrained the degradation of ATZ in catalytic ozonation system. It suggested that both $O_2^{\bullet-}$, and $^1O_2$ were also important ROS in the process. However, as illustrated in Fig.6.15, when the scavengers were added into O_3 alone process, the ATZ elimination was significantly suppressed. In particular, more than 20% of ATZ degradation was inhibited by *p*-BQ and NaN_3. Guo et al pointed out that conventional radical scavengers with high concentrations can significantly interfere with O_3 decomposition and the chain reaction involving free radicals, making it challenging to accurately assess the contribution of ROS to catalytic ozonation efficiency [33]. Therefore, a probe approach was employed in the study to measure the exposures of various ROS in the reaction.

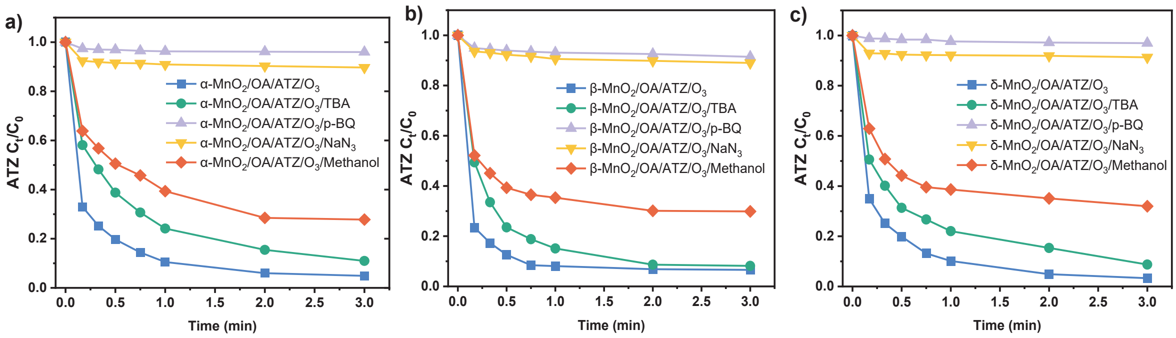

Fig.6.14 Effects of various scavengers on ATZ removal efficiency in α-MnO$_2$/OA/O$_3$ a), β-MnO$_2$/OA/O$_3$ b), and δ-MnO$_2$/OA/O$_3$ c) systems. Experimental conditions: $[ATZ]_0$=5 mg L^{-1}, [Cat]=50 mg L^{-1}, [OA]=40 mg L^{-1}, $[O_3]_0$=5 mg L^{-1}, [TBA]=[p-BQ]=[NaN$_3$]=[Methanol]=1 mM.

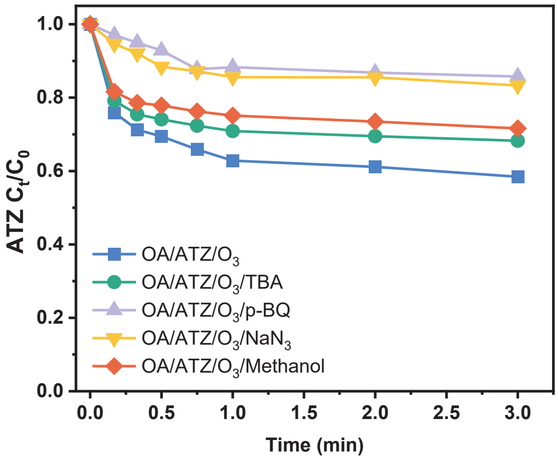

Fig.6.15 Effects of scavengers on ATZ removal efficiency in OA/ATZ/O3 process. Experimental conditions: [ATZ]0=5 mg L−1, [OA]=40 mg L−1, [O3]0=5 mg L−1, [TBA]=[p-BQ]=[NaN3]=[Methanol]=1 mM.

6.3.4.3 Quantification of ROS via low concentration probe experiments

As shown in Fig.6.16, the addition of trace amounts of probes (2,4-D, TA, and MDE) with concentration of 0.1 mg L^{-1} had little effect on the efficiency of O$_3$ alone (around 43%) and catalytic ozonation (>93%). According to the second-order rate constants of probe compounds and ATZ with O$_3$ and other ROS (Table 6.6), the exposure of O$_3$ and different ROS were calculated by using Eqs.(6.1-6.5). As shown in Fig.6.17, the O$_3$ exposure of β-MnO$_2$/OA/O$_3$ system was about 0.0055 Ms in 3 min, which was twice that of α-MnO$_2$/OA/O$_3$ and δ-MnO$_2$/OA/O$_3$ processes. The higher exposure level of O$_3$ in the β-MnO$_2$/OA/O$_3$ system provided an explanation for the faster catalytic reaction rate of the β-MnO$_2$-OA complex. Meanwhile, as displayed in

Fig.6.18, all three systems detected the presence of $^{\bullet}OH$, $O_2^{\bullet-}$, and $^1O_2$, but they exhibited different exposure rates. It was evident that the $^{\bullet}OH$ exposure level of α-MnO_2/OA/O_3 within 1 min (8.24×10^{-11} Ms) was higher than other systems, implying the more important role of $^{\bullet}OH$ in α-MnO_2/OA/O_3. As for the $O_2^{\bullet-}$, and $^1O_2$, β-MnO_2/OA/O_3 system presented the highest exposure rate in 1 min. In order to further investigate the roles of various ROS and O_3 in different catalytic ozonation processes, the contribution rates were simulated through Eqs.(6.6-6.8). Based on the results illustrated in Fig.6.18(d), it was found that the contribution rate of $^{\bullet}OH$ in α-MnO_2/OA/O_3 system was reach ~31%, which was higher than that of β-MnO_2/OA/O_3 (~22%) and δ-MnO_2/OA/O_3 (~24%) processes, further verifying the significant effect of $^{\bullet}OH$. Interestingly, the contribution column chart of O_3 and ROS also indicated that $^{\bullet}OH$ and $O_2^{\bullet-}$ were the dominant ROS responsible for ATZ removal, rather than $^1O_2$, which differed from the conclusion of the scavenger experiments.

$$f_{O_3,ATZ} = \frac{k_{O_3,ATZ}\int[O_3]\,dt}{k_{O_3,ATZ}\int[O_3]\,dt + k_{O_2^{\cdot-},ATZ}\int[O_2^{\cdot-}]dt \;+\; k_{^1O_2,ATZ}\int[^1O_2]dt} \tag{6.6}$$

$$f_{O_2^{\cdot-},ATZ} = \frac{k_{O_2^{\cdot-},ATZ}\int[O_2^{\cdot-}]dt}{k_{O_3,ATZ}\int[O_3]\,dt + k_{O_2^{\cdot-},ATZ}\int[O_2^{\cdot-}]dt \;+\; k_{^1O_2,ATZ}\int[^1O_2]dt} \tag{6.7}$$

$$f_{^1O_2,ATZ} = \frac{k_{^1O_2,ATZ}\int[^1O_2]dt}{k_{O_3,ATZ}\int[O_3]\,dt + k_{O_2^{\cdot-},ATZ}\int[O_2^{\cdot-}]dt \;+\; k_{^1O_2,ATZ}\int[^1O_2]dt} \tag{6.8}$$

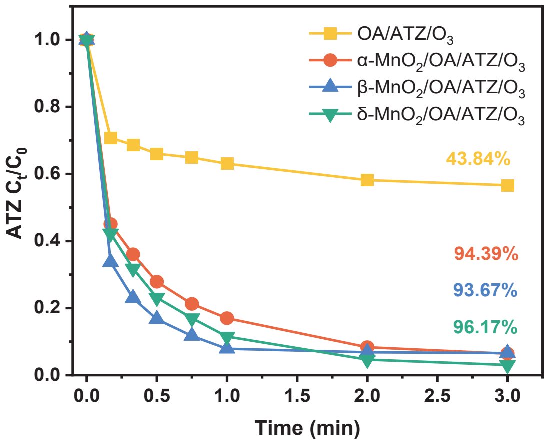

Fig.6.16 The degradation of ATZ in different systems with probe. Experimental conditions: $[ATZ]_0$=5 mg L^{-1}, [Cat]=50 mg L^{-1}, $[OA]_0$=40 mg L^{-1}, $[O_3]_0$=5 mg L^{-1}, [probes]=0.1 mg L^{-1}

Table 6.6 Second-order rate constants for the reaction of test micropollutants with O_3, $^{\bullet}OH$, $O_2^{\bullet-}$, and $^1O_2$.

Compounds	k_{O_3} **(M⁻¹·s⁻¹)**	$k_{^{\cdot}OH}$ **(M⁻¹·s⁻¹)**	$k_{O_2^{\cdot-}}$ **(M⁻¹·s⁻¹)**	$k_{^1O_2}$ **(M⁻¹·s⁻¹)**
TA	0.04	3.3×10^9	1.1×10^4	1.2×10^7
2,4-D	29.1	5.1×10^9	8.3×10^5	No·Reaction
MDE	<1	6×10^9	No·Reaction	1.5×10^8
ATZ	2.3	2.4×10^9	4.1×10^5	$<4\times10^4$

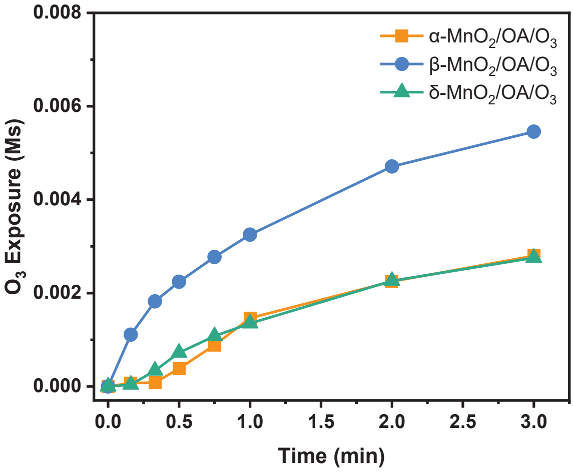

Fig.6.17 The exposures of O_3 during the catalytic ozonation system. Experimental conditions: $[ATZ]_0$=5 mg L^{-1}, [Cat]=50 mg L^{-1}, $[OA]_0$=40 mg L^{-1}, $[O_3]_0$=5 mg L^{-1}, [probes]=0.1 mg L^{-1}

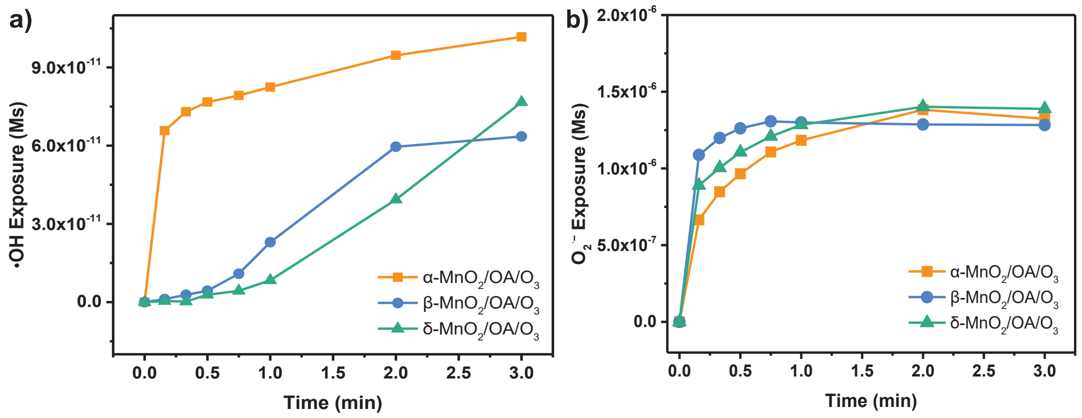

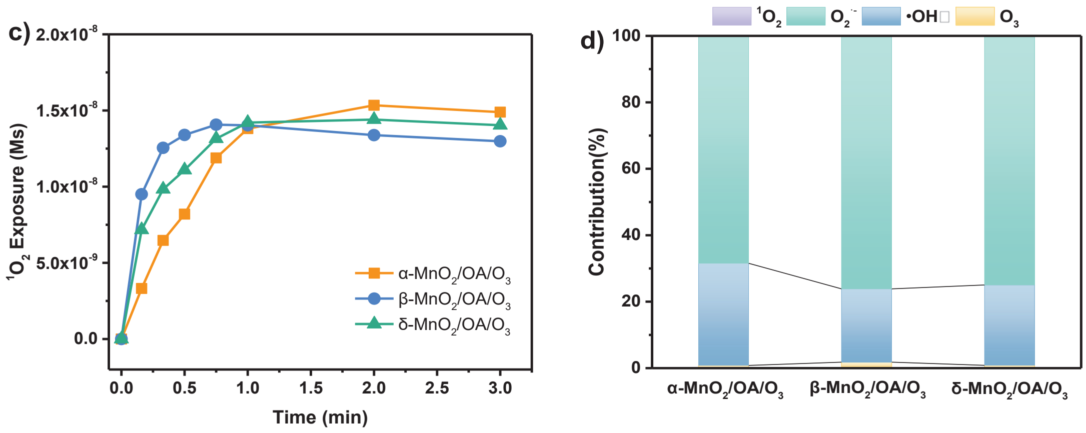

Fig.6.18 The exposures of $^{\bullet}OH$ a), $O_2^{\bullet-}$ b), and $^1O_2$ c), and the contribution rate of ROS and O_3 d) during catalytic ozonation. Experimental conditions: $[ATZ]_0$=5 mg L^{-1}, [Cat]=50 mg L^{-1}, $[OA]_0$=40 mg L^{-1}, $[O_3]_0$=5 mg L^{-1}, [probes]=0.1 mg L^{-1}.

6.3.5 Mechanisms elucidation in various MnO_2-OA/O_3 processes

As shown in FT-IR spectra (Fig.6.10(a)), the peaks of α-MnO_2-OA complex in the range of 1000-1500 cm^{-1} were weaken, indicating the replacement of -OH groups after adding OA into solution. The O_2-TPD spectra (Fig.6.10(b)) of α-MnO_2-OA complex verified the presence of looser O_S on the catalyst surface. Subsequently, an improvement of O_{II}/O_I ratio (0.79) in XPS O 1s spectra of α-MnO_2-OA complex was detected, which further confirmed that the combination of α-MnO_2 and OA was beneficial for the generation of more Vo on the surface of complex. After catalytic ozonation, XPS results of O 1s and Mn 2p (Fig.6.19 and Table 6.8) showed an evident decrease in the ratio of O_{II}/O_I from 0.79 to 0.19, and a subtle decline in that of Mn^{3+}/Mn^{4+} from 1.52 to 1.43, indicating the important role of O_{II} rather than Mn to take effect on catalytic ozonation of ATZ removal [34]. The O_{II} could occupy the Vo and then transformed into ROS, resulting in a consumption of O_{II} and Vo. Above performances and characterization analysis had identified the great role of Vo on catalytic ozonation for ATZ removal. Therefore, a mechanism focusing on the participation and regeneration of Vo was proposed as Eqs.(6.9)-(6.13).

$$[\alpha - MnO_2] + H_2O \rightarrow [\alpha - MnO_2] - OH + H^+ \tag{6.9}$$

$$[\alpha - MnO_2] - OH + OA \rightarrow [\alpha - MnO_2 - OA] - Vo + O_2 + H^+ \tag{6.10}$$

$$[\alpha - MnO_2 - OA] - Vo + O_3 \rightarrow [\alpha - MnO_2 - OA] - O^{2-} + O_2 \tag{6.11}$$

$$[\alpha - MnO_2 - OA] - O^{2-} + O_3 \rightarrow [\alpha - MnO_2 - OA] - O_2^{2-} + O_2 \tag{6.12}$$

$$[\alpha - MnO_2 - OA] - O^{2-}/O_2^{2-} + H_2O \rightarrow [\alpha - MnO_2 - OA] - \dot{O}H + O_2^{\cdot -} + {}^1O_2 \tag{6.13}$$

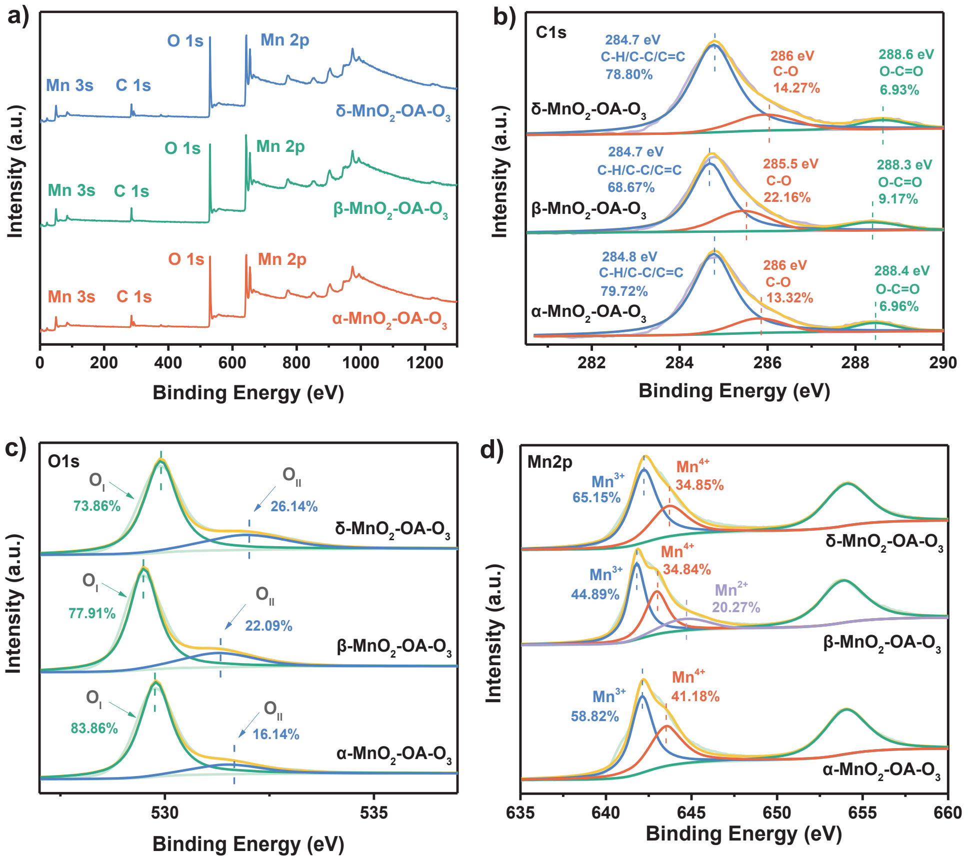

Fig.6.19 XPS spectrum for used α-MnO2-OA, β-MnO2-OA, and δ-MnO2-OA complexes after catalytic ozonation: survey spectra a), C 1s b), O 1s c), and Mn 2p d).

Table 6.7 O 1s spectrum of different catalysts

Catalyst	O1s								
	O_I		O_{II}				O_{III}		O_{II}/O_I
			-OH groups, O_2^{2-}, O^-, O^{2-}						
	Peak (eV)	Area (%)	Peak (eV)	Area (%)	Peak (eV)	Area (%)	Peak (eV)	Area (%)	ratio
α-MnO2-OA-O3	529.7	83.86			531.5	16.14			0.19
β-MnO2-OA-O3	529.5	77.91			531.3	22.09			0.28
δ-MnO2-OA-O3	529.9	73.86			531.8	26.14			0.35

Similarly, the combination of β-MnO_2 and OA occurred through the substitution of -OH groups on the β-MnO_2, as evidenced by the disappearance of 1114 cm^{-1} peak in FT-IR spectra of β-MnO_2-OA complex (Fig.6.10(a)) (Eq (6.14)). However, different from α-MnO_2-OA complex, the O_2-TPD spectra illustrated that β-MnO_2-OA complex had an enhanced O_L mobility. The XPS spectra of β-MnO_2-OA complex (Fig.6.11(d)) revealed a decrease in the proportion of Mn^{4+} and an increase in Mn^{3+} and Mn^{2+}. This indicated a transformation of Mn^{4+} to lower-valence Mn species as the addition of OA, leading to the generation of more V_{Mn} and improved mobility of O_L (Eq (6.15)). As displayed in Table 6.8, the percentage of Mn^{3+} in used β-MnO_2-OA complex declined to 50.51%, and that of Mn^{2+} increased to 20.27%. In β-MnO_2/OA/O_3 process, electrons from the surface of Mn^{2+} or Mn^{3+} would induce O_3 decomposition to ROS which resulted in ATZ degradation, and the oxidation of O_L promoted the reversion of Mn^{3+} to Mn^{2+}. The balance between Mn^{3+}/Mn^{2+} or Mn^{3+}/Mn^{4+} and O_2^-/O^0 was an important factor for the catalytic performance of β-MnO_2-OA complex [35] (Eq (6.16)). Besides, the O 1s peak appeared at 532.4 eV (Fig.6.10(c)) of β-MnO_2-OA complex disappeared in O 1s spectra of used β-MnO_2-OA complex (Fig.6.19(c)). Due to the presence of V_{Mn}, O_3 and H_2O could be adsorbed on the surface of β-MnO_2-OA complex and then participated in the catalytic ozonation reaction (Eq (6.17)). Hence, the catalytic activity could be attributed to the more V_{Mn} and the O_L [36].

$$[\beta - MnO_2] + H_2O \rightarrow [\beta - MnO_2] - OH + H^+ \tag{6.14}$$

$$[\beta - MnO_2] - OH + OA \rightarrow [\beta - MnO_2 - OA - O_L] - V_{Mn} + O_2 + H^+ \tag{6.15}$$

$$[Mn^{4+}/Mn^{3+} - O_L] \overset{e^-}{\rightarrow} [Mn^{3+}/Mn^{2+}] + O_2 \tag{6.16}$$

$$[\beta - MnO_2 - OA - O_L] - V_{Mn} + O_3 + H_2O \rightarrow ROS \tag{6.17}$$

According to the characterization analysis of α-MnO_2, β-MnO_2, and δ-MnO_2 catalysts, δ-MnO_2 contained the highest activity of mobile oxygen and the largest amount of Vo, which could improve O_3 adsorption and decomposition to generate more ROS, thus facilitating the degradation of ATZ (60.73%) (Eq (6.18)). As OA (10 mg L^{-1}) was introduced to the solution, the formed δ-MnO_2-OA complex promoted catalytic ozonation performance achieving 69.87% of ATZ removal. The O_2-TPD spectra (Fig.6.10(b)) revealed the transition from active Os to active O_L on the catalyst surface after δ-MnO_2 complexation with OA. Meanwhile, the FT-IR and the XPS analysis confirmed the presence of H_2O and -OH groups on the surface of δ-MnO_2-OA complex. The results indicated that the abundant Vo of δ-MnO_2 facilitates the adsorption of OA on the catalyst surface, accompanied by the migration of O_L to form complex. In an aqueous environment, H_2O coordinated with Lewis active sites on δ-MnO_2-OA complex surface, leading to the formation of surface -OH [37] (Eq (6.19)). As shown in Table 6.7, after catalytic ozonation, the O_{II}/O_I ratio of used δ-MnO_2-OA complex increased from 0.28 (Table 6.5) to 0.35. This is attributed to the surface -OH acting as active sites, reacting with O_3 to generate more surface oxygen species, which further reacted with ATZ (Eqs.(6.20)-(6.23)). Consequently, more surface Mn^{4+} formed on the catalyst surface converting to Mn^{3+} in order to maintain the electrostatic balance of the δ-MnO_2-OA complex in the reaction between O_3 and ATZ species [18]. That could explain why the Mn^{3+}/Mn^{4+} ratio of used δ-MnO_2-OA complex increased after catalytic ozonation (from 1.60 to 1.87) (Table 6.8). Therefore, it could be concluded that the surface -OH of δ-MnO_2-OA complex played a significant role in δ-MnO_2/OA/O_3 process for ATZ degradation.

$$[\delta - MnO_2 - O^{2-}] \rightarrow [\delta - MnO_2] - V_o + O_2 \tag{6.18}$$

$$[\delta - MnO_2] - V_o + OA + H_2O \rightarrow [\delta - MnO_2 - OA] - OH + H^+ \tag{6.19}$$

$$\begin{aligned}&[\delta - MnO_2 - OA] - OH + O_3 \\ &\qquad \rightarrow [\delta - MnO_2 - OA] - HO_2^- + O_2 + active\ oxygen\ species\end{aligned} \tag{6.20}$$

$$[\delta - MnO_2 - OA] - HO_2^- + O_3 \rightarrow [\delta - MnO_2 - OA] - O_3^{\cdot-} + HO_2^{\cdot} \tag{6.21}$$

$$HO_2^{\cdot} \rightarrow O_2^{\cdot-} + H^+ \tag{6.22}$$

$$\begin{aligned}&[\delta - MnO_2 - OA] - O_3^{\cdot-} + H^+ \rightarrow [\delta - MnO_2 - OA] - HO_3^{\cdot} \\ &\qquad \rightarrow [\delta - MnO_2 - OA] - {}^{\cdot}OH + O_2\end{aligned} \tag{6.23}$$

Table 6.8 Mn 2p spectrum of different catalysts.

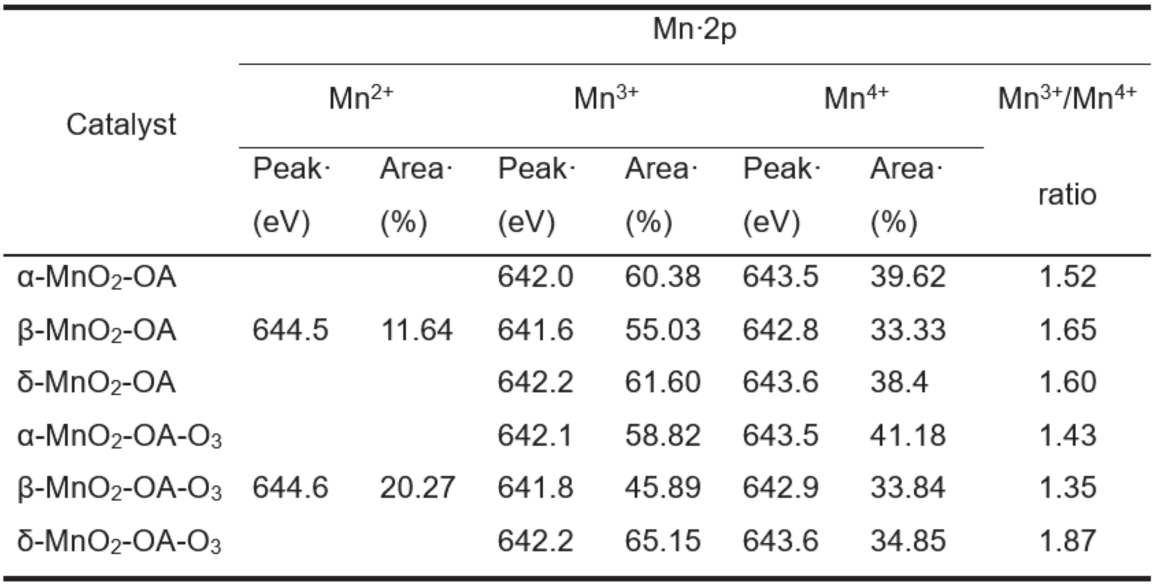

Catalyst	Mn·2p						
	Mn^{2+}		Mn^{3+}		Mn^{4+}		Mn^{3+}/Mn^{4+}
	Peak· (eV)	Area· (%)	Peak· (eV)	Area· (%)	Peak· (eV)	Area· (%)	ratio
α-MnO_2-OA			642.0	60.38	643.5	39.62	1.52
β-MnO_2-OA	644.5	11.64	641.6	55.03	642.8	33.33	1.65
δ-MnO_2-OA			642.2	61.60	643.6	38.4	1.60
α-MnO_2-OA-O_3			642.1	58.82	643.5	41.18	1.43
β-MnO_2-OA-O_3	644.6	20.27	641.8	45.89	642.9	33.84	1.35
δ-MnO_2-OA-O_3			642.2	65.15	643.6	34.85	1.87

Based on aforementioned analysis, in the MnO_2-OA complexes mediated catalytic ozonation system, the different crystal phase of MnO_2 did not affect on the formation of MnO_2-OA complexes, which depended on the existence of Mn^{3+}. However, due to the variations in the structural properties of various MnO_2crystals, the reactive sites of formed complexes in catalytic ozonation were different. Nevertheless, this ultimately promoted the decomposition of O_3 to generate ROS, primarily $O_2^{\bullet-}$, with $^{\bullet}OH$ playing a secondary role, thereby enhancing the elimination rate of pollutants.

6.4 Conclusion

In the catalytic ozonation process, compared to α-MnO_2 and β-MnO_2, δ-MnO_2 demonstrated the highest activity with 60.73% degradation of ATZ. This was attributed to the presence of $^{\bullet}OH_L$, $O_2^{\bullet-}$, and $^1O_2$ in the system. However, the addition of OA (10 mg L^{-1}) to the solution could promote the formation of α-MnO_2-OA, β-MnO_2-OA, and δ-MnO_2-OA complexes, which significantly enhanced ATZ degradation, achieving degradation rates of 78.61%, 84.47%, and 69.87% within 3 min, respectively. Furthermore, increasing the molar ratio of the catalyst to OA was found to significantly enhance the catalytic ozonation efficiency of the complex. Additionally, acidic conditions were shown to facilitate the formation of the complexes.

PP experiments suggested that the formation of MnO_2-OA complexes depends on the presence of Mn^{3+} in the systems. Scavengers and probe tests revealed that $O_2^{\bullet-}$

had a significant impact on the degradation of ATZ, with $^{\bullet}OH$ contributing secondarily. Characterization analysis further elucidated the catalytic mechanisms of the three systems. In α-MnO_2/OA/O_3 process, more oxygen vacancies (Vo) on the surface of complex facilitated the absorption of O_3 and pollutants for further reaction. For β-MnO_2-OA complex, more V_{Mn} and enhanced O_L mobility were key factors contributing to the ROS production in catalytic ozonation. As for δ-MnO_2/OA/O_3 system, the main active sites would be surface -OHs.

CHAPTER 7

General conclusions and recommendations

7.1 General conclusions

In this thesis, three different types of MnO_2 material were synthesized through a modified hydrothermal-calcination method and used in heterogeneous catalytic ozonation system towards contaminant elimination. The effects of the presence of acids, operation parameters, and the selection of experimental mode were investigated. Hence, several conclusions from this study were compiled and discussed in this section.

Referring to Effect of complexation between manganese dioxides and organic acids on enhancing catalytic ozonation efficiency

- Compared to the catalytic ozonation activities of α-MnO_2, β-MnO_2, and δ-MnO_2 synthesized by hydrothermal method alone, three catalysts obtained through a modified hydrothermal-calcination method would improve the degradation of OA (20 mg L^{-1}), which were 98.73%, 99.58%, and 39.82%, respectively.
- The adding sequence of the catalyst and O_3 stock solution would significantly influence the catalytic ozonation efficiency. When adding catalysts into the reaction first, the α-MnO_2/OA/O_3 β-MnO_2/OA/O_3, and δ-MnO_2/OA/O_3 system could achieve the enhanced co-degradation of ATZ and OA.
- The successful co-degradation of pollutant and OA might due to the presence of MnO_2-OA complexes, amongst, β-MnO_2 exhibited the highest catalytic ozonation activity with 76.6% of ATZ and 67.1% of OA removal.
- Considering whether this process is effective for other organic acids or selective to special molecule structures, other acids like formic acid (FA), acetic acid (AA), citric acid (CA), and pyruvic acid (PA) were used in place of OA to conduct the experiment. The results suggested that the presence of PA might also promote catalytic ozonation efficiency through forming complex with MnO_2.

Referring to Insights into the role of β-MnO_2 and oxalic acid complex expediting ozonation: Structural properties and mechanism

- A β-MnO_2-oxalic acid (β-MnO_2-OA) complex, obtained by employing β-MnO_2 fabricated through the hydrothermal-calcination method, could expedite ozonation.
- The simultaneous 90.4% of pCBA degradation and 65.2% of OA removal could be achieved in 10 mins with the incorporation of 50 mg L^{-1} of β-MnO_2, 10 mg L^{-1} of OA and just 2 mg L^{-1} of O_3.
- The *k* value of β-MnO_2/OA/O_3 was 1.541 min^{-1}, which was 4 times that of O_3 alone (0.364 min^{-1}) in the degradation process of pCBA.
- The β-MnO_2-OA complex in β-MnO_2/OA/O_3 process was conducive to the co-degradation of pollutants in HCO process, the degradation efficiencies of ACMP, IBU, and ATZ were improved by 27.96%, 54.18%, and 39.77%, respectively, compared with the single ozonation.
- Systematic characterization techniques (XPS, H_2-TPR, and *etc.*) confirmed the enhanced electron transfer ability and redox property of β-MnO_2-OA complex. More oxygen vacancies and reactive oxygen species (ROS) were generated through facilitating oxygen species migration.
- Sodium pyrophosphate tests demonstrated that Mn^{3+} was mainly responsible for the formation of β-MnO_2-OA complex.
- Scavenger experiments identified surface-$^{\cdot}OH$ and liquid-$^{\cdot}OH$ as major reactive radicals for pCBA degradation, while other ROS were the radicals involved in OA removal.

Referring to −Muti-MnO_2-oxalic acid complexes mediated catalytic ozonation: Phase effects, ROS contribution and Mechanisms

- Compared to O_3 alone, α-MnO_2 and β-MnO_2 showed no significant enhancement in ATZ removal, while δ-MnO_2 exhibited the highest activity with 60.73% of ATZ degradation.

- The addition of OA (10 mg L^{-1}) improved ATZ removal across all α-MnO_2/OA/O_3, β-MnO_2/OA/O_3, and δ-MnO_2/OA/O_3 systems. The newly-formed MnO_2-OA complexes significantly enhanced ATZ degradation, achieving degradation rates of 78.61%, 84.47%, and 69.87% within 3 min, respectively.
- Increasing the molar ratio of the catalyst to OA could significantly enhance the catalytic ozonation activity of the complex. At catalyst-to-OA molar ratio of 1:0.8, the ATZ degradation reached 95.09%, 93.43%, and 96.71% in α-MnO_2/OA/O_3, β-MnO_2/OA/O_3, and δ-MnO_2/OA/O_3 systems, respectively.
- The crystal phase of MnO_2 would not influence the formation of MnO_2-OA complexes. The PP experiments verified that the formation of MnO_2-OA complexes relied on the presence of Mn^{3+} in the system. In addition, acidic conditions would facilitate the complexes generation.
- Probe experiments suggested that in the MnO_2-OA complexes mediated catalytic ozonation system, the $O_2^{\bullet-}$ played a major role in ATZ removal, followed by $^{\bullet}OH$, while O_3 and $^1O_2$ had a lesser effect.
- In terms of α-MnO_2-OA complex, more oxygen vacancy generated on the surface adsorbing O_3 and pollutants for further reaction.
- For β-MnO_2-OA complex, more manganese vacancy and enhanced O_L mobility were key factors contributing to ROS production.
- As for δ-MnO_2-OA complex, the surface -OH groups as main active site reacted with O_3 to generate more ROS thus improving ATZ degradation.

7.2 Future recommendations

Regarding the investigation of interface reaction mechanisms between MnO_2 complexes and O_3:

- This thesis has confirmed the enhanced catalytic ozonation activity of MnO_2-OA complexes for pollutants removal. However, the active sites on the complex surface that react with ozone need to be further determined, such as the activation energy of ozone adsorption by different chemical bonds. In addition, the influence of different crystal facets on the formation of the complex also needs to be further discussed.

- Considering whether this process (MnO_2/acid/O_3) is effective for other organic acids or selective to special molecule structures, the influence of formic acid, acetic acid, citric acid, and pyruvic acid has been initially explored in the chapter 4. The results showed that different acids have different effects on improving the catalytic ozonation efficiency. However, the reaction mechanisms of different acids need further discussion and comparison.

Regarding the application of real water environment:

- Nowadays, experiments and the exploration of reaction mechanisms are primary conducted in pure water and under laboratory conditions. However, for practical application of materials, more tests need to be evaluated at pilot-scale, large-scale, and field applications to address the engineering complexities. The efficiency in real water bodies, the potential effects of variable environmental factors, and the parameters of treatment facilities need to be also considered. In addition, the challenges for the practical application of HCO system include its high operating costs and the cyclic regeneration of catalyst, requiring a balance between costs and efficacy. Therefore, techno-economic assessments for scale-up and operation costs are suggested for future studies.
- Research on MnO_2/MnO_2-based catalysts for contaminants removal in water treatment remains largely confined to observing experimental phenomena and results, with studies on catalysts recyclability typically limited to 3~5 cycles. To enable large-scale applications in the future, the thermodynamic and structural stability of MnO_2/MnO_2-based catalysts for tackling complex environmental contamination should be improved. For long-term sustainability, maintaining ROS activity during catalytic cycles, explaining the intricate reaction mechanisms, and elucidating intermediate pathways warrant further investigations. Exploring the recovery and regeneration of MnO_2/MnO_2-based catalysts could pave the way

towards low-carbon, eco-friendly, and sustainable environmental engineering applications. Moreover, the eco-toxicity analysis of applying MnO_2/MnO_2-based catalyst induced AOPs in water environments is also limited. The ecological toxicity resulting from the long-term exposure of catalysts and the formation of degradation intermediates should be investigated to avoid the increase of ecological risks after pollutant removal.

CHAPTER 8

Publications

8.1 Publications involving the thesis

- **Paper 1** Progress in MnO_2/MnO_2-Based Materials Catalytic Ozonation Process for Water and Wastewater Treatment (**Under review**)

- **Paper 2** Effect of complexation between manganese dioxides and organic acids on enhancing catalytic ozonation efficiency (**Under preparation**)

- **Paper 3** Insights into the role of β-MnO_2 and oxalic acid complex expediting ozonation: Structural properties and mechanism (**Published**) https://doi.org/10.1016/j.seppur.2024.126904

Separation and Purification Technology 341 (2024) 126904

Contents lists available at ScienceDirect

Separation and Purification Technology

journal homepage: www.elsevier.com/locate/seppur

Insights into the role of β-MnO_2 and oxalic acid complex expediting ozonation: Structural properties and mechanism

Jing Liu[a], Xiangjuan Yuan[b,*], Carmen Sans[a,*]

[a] Department of Chemical Engineering and Analytical Chemistry, Faculty of Chemistry, Universitat de Barcelona, C/Martí i Franquès 1, 08028 Barcelona, Spain
[b] School of Environmental Engineering, Wuhan Textile University, Wuhan 430073, China

- **Paper 4** Muti-MnO_2-oxalic acid complexes mediated catalytic ozonation: Phase effects, ROS contribution and Mechanisms (**Under review**)

8.2 Other publication involving the cooperation

- **Paper 1** Constructing boron and oxygen dual coordination in g-C_3N_4 for robust catalytic ozonation and iopamidol degradation (**Published**) https://doi.org/10.1016/j.seppur.2024.130676

Separation and Purification Technology 359 (2025) 130676

Contents lists available at ScienceDirect

Separation and Purification Technology

journal homepage: www.elsevier.com/locate/seppur

Constructing boron and oxygen dual coordination in g-C_3N_4 for robust catalytic ozonation and iopamidol degradation

Jing Liu [a,b,c], Huiyu Dong [b,*], Carmen Sans [c], Xiangjuan Yuan [a,*]

[a] School of Environmental Engineering, Wuhan Textile University, Wuhan 430073, China
[b] Research Center for Eco-Environmental Sciences, Chinese Academy of Sciences, 18 Shuang-qing Road, Beijing 100085, China
[c] Department of Chemical Engineering and Analytical Chemistry, Faculty of Chemistry, Universitat de Barcelona, C/Martí i Franquès 1, 08028 Barcelona, Spain

- **Paper 2** Insights into the photocatalytic ozonation over Ag_2O-ZnO@g-C_3N_4 composite: Cooperative structure, degradation performance, and synergistic mechanisms (**Published**)

  https://doi.org/10.1016/j.jece.2022.107285

Journal of Environmental Chemical Engineering 10 (2022) 107285

Contents lists available at ScienceDirect

Journal of Environmental Chemical Engineering

journal homepage: www.elsevier.com/locate/jece

Insights into the photocatalytic ozonation over Ag_2O-ZnO@g-C_3N_4 composite: Cooperative structure, degradation performance, and synergistic mechanisms

Jing Liu [a,b], Hanlu Shi [a,c], Carmen Sans [b], Lei Sun [a], Xiangjuan Yuan [a,d,*], Fei Pan [a,d], Dongsheng Xia [a,d,*]

[a] School of Environmental Engineering, Wuhan Textile University, Wuhan 430073, China
[b] Department of Chemical Engineering and Analytical Chemistry, Faculty of Chemistry, Universitat de Barcelona, C/Martí i Franquès 1, 08028 Barcelona, Spain
[c] Huaneng Nanjing Jinling Power Generation Co. Ltd, Nanjing 210046, China
[d] Engineering Research Center for Clean Production of Textile Dyeing and Printing, Ministry of Education, Wuhan 430073, China

8.3 Contribution in congresses

- Jing Liu *XIV congreso Español de Tratamiento de Aguas*. Sevilla, 1-3 de Juny 2022 (**Poster** Insights into the photocatalytic ozonation over Ag_2O-ZnO@g-C_3N_4 composite: cooperative structure, degradation performance, and synergistic mechanisms)
- Jing Liu *IOA congference & Exhibition*, Toulouse, France, 28-30 November,2022 (**Poster** Insights into the catalytic ozonation over

manganese oxide composite: Cooperative structure, degradation performance, and synergistic mechanisms)

- Jing Liu *CIPOA - VI Iberoamerican Conference on Advanced Oxidation Technologies*, Florianopólis, Brazil, October 7-11, 2024 (**Poster** Unravelling the role of manganese oxides and oxalic acid complex in catalytic ozonation: Structural properties and mechanistic insights)
- Jing Liu *IOA International congference & Exhibition,* Porto, Portugal, 27-29 November,2024 (**Oral** Insights into the role of manganese oxide and oxalic acid complex enhancing ozonation)

CHAPTER 9

References

Chapter 1

[1] L.J. Fu, Q.J. Wang, J.B. Che, Medical Journal of Chinese People's Liberation Army, 2016, 034(003):305-307.

[2] M.Sharma, A. Bains, K. Sridhar, P. Chawla, M. Sharma, Food Chem. Toxicol., 193 (2024) 115038

[3] Q.J. Zheng, T.Z. Tang, J.D. Yang, Journal of Green Science and Technology, 2011(3):101-104.

[4] D. Nguyen, Minh-Ky Nguyen, Quoc-Minh Truong, Van-Anh Thai, Minh-Thuan Pham, S. Woong Chang, D. Duc Nguyen, Sep. Purif. Technol, 361 (2025) 131489.

[5] N. Morin-Crini, E. Lichtfouse, G. Liu, V, Balaram, A.R.L. Ribeiro, Z. Lu, F. Stock, E. Carmona, M.R. Teixeira, L.A. Picos-Corrales, J.C. Moreno-Piraj´an, L. Giraldo, C. Li, A. Pandey, D. Hocquet, G. Torri, G. Crini, 2022. Environ. Chem. Lett. 20 (4), 2311–2338.

[6] J.H. Liang, Y. Fei, Y.H. Yin, Q. Han, Y.Z. Liu, L. Feng, L.Q. Zhang, Environ. Res. 266(2025)120469.

[7] Ajala, O.J., Tijani, J.O., Salau, R.B., Abdulkareem, A.S., Aremu, O.S., Results in Engineering 16, (2022) 100671.

[8] Kumar Mishra, R., Samyukthalakshmi Mentha, S., Misra, Y., Dwivedi, N., 2023, Water-Energy Nexus.

[9] Oscar M. Rodriguez-Narvaez, J. M. Peralta-Hernandez, A. Goonetilleke, E. R. Bandala, Chem. Environ.J. 323 (2017)361-380.

[10] C.Teodosiu, A.F. Gilca, G. Barjoveanu, S. Fiore, J. Cleaner Prod. 197 (2018) 1210-1221.

[11] Rodriguez-Narvaez, O.M., Peralta-Hernandez, J.M., Goonetilleke, A., Bandala, E.R., Chem. Eng. J. 323 (2017), 361e380.

[12] A. Singh, A. Majumder , D. Saidulu, A. Bhattacharya, A. Bhatnagar , A. K. Gupta, J. Environ. Manage. 354 (2024) 120339.

[13] Upadhyay, A., Singh, R., Talwar, P., Verma, N., Ahire, P.D., Khatri, H., Masakapalli, S.K., Pareek, N., Kumar, V., Kovalev, A.A., Zhuravleva, E.A., Litti, Y.V., Vivekanand, V., 2023. J. Environ. Manag. 343 (118219), 118219.

[14] Vu, C.T., Wu, T., 2021. Environ. Sci. J. Integr. Environ. Res.: Water Res. Technol. 7 (6), 1146–1148.

[15] Meng, Y., Li, X., Wang, B., 2022. Water 14 (21), 3413.

[16] Madhu Sharma, Aarti Bains, Kandi Sridhar, Prince Chawla, Minaxi Sharma, Food and Chemical Toxicology 193 (2024) 115038

[17] Peng, H., Wang, R., Mei, L., Zhang, Q., Ying, T., Qian, Z., Farimani, A.B., Voiry, D., Zeng, Z., 2023. Matter 6 (1), 59–96.

[18] Wu, L., Liu, Y., Hu, J., Feng, X., Ma, C., Wen, C., 2021. Chemosphere 284 (131294), 131294.

[19] Cardoso, I.M.F., Cardoso, R.M.F., da Silva, J.C.G.E., 2021. Nanomaterials 11 (8), 2045.

[20] Cardoso, I.M.F., Cardoso, R.M.F., da Silva, J.C.G.E., 2021. Nanomaterials 11 (8), 2045.

[21] Y.Q. Zeng, [D] Guangdong University of Technology.

[22] Duan F, Li Y, Cao H, et al. Chemosphere, 2015, 125:205-211.

[23] Cardoso, I.M.F., Cardoso, R.M.F., da Silva, J.C.G.E., 2021, Nanomaterials 11 (8), 2045.

[24] Wu, L., Liu, Y., Hu, J., Feng, X., Ma, C., Wen, C., 2021. Chemosphere 284 (131294), 131294.

[25] Wu, L., Liu, Y., Hu, J., Feng, X., Ma, C., Wen, C., 2021. Chemosphere 284 (131294), 131294.

[26] Zhu X , Tian J , Liu R , et al. Sep. Purif. Technol, 2011, 81(3):444-450.

[27] H. Pourzamani, Y. Hajizadeh, N. Mengelizadeh, Process. Saf. Environ. Prot. 119 (2018) 271–284.

[28] G. P. Anipsitakis, D. D. Dionysiou and M. A. Gonzalez, Environ. Sci. Technol., 2006, 40, 1000 —1007

[29]S. Xiao, M. Cheng, H. Zhong, Z. Liu, Y. Liu, X. Yang, Q. Liang, Chem. Eng. J., 2020, 384, 123265.

[30] M. Munoz, Z. M. de Pedro, J. A. Casas,J. J. Rodriguez, Appl. Catal., B, 2015,176–177, 249-265.

[31] C.A. Orge, M.F.R. Pereira, J.L. Faria, Appl. Catal. B: Environ. 174-175 (2015) 113-119.

[32] Y. Liu, H.P. He, D.L. Wu, Process in Chemisty, 2016, 28(7): 1112-1120.

[33] Cardoso, I.M.F., Cardoso, R.M.F., da Silva, J.C.G.E., 2021.. Nanomaterials 11 (8), 2045.

[34] Peng, H., Wang, R., Mei, L., Zhang, Q., Ying, T., Qian, Z., Farimani, A.B., Voiry, D., Zeng, Z., 2023.

[35] Xianfeng Huang, You Xu, Chao Shan, Xuchun Li, Weiming Zhang, Bingcai Pan, Chem. Eng. J.299 (2016)23-29

[36] C.H. Wu, C.Y. Kuo, C.L. Chang, J. Hazard. Mater, 154 (2008) 748–755

[37] E. Issaka, J. Nii-Okai AMU-Darko, S. Yakubu, Funmilayo Omotoyosi Fapohunda, Nisar Ali, Muhammad Bilal, Chemosphere 289 (2022)133208

[38] Z. Song, M. Wang, Z. Wang, Y. Wang, R. Li, Y. Zhang, C. Liu, Y. Liu, B. Xu, F. Qi, Environ. Sci. Technol. 53(9) (2019) 5337-5348.

[39] F. Nawaz, H. Cao, Y. Xie, J. Xiao, Y. Chen, Z.A. Ghazi, Chemosphere. 168 (2017) 1457-1466.

[40] Y. Yuan, Z. Qin, Z. Xu, SBA-15 Catal. Lett. 150(2) (2019) 365-374.

[41] S. Dharmarathna, C.K. King'ondu, L. Pahalagedara, C.-H. Kuo, Y. Zhang, S.L. Suib, Applied Catalysis B: Environmental, 147 (2014) 124-131.

[42] J. Cheng, D. Wang, B. Wang, H. Ning, Y. Zhang, Y. Li, J. An, P. Gao, Chemosphere. 253 (2020) 126595.

[43] M. Xu, Y. Zhang, H. Yin, J. Wang, A. Li, P.F.-X. Corvini, Appl. Catal. B Environ. 322 (2023) 122085.

[44] D. Liu, M. Lin, W. Chen, J. Wang, X. Guo, X. Li, L. Li, Chemosphere, 292 (2022) 133544.

[45] Y. Guo, Y. Zhang, G. Yu, Y. Wang, Appl. Catal. B: Environ. 280 (2021) 119418.

[46] Y. Guo, J. Long, J. Huang, G. Yu, Y. Wang, Water Res 215 (2022) 118275.

[47] F. Li, H. Yin, T. Zhu, W. Zhuang, Eco. Environ. Health. 3(1) (2024) 89-106..

[48] S S.M. Webb, Am. Mineral. 90(8-9) (2005) 1342-1357.

[49] F. Nawaz, H. Cao, Y. Xie, J. Xiao, Y. Chen, Z.A. Ghazi, Chemosphere. 168 (2017) 1457-1466.

[50] Y. Dong, K. Li, P. Jiang, G. Wang, H. Miao, J. Zhang, C. Zhang, RSC Adv. 4(74) (2014) 39167.

[51] I.J. De la Cruz, J.L. Rodríguez S, I. Fuentes, H. Tiznado, J.L. Vazquez-Arce, I. Romero-Ibarra, J.I. Guzmán C, H.M. Gutiérrez, J. Environ. Chem. Eng. 11(5) (2023) 110753

[52] L. Wu, Z. Wang, J. Liu, C. Liu, X. Li, Y. Zhang, W. Wang, J. Ma, Z. Sun, Appl. Catal. B: Environ. 343 (2024) 123526.

[53] P. Li, S. Zhan, L. Yao, Y. Xiong, S. Tian, J. Hazard. Mater. 437 (2022) 129235.

[54] Y.Z. Song, M.S. Li, W.H. Song, Russ. J. Phys. Chem. A. 97(13) (2023) 3161-3167.

[55] S. Juyal, A. Mishra, F.S. Gill, V. Agarwal, P. Juneja, B. Prasad, S. Chandra, A. Parveen, Electrochim. Acta. 475 (2024) 143544.

[56] Y. Dong, H. Yang, K. He, S. Song, A. Zhang, Appl. Catal. B: Environ. 85(3-4) (2009) 155-161.

[57] Y. Guo, S. Zhu, B. Wang, J. Huang, S. Deng, G. Yu, Y. Wang, J. Hazard. Mater. 380 (2019) 120888.

[58] R. Verma, K.R.B. Singh, R. Verma, R.P. Singh, J. Singh, New J. Chem. 48(2) (2024) 554-568.

[59] Y. Tang, D. Li, P. Hollings, X. Sun, Y. Liang, R. Wang, J. Peng, Y. Fu, P. Wang, Mar. Geol. 473 (2024) 107309.

[60] Y. Li, Y. Wang, Y. Cai, R. Fang, L. Zhang, Desalination. 577 (2024) 117387.

[61] X. Ding, Y. Wen, C. Qing, Y. Wei, P. Wang, J. Liu, Z. Peng, Y. Song, H. Chen, Q. Rong, J. Alloy. Compd. 986 (2024) 174041.

[62] J. Ma, S. Zhang, X. Duan, Y. Wang, D. Wu, J. Pang, X. Wang, S. Wang, Chemosphere. 267 (2021) 129287.

[63] K. Luo, S.-X. Zhao, Y.-F. Wang, S.-J. Zhao, X.-H. Zhang, New J. Chem. 42(9) (2018) 6770-6777.

[64] L. Benhaddad, F. Moulai, N. Djouzi, H. Hama, T. Hadjersi, Russ. J. Gen. Chem. 93(8) (2023) 2135-2151.

[65] X. Chen, J. Chen, Y. Liu, Y. Liu, Y. Gao, S. Fan, X. He, X. Liu, C. Shen, Y. Jiang, L. Li, Y. Qiao, S. Chou, ACS Appl. Mater. Interfaces.15(23) (2023) 28106-28115.

[66] S. Wang, J. Xie, M. Wu, F. Wang, Appl. Surf. Sci. 620 (2023) 156803.

[67] X. Huang, W. Cui, J. Yu, S. Lu, X. Liao, Catal. Lett. 152(5) (2021) 1441-1450.

[66] B. Zhao, R. Ran, X. Wu, D. Weng, Appl. Catal. A: Gen.514 (2016) 24-34.

[67] A.S. Poyraz, W. Song, D. Kriz, C.H. Kuo, M.S. Seraji, S.L. Suib, ACS Appl. Mater. Interfaces. 6(14) (2014) 10986-91.

[68] X. Li, H. Zhang, G. Zhang, T. Zhou, R. Min, Water Sci. Technol. 88(8) (2023) 2174-2188.

[69] R.P. Rao, B. Ramasubramanian, R. Saritha, S. Ramakrishna, Nano Express. 4(4) (2023) 045004.

[70] X. Lai, Y. Cheng, C. Han, G. Luo, Mater. Res. Innov. 23(5) (2018) 305-309.

[71] W. Hong, M. Shao, T. Zhu, H. Wang, Y. Sun, F. Shen, X. Li, Appl. Catal. B: Environ. 274 (2020) 119088.

[72] D. Zhang, D. Li, J. Zhang, T. Sun, J. Electroanal. Chem. 901 (2021) 115764.

[73] L. Li, Q. Yang, D. Wang, Y. Peng, J. Yan, J. Li, J. Crittenden, Chem. Eng. J. 421 (2021) 127828.

[74] Z. Xing, M. Fan, J. Liu, Y. Wang, X. Zhang, R. Li, Y. Wang, C. Fan, Inorg. Chem. Commun.150 (2023) 110396.

[75] S. Lee, G. Nam, J. Sun, J.S. Lee, H.W. Lee, W. Chen, J. Cho, Y. Cui, Angew. Chem. Int. Edit. 55(30) (2016) 8599-604.

[76] B. Hu, X. Shang, P. Nie, B. Zhang, J. Yang, J. Liu, J. Colloid Interface Sci. 612 (2022) 392-400.

[77] Y. Xue, Y. Chen, M.-L. Zhang, Y.-D. Yan, Mater. Lett. 62(23) (2008) 3884-3886.

[78] M. Musil, B. Choi, A. Tsutsumi, J. Electrochem. Soc. (9)163 A2047-A2053.

[79] Y. He, L. Wang, Z. Chen, B. Shen, J. Wei, P. Zeng, X. Wen, Sci. Total. Environ.785 (2021) 147328.

[80] L. Lin, J. Wang, Z. Zhao, J. Zhu, A. Zhamaerding, L. Feng, D. Yang, L. Meng, C. He, W. Wang, Y. Zhang, W. Jin, Chem. Eng. J. 474 (2023) 145600.

[81] X. Tan, Y. Wan, Y. Huang, C. He, Z. Zhang, Z. He, L. Hu, J. Zeng, D. Shu, J Hazard. Mater. 321 (2017) 162-172.

[82] F. Nawaz, Y. Xie, J. Xiao, H. Cao, Z.A. Ghazi, Z. Guo, Y. Chen, Catal. Sci. Technol. 6(21) (2016) 7875-7884.

[83] X. Zhang, X. Zhang, B. Zhou, P. Wang, Y. Wang, F. Meng, C. Wei, X. Huang, G. Wen, Colloid. Surface. A. 667 (2023) 131436.

[84] H. Zhao, Y. Dong, P. Jiang, G. Wang, J. Zhang, K. Li, C. Feng, New J. Chem. 38(4) (2014) 1743-1750.

[85] S. Zarei, N. Fallah, M. Mohseni, J. Water Process Eng. 56 (2023) 104355.

[86] B. Zhou, X. Zhang, P. Wang, X. Zhang, C. Wei, Y. Wang, G. Wen, J. Mol. Liq. 401 (2024) 124644.

[87] H. Li, B. Fu, H. Huang, S. Wu, J. Ge, J. Zhang, F. Li, P. Qu, Environ. Pollut. Bioavail. 34(1) (2022) 395-406.

[88] J. Zhang, B. Dong, Y. Han, X. Zhan, S. Ge, S. He, Environ. Eng. Res. 28(3) (2022) 220156-0.

[89] J. Zhang, Z. Wu, B. Dong, S. Ge, S. He, Water Sci. Technol. 89(3) (2024) 823-837.

[90] H. Zhou, W. Su, Y. Xing, J. Wang, W. Zhang, H. Jia, W. Su, T. Yue, Fuel. 366 (2024) 131305.

[91] K. Bourikas, C. Kordulis, A. Lycourghiotis, Chem. Rev. 114(19) (2014) 9754-823.

[92] C. Valdes, C. Quispe, R.A. Fritz, R. Andler, J. Villasenor, G. Pecchi, E. Avendano, A. Delgadillo, W.N. Setzer, J. Sharifi-Rad, BMC Chem. 18 (2024) 83.

[93] C. Valdes, C. Quispe, R.A. Fritz, R. Andler, J. Villasenor, G. Pecchi, E. Avendano, A. Delgadillo, W.N. Setzer, J. Sharifi-Rad, BMC Chem.18(1) (2024) 83.

[94] Y. Teng, K. Yao, W. Song, Y. Sun, H. Liu, Z. Liu, Y. Xu, Int. J. Environ. Res. Public Health. 16(8) (2019).

[95] Q. Cao, F. Lou, N. Liu, J. Zhang, L. Wu, ACS ES&T Water, 1(8) (2021) 1911-1920.

[96] E. Gao, R. Meng, Q. Jin, S. Yao, Z. Wu, J. Li, E. Du, Chem. Phys. Impact. 6 (2023) 100149.

[97] X. Liu, S. Wang, H. Yang, Z. Liu, Y. Wang, F. Meng, J. Ma, O.S. Izosimova, ozone: Sci. Eng. 43(2) (2020) 173-184.

[98] B. Betancur-Corredor, J. Soltan, G.A. Peñuela, ozone: Sci. Eng. 38(3) (2015) 203-210.

[99] S. Xu, H. Bi, G. Liu, B. Su, Water Environ. Res. 91(7) (2019) 650-660.

[100] D. Yang, F. Meng, Z. Zhang, X. Liu, ACS Omega, 8(24) (2023) 21823-21829.

[101] W. Wang, Y. Liu, M. Tang, Catal. Lett. 154(7) (2024) 3677-3691.

[102] H. Zhang, Y. He, L. Lai, G. Yao, B. Lai, Sep. Purif. Technol. 245 (2020) 116449.

[103] F. Nawaz, Y. Xie, J. Xiao, H. Cao, Y. Li, D. Zhang, RSC Adv. 6(35) (2016) 29674-29684.

[104] L. Ke, J. Liu, L. Sun, F. Pan, X. Yuan, D. Xia, J. Water Process Eng. 46 (2022) 102535.

[105] Z. Wang, C. Li, Y. Guo, J. Cheng, Z. Song, D. Sun, F. Qi, A. Ikhlaq, Chem. Eng. J. 455 (2023) 140792.

[106] J. Zhang, Q. Guo, W. Wu, S. Shao, Z. Li, Y. Liu, W. Jiao, Chem. Eng. Sci. 255 (2022) 117667.

[107] C. Gong, X. Lv, S. Liu, X. Chen, R. Weerasooriya, Z. Ding, J. Ind. Eng. Chem. (2024).

[108] Y. Wang, Y. Xie, H. Sun, J. Xiao, H. Cao, S. Wang, J. Hazard. Mater. 301 (2016) 56-64.

[109] Y. Wang, Y. Xie, H. Sun, J. Xiao, H. Cao, S. Wang, J Hazard Mater, 301 (2016) 56-64.

[110] T. Ding, W. Zhao, Y. Sun, S. Li, T. Yu, W. Jing, Appl. Surf. Sci. 609 (2023) 155293.

[111] X. Cheng, H. Liang, F. Qu, A. Ding, H. Chang, B. Liu, X. Tang, D. Wu, G. Li, Chem. Eng. J. 308 (2017) 1010-1020.

[112] Y. Guo, B. Xu, F. Qi, Chem. Eng. J. 287 (2016) 381-389.

[113] X. Li, W. Chen, D. Liu, G. Liao, J. Wang, Y. Tang, L. Li, J. Hazard. Mater. 460 (2023) 132357.

[114] Z. Pan, J. Zeng, B. Lan, X. Wang, G. Liao, L. Li, ozone: Sci. Eng. 37(6) (2015) 527-537.

[115] M. Sui, J. Liu, L. Sheng, Appl. Catal. B: Environ. (2011).

[116] Q. Sun, L. Li, H. Yan, X. Hong, K.S. Hui, Z. Pan, Chem. Eng. J. 242 (2014) 348-356.

[117] C. He, Y. Wang, Z. Li, Y. Huang, Y. Liao, D. Xia, S. Lee, Environ. Sci. Technol. 54(19) (2020) 12771-12783.

[118] T. Tian, P. Zhu, C. He, Y. Xiong, J. Fang, S. Tian, Appl. Catal. B Environ. 359 (2024) 124463.

[119] H. Zhang, S. Song, Q. Xie, Y. Du, Y. Huang, K. Hu, C. Wu, Q. Wu, H. Wang, J. Water Process Eng. 53 (2023) 103819.

[120] J. Zhang, B. Dong, D. Ding, S. He, S. Ge, Environ. Eng. Res. 26(5) (2020) 200394-0.

[121] F. Nawaz, Y. Xie, H. Cao, J. Xiao, YueqiuWang, X. Zhang, M. Li, F. Duan, Catal. Today. 258 (2015) 595-601.

[122] J. Villasenor, P. Reyes, G. Pecchi, Catal. Today. 76 (2022) 121-131.

[123] J. Bing, Y. Xu, C. Wu, X. Lv, X. Xiao, L. Chen, Environ. Sci. Nano. 10(9) (2023) 2312-2323.

Chapter 4

[1] F. Nawaz, H. Cao, Y. Xie, J. Xiao, Y. Chen, Z.A. Ghazi, Chemosphere 168 (2017) 1457-1466.

[2] Y. Dong, K. Li, P. Jiang, G. Wang, H. Miao, J. Zhang, C. Zhang, RSC Adv. 4(74) (2014) 39167.

[3] I.J. De la Cruz, J.L. Rodríguez S, I. Fuentes, H. Tiznado, J.L. Vazquez-Arce, I. Romero-Ibarra, J.I. Guzmán C, H.M. Gutiérrez, Journal of Environmental Chemical Engineering 11(5) (2023) 110753.

[4] S. Juyal, A. Mishra, F.S. Gill, V. Agarwal, P. Juneja, B. Prasad, S. Chandra, A. Parveen, Electrochimica Acta 475 (2024) 143544.

[5] Y. Tang, D. Li, P. Hollings, X. Sun, Y. Liang, R. Wang, J. Peng, Y. Fu, P. Wang, Marine Geology 473 (2024) 107309.

[6] J. Ma, S. Zhang, X. Duan, Y. Wang, D. Wu, J. Pang, X. Wang, S. Wang, Chemosphere 267 (2021) 129287.

[7] J. Zhang, B. Dong, D. Ding, S. He, S. Ge, Environ. Eng. Res. 26(5) (2020) 200394-0.

[8] F. Nawaz, Y. Xie, H. Cao, J. Xiao, YueqiuWang, X. Zhang, M. Li, F. Duan, Catal. Today. 258 (2015) 595-601.

[9] J. Liu, H. Shi, C. Sans, L. Sun, X. Yuan, F. Pan, D. Xia, Journal of Environmental Chemical Engineering 10(2) (2022) 107285.

[10] Z.M. Liu, W.B. Qin, S.T. Li, Q.X. Li, Z.Y. Wang, Proc.SPIE, (2022) 12501.

[11] J.W. Wang, W.F. Yue, Y.G. Teng, Y.Z. Zhai, H.H. Zhu, Chemosphere, 320 (2023) 138054.

[12] S.Y. Sun, Y.H. Wang, L. Zhou, X.Y. Wang, C.L. Kang, Chemosphere, 286 (2022) 131606.

[13] J. Wang, W. Yue, Y. Teng, Y. Zhai, H. Zhu, Chemosphere 320 (2023) 138054.

[14] W.R. Chen, C. Liu, S.A. Boyd, B.J. Teppen, H. Li, Environ Sci Technol 47(3) (2013) 1357-64.

[15] T. Zhang, J.-P. Croué, Applied Catalysis B: Environmental 144 (2014) 831-839.

Chapter 5

[1] R. Andreozzi, A. Insola, V. Caprio, and M.G. D’Amore, Water Res., 26 (1992) 917-921.

[2] J.S. Park, H. Choi, J. Cho, Water Res, 38 (2004) 2284-2291.

[3] M.A. Jiménez-López, A. Rey, F.J. Rivas, F.J. Beltrán, Catal. Today, 430 (2024) 114541.

[4] Z.L. Song, M.X. Wang, Z. Wang, Y.F. Wang, R.Y. Li, Y.T. Zhang, C. Liu, Y. Liu, B.B. Xu, F. Qi, Environ Sci Technol, 53 (2019) 5337-5348.

[5] Y.X. Wang, H.B. Cao, L.L. Chen, C.M. Chen, X.G. Duan, Y.B. Xie, W.Y. Song, H.Q. Sun, S.B. Wang, Appl. Catal. B: Environ., 229 (2018) 71-80.

[6] F. Ji, C.L. Li, L. Deng, Performance of CuO/Oxone system: Chem. Eng. J., 178 (2011) 239-243.

[7] J. Liu, L.J. Ke, L. Sun, F. Pan, X.J. Yuan, D.S. Xia, J. Environ. Chem. Eng., 9 (2021) 106199.

[8] N.P. Chokshi, A. Chauhan, R. Chhayani, S. Sharma, J.P. Ruparelia, Water Sci. Eng., (2023).

[9] M.U. Khalid, M.A. Huwayz, S. Zulfiqar, E.W. Cochran, Z.A. Alrowaili, M.S. Al-Buriahi, M.F. Warsi, M. Shahid, Mater. Sci. Eng. B, 295 (2023) 116580.

[10] M. Ashokkumar, S. Muthukumaran, Physica E: Low-dimensional Systems and Nanostructures, 69 (2015) 354-359.

[11] S. Saini, P. Chand, A. Joshi, Materials Today: Proceedings, 76 (2023) 63-69.

[12] S.R. Le, B.Z.X. Yan, Y.C. Mao, D.Z. Chi, M. Zhu, H.Y. Jia, G.Y. Zhao, X.D. Zhu, N.Q. Zhang, Int. J. Electrochem. Sci., 18 (2023) 1-8.

[13] R.P. Liu, H.J. Liu, Z.M. Qiang, J.H. Qu, G.B. Li, D.S. Wang, J. Colloid Interf. Sci, 331 (2009) 275-280.

[14] Y. Kumar, S. Chopra, A. Gupta, Y. Kumar, S.J. Uke, S.P. Mardikar, Mater. Sci. Energy Technol., 3 (2020) 566-574.

[15] S.M. Wang, K.X. Wang, W.P. Cao, L. Qiao, X. Peng, D. Yu, S.M. Wang, C. Li, C. Wang, Appl. Surf. Sci., 619 (2023) 156667.

[16] E. Hastuti, A. Subhan, P. Amonpattaratkit, M. Zainuri, S. Suasmoro, RSC Adv, 11 (2021) 7808-7823.

[17] D.P. Dubal, W.B. Kim, C.D. Lokhande, J. Phys. Chem. Solids, 73 (2012) 18-24.

[18] Y.H. Wang, Y.L. Sun, M.C. Gao, C.Z. Zhou, Y.J. Xin, G.S. Zhang, P. Xu, D. Ma, J. Clean. Prod., 380 (2022) 134953.

[19] W.W. Jiang, X.J. Xu, Y.X. Liu, L. Tan, F.C. Zhou, Z.W. Xu, R.Z. Hu, J. Alloys Compd., 827 (2020) 154273.

[20] Y. Liu, H. Zhou, R.R. Cao, X.Y. Liu, P.Y. Zhang, J.J. Zhan, L.F. Liu, Appl. Catal. B Environ., 245 (2019) 569-582.

[21] L.J. Liu, B.X. Shen, M. Si, P. Yuan, F.J. Lu, H.P. Gao, Y. Yao, C. Liang, H.J. Xu, RSC Adv, 11 (2021) 18945-18959.

[22] J.S. Cha, Y.M. Kim, I.H. Lee, Y.J. Choi, G.H. Rhee, H. Song, B.H. Jeon, S.S. Lam, M.A. Khan, K.Y. Andrew Lin, W.H. Chen, Y.K. Park, Environ. Pollut., 312 (2022) 119920.

[23] G.J. Fan, Y.C. Guo, S.H. Chai, L. Zhang, J. Guan, G.J. Ma, N. Han, Y.F. Chen, J. Environ. Sci., (2023).

[24] L. Liu, B.D. Wang, X.J. Yao, L. Yang, W.J. Jiang, X. Jiang, Fuel, 283 (2021) 119336.

[25] X. Wang, Y.Y. Zheng, Z. Xu, X.B. Liu, Y.B. Zhang, Catal. Commun., 50 (2014) 34-37.

[26] J.N. Yang, J.J. Zhan, H. Zhou, H.H. Yang, S.Y. Zhang, X.L. Yi, J.J. Shan, Y. Liu, Environ. Res., 217 (2023) 114938.

[27] W. Hong, M.P. Shao, T.L. Zhu, H.N. Wang, Y. Sun, F.X. Shen, X. Li, Appl. Catal. B Environ., 274 (2020) 119088.

[28] T. Putjuso, S. Putjuso, A. Karaphun, S. Nijpanich, N. Chanlek, E. Swatsitang, Appl. Surf. Sci., 618 (2023) 156653.

[29] X.B. Liao, C.L. Pan, Y.S. Pan, C.J. Yin, J. Alloys Compd., 888 (2021) 161619.

[30] J. Huang, M. Han, P. Ji, B. He, X.S. Feng, Y. Han, K.S. Gao, Z.Q. Miao, C.L. Sun, J. Zhi, L. Zhang, P. Chen, Acta, 424 (2022) 140646.

[31] Y. Yan, L. Wang, H.P. Zhang, X.Y. Zhang, Sep. Purif. Technol., 175 (2017) 213-221.

[32] H.W. Li, W.K. Ho, J.J. Cao, D. Park, S.C. Lee, Y. Huang, Environ. Sci. Technol., 53 (2019) 10906-10916.

[33] B. Sun, X.H. Guan, J.Y. Fang, P.G. Tratnyek, Environ. Sci. Technol., 49 (2015) 12414-12421.

[34] S.M. Webb, G.J. Dick, J.R. Bargar, B.M. Tebo, PANS, 102 (2005) 5558-5563.

[35] J. Wang, Y.B. Xie, G.F. Yu, L.C. Yin, J.D. Xiao, Y.X. Wang, W.G. Lv, Z. Sun, J.H. Kim, H. Cao, Environ. Sci. Technol., 56 (2022) 17753-17762.

[36] Y. Yang, J. Huang, S.W. Wang, S.B. Deng, B. Wang, G. Yu, Appl. Catal. B Environ., 142-143 (2013) 568-578.

[37] J. Liu, L. Ke, J. Liu, L. Sun, X.J. Yuan, Y.G. Li, D.S. Xia, J. Hazard. Mater., 371 (2019) 42-52.

[38] E. Gao, R.Y. Meng, Q. Jin, S.L. Yao, Z.L. Wu, J. Li, E. Du, Chem. Phys. Impact, 6 (2023) 100149.

Chapter 6

[1] J. Wang, W. Yue, Y. Teng, Y. Zhai, H. Zhu, Chemosphere, 320 (2023) 138054.

[2] S. Sun, Y. Wang, L. Zhou, X. Wang, C. Kang, Chemosphere, 286 (2022) 131606.

[3] J. Liu, X. Yuan, C. Sans, Sep. Purif. Technol, 341 (2024) 126904.

[4] L. Xia, W. Liang, G. Chen, W. Li, M. Gao, Catalysis Letters, 152 (2021) 1669-1677.

[5] I.J. De la Cruz, J.L. Rodríguez S, I. Fuentes, H. Tiznado, J.L. Vazquez-Arce, I. Romero-Ibarra, J.I. Guzmán C, H.M. Gutiérrez, J. Environ. Chem. Eng, 11 (2023) 110753.

[6] R. Verma, K.R.B. Singh, R. Verma, R.P. Singh, J. Singh, N. J. Chem, 48 (2024) 554-568.

[7] P. Li, S. Zhan, L. Yao, Y. Xiong, S. Tian, J Hazard Mater, 437 (2022) 129235.

[8] J. Ma, S. Zhang, X. Duan, Y. Wang, D. Wu, J. Pang, X. Wang, S. Wang, Chemosphere, 267 (2021) 129287.

[9] E.S. Gad, K. Chaudhary, A.H. Ahmed, S. Rafiq, A.M. Yousif, M. Suleman, Optical Materials, 135 (2023) 113274.

[10] M.U. Khalid, M.A. Huwayz, S. Zulfiqar, E.W. Cochran, Z.A. Alrowaili, M.S. Al-Buriahi, M.F. Warsi, M. Shahid, Mater. Sci. Eng: B, 295 (2023) 116580.

[11] E. Hastuti, A. Subhan, P. Amonpattaratkit, M. Zainuri, S. Suasmoro, RSC Adv, 11 (2021) 7808-7823.

[12] D.P. Dubal, W.B. Kim, C.D. Lokhande, J. Phys. Chem. Solids, 73 (2012) 18-24.

[13] Y. Kumar, S. Chopra, A. Gupta, Y. Kumar, S.J. Uke, S.P. Mardikar, Mater. Sci. Energy Technol, 3 (2020) 566-574.

[14] H. Li, W. Ho, J. Cao, D. Park, S.C. Lee, Y. Huang, Environ. Sci. Technol, 53 (2019) 10906-10916.

[15] W. Hong, M. Shao, T. Zhu, H. Wang, Y. Sun, F. Shen, X. Li, Appl. Catal. B: Environ, 274 (2020) 119088.

[16] G. Fan, Y. Guo, S. Chai, L. Zhang, J. Guan, G. Ma, N. Han, Y. Chen, J. Environ. Sci, (2023).

[17] X. Zhang, B. Zhou, S. Yin, Y. Wang, X. Zhang, Q. Meng, F. Meng, C. Wei, G. Wen, Vacuum, 206 (2022) 111495.

[18] H. Zhao, Y. Dong, P. Jiang, G. Wang, J. Zhang, K. Li, C. Feng, New J. Chem., 38 (2014) 1743-1750.

[19] Y. Yan, L. Wang, H. Zhang, X. Zhang, Sep. Purif. Technol, 175 (2017) 213-221.

[20] J. Huang, M. Han, P. Ji, B. He, X. Feng, Y. Han, K. Gao, Z. Miao, C. Sun, J. Zhi, L. Zhang, P. Chen, Electrochimica Acta, 424 (2022) 140646.

[21] J.N. Yang, J. Zhan, H. Zhou, H.H. Yang, S.Y. Zhang, X. Yi, J. Shan, Y. Liu, Environ Res, 217 (2023) 114938.

[22] Ma J, Graham N J D. Water Res, 2000, 34(15): 3822-3828.

[23] J. Zhao, Z. Zhao, N. Li, J. Nan, R. Yu, J. Du, Chem. Engin. J, 353 (2018) 805-813.

[24] W. Qin, P. Tan, Y. Song, Z. Wang, J. Nie, J. Ma, Sep. Purif. Technol, 261 (2021) 118272.

[25] H. Wang, Z. Lu, D. Qian, Y. Li, W. Zhang, Nanotechnology, 18 (2007) 115616.

[26] S. Wang, K. Wang, W. Cao, L. Qiao, X. Peng, D. Yu, S. Wang, C. Li, C. Wang, Appl. Surf. Sci, 619 (2023) 156667.

[27] R. Liu, H. Liu, Z. Qiang, J. Qu, G. Li, D. Wang, J Colloid Interface Sci, 331 (2009) 275-280.

[28] Y. Wang, J. Dai, M. Wang, F. Qi, X. Jin, L. Zhang, J Colloid Interface Sci, 636 (2023) 577-587.

[29] Y. Liu, H. Zhou, R. Cao, X. Liu, P. Zhang, J. Zhan, L. Liu, Appl. Catal. B: Environ, 245 (2019) 569-582.

[30] Y. Yuan, K. He, B.W. Byles, C. Liu, K. Amine, J. Lu, E. Pomerantseva, R. Shahbazian-Yassar, Chem, 5 (2019) 1793-1805.

[31] E. Gao, R. Meng, Q. Jin, S. Yao, Z. Wu, J. Li, E. Du, Chemical Physics Impact, 6 (2023) 100149.

[32] J. Wang, Y. Xie, G. Yu, L. Yin, J. Xiao, Y. Wang, W. Lv, Z. Sun, J.H. Kim, H. Cao, Environ. Sci. Technol, 56 (2022) 17753-17762.

[33] Y. Guo, Y. Zhang, G. Yu, Y. Wang, Appl. Catal. B: Environ, 280 (2021) 119418.

[34] C. He, Y. Wang, Z. Li, Y. Huang, Y. Liao, D. Xia, S. Lee, Environ. Sci. Technol, 54 (2020) 12771-12783.

[35] X. Tan, Y. Wan, Y. Huang, C. He, Z. Zhang, Z. He, L. Hu, J. Zeng, D. Shu, J. Hazard. Mater, 321 (2017) 162-172.

[36] V.P. Santos, M.F.R. Pereira, J.J.M. Órfão, J.L. Figueiredo, Appl. Catal. B: Environ, 99 (2010) 353-363.

[37] J. Zhang, B. Dong, Y. Han, X. Zhan, S. Ge, S. He, Environ. Eng. Res, 28 (2022) 220156-220150.